**MIDWAVE INFRARED IMAGING FOURIER
TRANSFORM SPECTROMETRY OF
COMBUSTION PLUMES**

DISSERTATION

Kenneth C. Bradley, Captain, USAF

AFIT/DS/ENP/09-S01

**DEPARTMENT OF THE AIR FORCE
AIR UNIVERSITY**

AIR FORCE INSTITUTE OF TECHNOLOGY

Wright-Patterson Air Force Base, Ohio

AFIT/DS/ENP/09-S01

MIDWAVE INFRARED IMAGING FOURIER TRANSFORM SPECTROMETRY

OF COMBUSTION PLUMES

DISSERTATION

Presented to the Faculty

Graduate School of Engineering and Management

Air Force Institute of Technology

Air University

Air Education and Training Command

in Partial Fulfillment of the Requirements for the

Degree of Doctor of Philosophy

Kenneth C. Bradley, B.S.E.E., M.S.E.E.

Captain, USAF

September 2009

AFIT/DS/ENP/09-S01

MIDWAVE INFRARED IMAGING FOURIER TRANSFORM SPECTROMETRY OF COMBUSTION PLUMES

Kenneth C. Bradley, B.S.E.E., M.S.E.E.
Captain, USAF

Approved:

_____   _____
Glen P. Perram, PhD (Chairman)   Date

_____   _____
Guna S. Seetharaman, PhD (Member)   Date

_____   _____
Kevin C. Gross, PhD (Member)   Date

_____   _____
Maj LaVern A. Starman, PhD (Member)   Date

Accepted:

_____   _____
M. U. Thomas   Date
Dean, Graduate School of Engineering and Management

Abstract

A midwave infrared (MWIR) imaging Fourier transform spectrometer (IFTS) was used to successfully capture and analyze hyperspectral imagery of combustion plumes. Jet engine exhaust data from a small turbojet engine burning diesel fuel at a flow rate of 300 $\frac{cm^3}{min}$ was collected at 1 cm^{-1} resolution from a side-plume vantage point on a 200x64 pixel window at a range of 11.2 meters. Spectral features of water, CO, and CO_2 were present, and showed spatial variability within the plume structure. An array of thermocouple probes was positioned within the plume to aid in temperature analysis. A single-temperature plume model was implemented to obtain spatially-varying temperatures and plume concentrations. Model-fitted temperatures of 811 $\pm$ 1.5 K and 543 $\pm$ 1.6 K were obtained from plume regions in close proximity to thermocouple probes measuring temperatures of 719 K and 522 K, respectively. Industrial smokestack plume data from a coal-burning stack collected at 0.25 cm^{-1} resolution at a range of 600 meters featured strong emission from NO, CO, CO_2, SO_2, and HCl in the spectral region 1800-3000 cm^{-1}. A simplified radiative transfer model was employed to derive temperature and concentrations for clustered regions of the 128x64 pixel scene, with corresponding statistical error bounds. The hottest region (closest to stack centerline) was 401 $\pm$ 0.36 K, compared to an in-stack measurement of 406 K, and model-derived concentration values of NO, CO_2, and SO_2 were 140 $\pm$ 1 ppmV, 110,400 $\pm$ 950 ppmV, and 382 $\pm$ 4 ppmV compared to in-stack measurements of 120 ppmV (NO_x), 94,000 ppmV, and 382 ppmV, respectively. In-stack measurements of CO and HCl were not provided by the stack operator, but model-derived values of 19 $\pm$ 0.2 ppmV and 111 $\pm$ 1 ppmV are reported near stack centerline. A deployment to Dugway Proving Grounds, UT to collect hyperspectral imagery of chemical and

biological threat agent simulants resulted in weak spectral signatures from several species. Plume detection of methyl salicilate was achieved from both a stack release and explosive detonation, although spectral identification was not accomplished due to weak signal strength.

Acknowledgements

and I thank them for being there with me.

I would also like to thank Spencer Bowen for the work he did with me for his Master's thesis. He set up a well-organized data collection to look at jet engine exhaust, and built a thermocouple rake to measure in situ plume temperatures. The thermocouple data was very useful in analyzing the jet engine data.

Finally, I would like to thank the PhD '09 Class. I was able to get to know many of you well, and consider you friends. Thanks for making this a good experience. I'm sure we'll cross paths again...

<div align="right">Kenneth C. Bradley</div>

Table of Contents

List of Figures

List of Tables

List of Abbreviations

MIDWAVE INFRARED IMAGING FOURIER TRANSFORM SPECTROMETRY OF COMBUSTION PLUMES

I. Introduction

Analysis of combustion plumes is important for many applications. Jet engine exhaust plumes are analyzed to determine engine performance and to improve upon design. Industrial smokestack plumes are monitored, due to environmental regulations, to ensure pollution output is at acceptable levels. In the post-911 world, an increased emphasis has been placed on plume detection and monitoring for a myriad of applications, including the detection and analysis of improvised explosive devices (IEDs), detection and tracking of chemical and biological threat agents, and monitoring of potential dual-use industrial facilities.

Imaging Fourier Transform Spectrometry has been employed for the study of various plume types, most often in the longwave infrared (LWIR) region of the electromagnetic spectrum, but in recent years, the midwave infrared (MWIR) has demonstrated significant potential for analysis of combustion events, such as explosive detonations, using a single-pixel Fourier Transform Spectrometer (FTS) [26].

To further research in this area, a MWIR Imaging Fourier Transform Spectrometer (IFTS) was developed for the Air Force Institute of Technology (AFIT) by Telops, Inc. to collect hyperspectral imagery of combustion plumes. This one-of-a-kind Field-portable Imaging Radiometric Spectrometer Technology - Midwave Extended (FIRST-MWE) employs an indium antimonide (InSb) focal plane array (FPA) to collect hyperspectral imagery in the 1.5-5.5 μm (1800-6667 cm^{-1}) region.

For this work, the first-ever MWIR IFTS data of jet engine exhaust from the

1

combustion of diesel fuel, industrial smokestack effluents from a coal-burning stack, and chemical agent simulants were collected. Spectral analysis of the jet engine exhaust and industrial smokestack effluent data resulted in the identification of plume constituents, and both data sets were fitted in a least-squares sense to a single-temperature radiative transfer plume model to uncover spatially resolved plume temperatures and column densities of individual plume constituents. Hyperspectral imagery of chemical and biological threat agent simulants were collected at Dugway Proving Grounds, UT, at the invitation of the Joint Project Manager Nuclear Biological Chemical Contamination Avoidance (JPM NBC CA) within the Department of Defense during the Chemical Biological Distributed Early Warning System (CB-DEWS) test in October 2008, but results of this data collection were inconclusive based on a quick-look analysis.

Aside from the unique data sets obtained with the FIRST-MWE, key contributions of this research include a demonstrated method of analyzing turbulent plumes, extraction of temperature and concentrations of plume constituents from spatially-resolved plume spectra, dimensionality reduction of the hyperspectral data by clustering pixels with similar spectral features, and excellent agreement between plume temperature and concentration values obtained by fitting the data to a single-temperature radiative transfer plume model and those obtained via intrusive measurements.

This document is organized to give the reader an understanding of remote sensing of plumes in the MWIR, beginning with this introduction to the research topic. Chapter II details prior work related to this research effort, including imaging spectrometry of several plume-types. Chapter III begins with the basic physical phenomenon of interference, leading to an understanding of the technology associated with IFTS, and an introduction to the Telops FIRST-MWE. Chapter IV details preliminary combustion event data obtained with this one-of-a-kind IFTS, as presented at the 2008

2

International Symposium on Spectral Sensing Research (ISSSR) Conference in Hoboken, NJ and accepted for publication in a special issue of the IEEE Sensors Journal on Enhancement Algorithms, Methodologies & Technology for Spectral Sensing. Chapter V presents IFTS data and analysis of jet engine exhaust plumes to be submitted for publication by AIAA. Chapter VI details the capability of MWIR IFTS to remotely detect and quantify industrial smokestack effluents, as presented at the 2009 Air & Waste Management Association Conference in Detroit, MI and to be submitted for publication in the Environmental Science & Technology Journal. Chapter VII presents analysis of MWIR IFTS and non-imaging FTS data obtained at Dugway Proving Grounds, UT in October 2008. These results were presented at the 2009 SPIE Defense Sensing & Security Conference in Orlando, FL and were published in the conference proceedings. Finally, Chapter VIII contains concluding remarks, and thoughts associated with future work that can follow from this successful research effort.

II. Previous Work

2.1 Remote Spectrometry of Engine Emissions

The exhaust from jet turbine engines contains many chemical species, including carbon dioxide (CO_2), carbon monoxide (CO), nitric oxide (NO), and nitrogen dioxide (NO_2). Additionally, unburnt hydrocarbons (UHCs) are found in the engine exhaust due to the breakdown of heavy molecules in the fuel during combustion [4]. The detection of UHCs from jet engines is needed to certify engine performance and monitor environmental pollutants [4].

Traditionally, in-situ techniques have been employed for UHC detection, as regulated by the International Civil Aviation Organization (ICAO) [70]. Flores-Jardines, *et.al.*[23] highlights the following advantages of non-intrusive optical methods for detection of UHCs:

- lower operational costs

- ease of handling

- online measurements

- data can be re-analyzed without affecting data source (measured spectra)

- extractive sampling of chemicals is not required: avoids possible chemical changes due to probe and extraction system before analysis

- eliminates risk of engine damage during measurement

- measurements can be taken during airport operations

Fourier Transform infrared (FTIR) spectrometry has been used to non-intrusively detect hydrocarbons from gas turbine engine exhaust emissions using both non-imaging [6; 5; 4; 39; 70; 68; 69; 33; 67; 71] and imaging [23; 66] Fourier Transform spectrometers (FTS).

Rusch, *et.al.*[66] and Flores-Jardines, *et.al.*[23] used a Scanning Infrared Gas Imaging System of High Resolution (SIGIS HR) to monitor engine exhaust during airport operations. SIGIS HR consists of an IR camera (JENOPTIK Variocam Head) with a Mercury Cadmium Telluride (MCT) focal plane array (FPA), a scanning mirror, a telescope, two digital signal processor (DSP) systems (FTIR DSP and Video DSP), a Bruker OPAG interferometer, and a personal computer (PC) with monitor [66]. Two stepper motors are used to position the scanning mirror. Mirror control, data acquisition and pre-processing is performed by the FTIR DSP system, and the Video DSP system captures the IR imagery to be processed and displayed on the monitor [66].

Rusch, *et.al.* utilized three different measurement methods for mirror alignment. These are manual mode, scan mode, and track mode. Each method is detailed below. [66]

In manual mode, fast (17 spectra per second), low resolution ($\Delta\sigma = 56$ cm^{-1}) spectra were measured and viewed in real-time. The hot exhaust gases show a CO_2 signature around 2400 cm^{-1} in this low resolution mode. The SIGIS HR system allows the user to simultaneously view the entire IR image from the camera with a square superimposed on the image to show where the mirror is looking. The user can move the square on the screen to the desired location (with respect to the IR image) to capture the hot exhaust gases with the spectrometer. When the CO_2 signature appears in the low resolution spectrum, the mirror is positioned correctly for high

resolution ($\Delta\sigma = 0.2$ cm^{-1}) measurement. [66]

In scan mode, four different algorithms were employed to perform the same objective as manual mode, with little to no user interference after initial setup. The user defines the scan region, and then the mirror is automated. The system records spectra within the scan region, at the same fast, low resolution as defined for the manual mode. The background temperature algorithm integrates the signal over the spectral range from 800 cm^{-1} to 1200 cm^{-1}, giving a background temperature image of the scene. The gas temperature algorithm performs a similar integral over the spectrum within the CO_2 signature range, resulting in a gas temperature image. The intensity difference algorithm calculates the difference between the peak intensity of the CO_2 signature and a baseline over the CO_2 spectral range. The baseline is established with a linear function between two spectral intensities immediately below and above the CO_2 spectral range. Finally, the integrated intensity difference algorithm integrates the difference between the CO_2 peak and the baseline. The intensity difference and integrated intensity difference algorithms were best able to determine the ideal mirror position for high-resolution measurements. [66]

In track mode, the user positions the mirror so that it is aimed at a region close to the engine by selecting it on the screen. A search algorithm is then implemented to find the area with the highest IR-emission near the selected point. The mirror is repositioned to the hot-spot, and the algorithm repeats itself. The hot turbine on the engine is automatically tracked by SIGIS HR during push-back from the gate, at which time the aircraft sits for several minutes. Using the track mode, the ideal mirror position has already been determined, the mirror is in position, and high-resolution measurements can be taken.[66]

Flores-Jardines, *et.al.* used SIGIS HR to measure temperature and gas concentration distributions in hot engine exhaust from a Boeing B737. The scan mode was used

6

for mirror alignment to capture spectra of the exhaust plumes from the engine when the aircraft was on the taxiway and the auxiliary power unit (APU) while parked. With the mirror positioned in the optimum location for each measurement, a high resolution spectrum was recorded at 0.2 cm^{-1}. Synthetic emission spectra at different temperatures and concentrations were calculated and compared to the observed spectra by the least-squares-fitting technique. Molecular parameters were extracted from the *hi*gh-resolution *tran*smission molecular absorption (HITRAN) database, and the Multi-component Air Pollution Software (MAPS) was used to interpret the measured spectrum using a line-by-line calculation of the thermal emission and molecular absorption of the air components. [23]

2.2 Industrial Smokestack Monitoring

Industrial smokestack monitoring in support of the Environmental Protection Agency (EPA) using Fourier Transform spectroscopic techniques was first implemented in the late 1970's and early 1980's [72; 36; 35].

Selby, *et.al.* used a General Dynamics model PFS-201 Fourier spectrometer to measure MWIR exhaust plume spectra from an oil-burning power plant and compared it to calculated spectra using the LOWTRAN 4 Radiance Model. With a 0.5 cm^{-1} spectral resolution over the 1900-2600 cm^{-1} spectral range, signatures of several chemical species were detected, including carbon dioxide (CO_2), sulfur dioxide (SO_2), dinitrous oxide (N_2O), and carbon monoxide (CO). [72]

Herget, *et.al.* used the Remote Optical Sensing of Emissions (ROSE) System to make measurements of various pollutant sources, including a phosphate fertilizer plant gypsum pond, jet engines, oil refineries, coal-burning power plants, and a cement smokestack. ROSE is a non-imaging FTIR system that covers the 700-6000 cm^{-1} spectral region at a resolution of 0.1 cm^{-1}. The wide spectral range is possi-

ble using a MCT detector for the 700-1800 cm^{-1} region and an indium antimonide (InSb) detector for the 1800-6000 cm^{-1} region. Spectral signatures of SO_2, NO, CO_2, and HCl (hydrogen chloride) were detected from the power plant smokestack emissions, and spectral signatures of NH_3 (ammonia), NO, CO_2, CO, SO_2, HCl , H_2CO (formaldehyde), and HF (hydrogen flouride) were detected from the cement plant smokestack emissions. [36; 35]

While a few notable publications related to non-imaging FTIR spectroscopy of smokestack plumes exist [11; 30], the focus of the remainder of this section will be on imaging spectrometers and corresponding chemical detection and identification algorithms. Hyperspectral imaging spectrometers have led to an increased level of research in the area of smokestack monitoring, due in part to the merging research interests of multiple fields. While earlier work was performed almost exclusively by spectroscopists and atmospheric scientists, the invention of the imaging spectrometer and advancements in computational efficiency has led to increased participation by the remote sensing community. Consequently, the literature over the past two decades is replete with articles on both instrumentation [12; 42; 77; 73] and algorithms [63; 54; 60; 45; 55; 31] to aid in the remote smokestack monitoring problem.

2.2.1 Imaging Spectrometers for Industrial Smokestack Monitoring.

Lawrence Livermore National Laboratories developed an imaging Fourier Transform spectrometer (IFTS) to monitor chemical emissions. A chlorodifluoromethane (freon-22) gas plume was imaged with the IFTS in the LWIR region at 4 cm^{-1} spectral resolution. The background during this measurement was the cold night sky, which was imaged prior to the chemical release. Background subtraction was used to measure the freon-22 emission spectra. [12]

Pacific Advanced Technology (PAT) developed a hyperspectral imaging sensor,

known as Image Multi-spectral Sensing (IMSS) for gas plume monitoring. IMSS takes advantage of a diffractive optical element's chromatic abberations for both imaging and dispersion, and is able to detect chemical plumes at a distance of 5 km. Designed to operate in the MWIR, PAT imaged the plume of an oil refinery smokestack at night from a stand-off distance of 1 km, with a spectral bandwidth of 0.01 μm and center wavelength of 4.6 μm. [42]

Northrop Grumman, Inc. built a LWIR hyperspectral imager that consists of a grating spectrometer and MCT FPA. The instrument's instantaneous field of view (IFOV) is 0.9 mrad, which corresponds to a ground sampling distance (GSD) of 1 m at an altitude of 1.1 km. Cross-track coverage at this altitude is 128 m. The instrument measures 256 spectral bands within the LWIR range of 8-12.5 μm. The instrument was used to image a release of hydrofluorocarbon 1,1,1,2-tetrafluoroethane (HFC-134a), and plume concentrations were calculated based on the acquired data using a modified version of Flannigan's Three-Layer Model.[73]

2.2.2 Hyperspectral Algorithms for Industrial Smokestack Monitoring.

Polak, *et.al.* derived a ratioing algorithm for quantitative analysis of a plume using LWIR data. The only data required to compute the special ratio are the plume spectrum, the background spectrum, and spectrum of a high-emissivity plate at ambient temperature. The resulting special ratio can be used to directly calculate the column density of the plume. The key assumptions to use this algorithm are that the plume transmission is approximately one (totally transmitting), or that the plume is at ambient temperature, surrounded by a uniform medium also at ambient temperature. This algorithm automatically removes background and internal instrument signatures. [63]

Mehta, *et.al.* used a Sticklet Transform Method to estimate trace chemicals from industrial plumes from MWIR data. A Sticklet Least Squares (SLS) method was compared to the Classical Least Squares (CLS) method for remote chemical sensing in MWIR. By choosing an appropriate sticklet (combination of lobewidth and lobe separation) for a given target chemical species, SLS was shown to provide accurate chemical concentration estimates for butanol, chloromethane, and isopropanol. [54]

O'Donnell, *et.al.* applied a sub-pixel version of the Invariant Algorithm to generated LWIR hyperspectral plume test imagery to demonstrate the detection and identification of single gases in weak plumes and mixtures of gases in strong plumes. Absorption spectra of target gases are extracted from the PNNL database, and spectral value decomposition (SVD) is implemented to form basis vectors for the modelled data. SVD is also implemented on a section of the scene that contains background pixels, resulting in background basis vectors. A generalized likelihood ratio test (GLRT) is implemented to determine whether a given pixel is more like the target or background, and the pixel is assigned, accordingly. Single gas identification using this method gave promising results, whereas identification of gases within a gas mixture was poor. [60]

Jellison, *et.al.* used a ratio of intensities from two different CO_2 infrared molecular transitions within a gas plume to calculate the plume temperature. The two transition wavelengths best suited for CO_2 temperature measurements are 4.19668 and 14.5023 μm. The root-mean-square (RMS) error between temperature calculated using the intensity ratio method and thermocouple ground truth temperature data is 22 K. Accurate plume temperatures should lead to the ability to use IR intensity data to determine plume gas concentration. [45]

Messinger, *et.al.* used physics-based signatures to detect gases from airborne LWIR hyperspectral imagery. The physics-based signatures take into account atmo-

spheric effects (using MODTRAN data), background spectral characteristics, temperature contrast between plume and background, and plume gas concentration. A GLRT approach based on a matched subspace detector (MSD) is used to distinguish between background and plume pixels. The physics-based signature approach outperformed the clutter-matched filter (CMF) algorithm when applied to data collected by the Airborne Hyperspectral Imager (AHI) looking down at facility propane and methane releases. [55]

Heasler, *et.al.* used a nonlinear Bayesian regression (NLBR) algorithm for gas plume detection and estimation from LWIR hyperspectral data. When compared to the more common matched filter approach for estimation of gas concentrations of ammonia, ethylene, and butyl acetate, the NLBR approach resulted in better estimates. Atmospheric variability was not included in the NLBR algorithm, resulting in less than optimal performance when implemented against real hyperspectral data. However, due to the flexibility of the NLBR approach, modification to include atmospheric variables may be included in the future, and should result in greatly improved performance on real hyperspectral gas plume data. [31]

2.3 Chemical and Biological Agent Detection

Especially in recent years, homeland defense and national security interests have resulted in an increased focus on chemical and biological agent detection and defeat. Standoff chemical detection has been demonstrated using various imaging spectrometers [42; 24; 41; 51; 52; 27; 75] and hyperspectral algorithms [50; 49; 79; 48; 43]. Although the emphasis of research has been in the LWIR for both instrument and algorithm development, the potential for chemical and biological agent detection in the MWIR has been demonstrated without a clear understanding of the phenomenology [41]. The remainder of this section will identify the key players for stand-off detec-

tion of chemical and biological agents by describing the state-of-the-art in imaging spectrometers and hyperspectral algorithms designed for this purpose.

2.3.1 Imaging Spectrometers for Chemical and Biological Agent Detection.

Pacific Advanced Technology (PAT) developed a small, handheld imaging spectrometer based on a patented Image Multi-spectral Sensing (IMSS) technique. IMSS uses diffractive optics in combination with image processing to capture spectral information about the object scene. PAT participated in a series of field trials at Dugway Proving Grounds in 2002 to detect chemical and biological agents. Among their notable achievements during this test was the ability to detect *bacillus globigii* (BG), a simulant of anthrax, from a standoff distance of 3.5 km at night in the MWIR. This result was unexpected, based on spectral absorption characteristics of BG, but a full understanding of this phenomenon may lead to the capability of detecting chemical or biological agents in the MWIR. [41]

The US Army Research Laboratory (ARL) developed a dual-band hyperspectral imager (DBHSI) for chemical and biological agent detection. The DBHSI uses the PAT IMSS lens in conjunction with a DRS Infrared Technologies cooled dual-band MCT FPA. The LWIR image is formed by 1st order diffraction, and the MWIR image is formed by 2nd order diffraction, resulting in simultaneous capture of two hyperspectral image cubes covering the 4-5.2 μm and 8-10.4 μm regions. A biological standoff detection field test at Dugway Proving Grounds, UT in June 2005 demonstrated detection of BG and BA (*bacillus anthracis*) in both MWIR and LWIR, showing that both biological agent simulants have MWIR absorption. [27]

Physical Sciences, Inc. (PSI) developed a Fabry-Perot (FP) imaging spectrometer designed for the LWIR, known as Adaptive InfraRed Imaging Spectoradiometers

12

(AIRIS). AIRIS is able to selectively detect one or two chemical species in plumes consisting of many chemical species, as well as detection of a single chemical species using a limited number of detection bands with low rate of false alarm. PSI used AIRIS to detect plume releases of three potential interferents, Dimethyl Methyl Phosphonate (DMMP), trichloroacetic acid (TCA), and n-butanol, with low false alarm rates. [24]

Further development led to the AIRIS-WAD system, an airborne prototype mounted on a UH-1 helicopter for wide area chemical and biological agent detection. Three technology readiness experiments (TRE) were conducted from the UH-1 platform to demonstrate detection of SF_6 and BG. The test locations were at Dugway Proving Grounds during the 2002 TRE and in urban areas in Oklahoma City for the Joint Urban 2003 tests. Additional ground-based testing was conducted at the Pentagon in Washington, D.C. during the Pentagon Shield test, which was set-up to detect an SF_6 release from a vehicle in the south parking lot at the Pentagon. [51; 52]

Telops, Inc. developed the Field-portable Imaging Radiometric Spectrometer Technology (FIRST), which is an IFTS designed with a 320x256 pixel MCT FPA for chemical detection in the LWIR. The FIRST collects hyperspectral datacubes at user-selectable spectral resolution between 0.25 and 150 cm^{-1}. With an individual pixel field of view (FOV) of 0.35 mrad, the FIRST can view a 5x6 degree scene with high spatial resolution, allowing for simultaneous measurements of background (off-plume) and target (plume) spectra. Using a principle component analysis (PCA) for background suppression and two standard hyperspectral imaging algorithms, spectral matched filter (SMF) and spectral angle mapper (SAM), measured data was compared to high resolution spectra from the Pacific Northwest National Library (PNNL) IR database to detect ten chemical species of interest, including acetic acid, triethylphosphate (TEP), diethyl ethylphosphonate (DEEP), DMMP, and NH_3. [75]

2.3.2 Hyperspectral Algorithms for Chemical and Biological Agent Detection.

Vallieres, *et.al.* developed a fast hyperspectral algorithm for chemical detection from LWIR thermal imagery. The algorithm uses a combination of CMF and SAM, with appropriate thresholding and spatial filtering, to detect and identify chemicals within the FOV. The PNNL IR database is used as a reference library for chemical identification. The entire algorithm can be implemented by the signal processing hardware of the Telops' FIRST system, making it both fast and robust for real-time chemical agent detection. [79]

Manolakis, *et.al.* used a linear model to characterize thin plumes in the LWIR. For plumes with known gas composition, the GLRT approach can be used to derive appropriate detection algorithms. The background can be modelled either with first- and second-order statistics (unstructured background model) or a linear subspace (structured background model). Among the GLRT detectors investigated were the adaptive matched filter (AMF), the adaptive coherence/cosine estimator (ACE), and the optimum matched filter. [50; 49]

Kwan, *et.al.* used spectral unmixing methods to identify and quantify chemical and biological agents from government-furnished LWIR datasets. SAM and SID (spectral information divergence) were the two similarity measures employed to compare the orthogonal subspace projection (OSP) and nonnegatively constrained least squares (NCLS) unmixing, classification, and abundance estimation methods. OSP worked well when the database consisted of only a small number of distinct chemical agents, and performance degraded rapidly for larger datasets or when overlaps existed between similar chemical agents of interest. The NCLS method outperformed OSP, resulting in more accurant abundance fraction estimates. [48]

Hirsch, *et.al.* employed a divisive hierarchical spectral-spatial decomposition al-

gorithm to detect chemical agents without any *a priori* background or plume size and position information. Wavelength-dependent gas transmission is extracted from the LWIR hyperspectral image cube using the special ratio, as in [63]. Prior to implementing the divisive hierarchical spectral-spatial decomposition algorithm, a median filter is applied to each spectral band's 2D image. This removes bad pixels due to noise spikes or nonuniformity by spatially-smoothing the image cube. The algorithm was applied to a LWIR hyperspectral image of simultaneous release of CHF_3 (trifluoromethane) and SF_6, captured by the FIRST system. Both gases were identified from this gas mixture. Over 114 hyperspectral images were recorded with either no plume, a single-chemical plume, or a chemical mixture, with 100% correct identification and no false alarms. [43]

III. Imaging Fourier Transform Spectrometry

In recent years, Imaging Fourier Transform Spectrometry has emerged as a novel technique to measure the hyperspectral signature of objects. Spectrometry is the measurement of an object's spectra (intensity vs wavelength), whereas imaging provides spatial information about the object. The combination of imaging with spectrometry results in a three dimensional hyperspectral datacube.

The spectral dimension of the directly-acquired datacube from an Imaging Fourier Transform Spectrometer (IFTS) is known as an interferogram, resulting from interference between plane waves, and a transformation is required to uncover the spectral content. The two-dimensional spatial information of the object is acquired from the FPA, where individual pixels can be mapped from object to image space, as with a standard camera. A simplified way of visualizing IFTS data, is to consider each pixel as containing the entire spectral content of a point in the object scene in the form of an interferogram, instead of an integrated intensity value. Fourier Transform techniques are used to convert the interferogram into the desired spectra.

This chapter will begin with the basic principles of interference, leading to a discussion of Michelson Interferometers and Imaging Fourier Transform Spectrometers. Finally, a specific IFTS, the Telops, Inc. FIRST, will be described in detail, as this is the instrument that was used for this research.

3.1 Interference

A physical and mathematical basis must be established in order to detail the operating principles of IFTS. Among the most basic physical principles is that of interference. Following the derivation in [32], consider two linearly polarized plane waves:

$$\vec{E}_1(\vec{r}, t) = \vec{E}_{01} \cos(\vec{k}_1 \cdot \vec{r} - \omega t + \epsilon_1) \tag{1}$$

and

$$\vec{E}_2(\vec{r}, t) = \vec{E}_{02} \cos(\vec{k}_2 \cdot \vec{r} - \omega t + \epsilon_2) \tag{2}$$

The superposition of these two waves, gives the resultant wave:

$$\vec{E} = \vec{E}_1 + \vec{E}_2 \tag{3}$$

Intensity, which is proportional to the squared time average of the magnitude of the electric field, can be defined for this resultant wave as:

$$
\begin{aligned}
I &= <\vec{E}^2>_T \\
&= <\vec{E} \cdot \vec{E}>_T \\
&= <(\vec{E}_1 + \vec{E}_2) \cdot (\vec{E}_1 + \vec{E}_2)>_T \\
&= <\vec{E}_1^2 + \vec{E}_2^2 + 2\vec{E}_1 \cdot \vec{E}_2>_T \\
&= I_1 + I_2 + 2 <\vec{E}_1 \cdot \vec{E}_2>_T
\end{aligned}
\tag{4}
$$

where I_1 and I_2 are the intensities of superposed waves, E_1 and E_2, respectively. The remaining term in Equation 4, is known as the interference term, which can be further expanded as follows:

$$
\begin{aligned}
I_{12} &= 2 < \vec{E}_1 \cdot \vec{E}_2 >_T \\
&= 2 < \vec{E}_{01} \cdot \vec{E}_{02} \cos(\vec{k}_1 \cdot \vec{r} - \omega t + \epsilon_1) \cos(\vec{k}_2 \cdot \vec{r} - \omega t + \epsilon_2) >_T \\
&= \vec{E}_{01} \cdot \vec{E}_{02} \cos(\vec{k}_1 \cdot \vec{r} + \epsilon_1 - \vec{k}_2 \cdot \vec{r} - \epsilon_2) \\
&= \vec{E}_{01} \cdot \vec{E}_{02} \cos \delta
\end{aligned}
\tag{5}
$$

where $\delta = \vec{k}_1 \cdot \vec{r} + \epsilon_1 - \vec{k}_2 \cdot \vec{r} - \epsilon_2$ is the phase difference between the two interfering waves. For our purposes, we will assume that $\vec{E}_{01}$ and $\vec{E}_{02}$ are parallel, and that there is no initial phase difference between the two waves. In this monochromatic, fully coherent case, Equation 5, reduces to:

$$
\begin{aligned}
I_{12} &= 2 E_{01} E_{02} \cos \delta' \\
&= 2 \sqrt{I_1 I_2} \cos \delta'
\end{aligned}
\tag{6}
$$

where $\delta' = \vec{k}_1 \cdot \vec{r} - \vec{k}_2 \cdot \vec{r}$ is the phase difference due exclusively to difference in optical path length between the two waves. A further simplification results when $I_1 = I_2 = \frac{I_s}{4}$, which is the case for amplitude splitting interferometers, where I_s is the intensity of light that enters the interferometer. Equation 4 becomes

$$
\begin{aligned}
I &= \frac{I_s}{2} + \frac{I_s}{2} \cos \delta' \\
&= \frac{I_s}{2} [1 + \cos \delta']
\end{aligned}
\tag{7}
$$

3.2 Michelson Interferometer

The physical property of interference has been exploited to make precise optical measurements using relatively inexpensive instruments. One such device is known as an amplitude-splitting interferometer, its most common form being that of a Michelson interferometer. A Michelson interferometer consists of a lens to collimate the light, a beam splitter to divide the incoming beam into two paths, an adjustable moving

mirror, a fixed mirror, a compensator plate, and a detector. The compensator plate is used to ensure that the optical path difference (OPD) between the two beam paths results exclusively from the position of the movable mirror with respect to the beam splitter. Zero path difference (ZPD) occurs when the fixed and movable mirrors are equidistant from the beam splitter, resulting in perfectly constructive interference. Interference fringes, which are a function of wavelength and OPD, will be formed at the detector when the interferometer is not set to ZPD. [32]

From Equation 7, given an incident monochromatic source of wavenumber $\bar{\nu}$ and intensity I_s, the Michelson interferometer output intensity can be calculated as a function of OPD, $\Delta = \frac{\delta'}{2\pi\bar{\nu}}$, as:

$$I(\Delta) \;\; = \;\; \tfrac{I_s}{2}[1 + \cos(2\pi\bar{\nu}\Delta)] \tag{8}$$

Since OPD is related to mirror displacement, x, by $\Delta = 2x$, the maximum intensity of $I(\Delta) = I(2x) = I_s$ occurs for $x = \frac{m}{2\bar{\nu}}$. Intensity minima, $I(x) = 0$, corresponds to mirror displacement of $x = \frac{2m+1}{4\bar{\nu}}$. In both cases, m is any integer value.

If the variable mirror position is moved from ZPD with velocity $V\frac{cm}{s}$, the change in OPD with respect to time $(\frac{\delta\Delta}{\delta t})$ is equal to $2V$. The corresponding frequency of the output intensity as a function of time, $I(t) = \frac{I_s}{2}[1 + \cos(2\pi\bar{\nu}2Vt)]$ is $f = 2\bar{\nu}V$ Hz, where $t = \frac{x}{V}$ sec. The Michelson interferometer operates as a linear frequency transducer, converting a relatively high frequency optical signal into a user-defined electrical frequency, with a proper choice of mirror velocity, V.

For a non-monochromatic source, I_s in the preceding discussion must be replaced with the frequency-dependent intensity, $I_s(\bar{\nu})$ and integrated over all wavenumbers. Equation 8 becomes:

$$
\begin{aligned}
I(\Delta) &= \int_{-\infty}^{\infty} \frac{I_s(\bar{\nu})}{2}[1 + \cos(2\pi\bar{\nu}\Delta)]d\bar{\nu} \\
&= 2\int_0^{\infty} \frac{I_s(\bar{\nu})}{2}[1 + \cos(2\pi\bar{\nu}\Delta)]d\bar{\nu} \\
&= \int_0^{\infty} I_s(\bar{\nu})d\bar{\nu} + \int_0^{\infty} I_s(\bar{\nu})\cos(2\pi\bar{\nu}\Delta)d\bar{\nu}
\end{aligned} \tag{9}
$$

The first integral in Equation 9 is a constant, corresponding to the total energy from the source that enters the interferometer. The second integral is equivalent to the cosine transform of $\frac{I_s(\bar{\nu})}{2}$, or the real part of the Fourier transform, as discussed in the next section. For now, Equation 9 can be rewritten in terms of the constant $C = \int_0^{\infty} I_s(\bar{\nu})d\bar{\nu}$ and $F(\Delta) = 2\int_0^{\infty} \frac{I_s(\bar{\nu})}{2}\cos(2\pi\bar{\nu}\Delta)d\bar{\nu}$ as:

$$
F(\Delta) = I(\Delta) - C \tag{10}
$$

3.3 Fourier Transform Fundamentals

The integral form of the Fourier transform can be written as a transform pair [10]:

$$
\begin{aligned}
F(s) &= \int_{-\infty}^{\infty} f(x)\exp(-i2\pi xs)dx \\
f(x) &= \int_{-\infty}^{\infty} F(s)\exp(j2\pi xs)ds
\end{aligned} \tag{11}
$$

The even part of a Fourier transform of $f(x)$ equals the cosine transform of the even part of $f(x)$. If $f(x)$ is an even function, the following cosine Fourier transform pair applies [10]:

$$
\begin{aligned}
F_c(s) &= 2\int_0^{\infty} f(x)\cos(2\pi sx)dx, \quad s > 0 \\
f(x) &= 2\int_0^{\infty} F_c(s)\cos(2\pi sx)ds, \quad x > 0
\end{aligned} \tag{12}
$$

The second integral in Equation 9, which defines the non-constant interference term due to a polychromatic source, is rewritten below:

$$F(\Delta) \;=\; 2\int_0^\infty \frac{I_s(\bar\nu)}{2}\cos(2\pi\bar\nu\Delta)d\bar\nu \tag{13}$$

Equation 13 represents an idealized version of the signal that is measured by the interferometer. A Michelson interferometer consists of non-ideal optical components, each of which will introduce some wavenumber-dependent factors to the output signal. Among these are the beamsplitter efficiency, detector response, and amplifier characteristics, which can be lumped together as a correction-factor, $H(\bar\nu)$. [25]

Allowing $B(\bar\nu) = H(\bar\nu)\frac{I_s(\bar\nu)}{2}$, results in the following modification to the interferogram defined in Equation 13:

$$F(\Delta) \;=\; 2\int_0^\infty B(\bar\nu)\cos(2\pi\bar\nu\Delta)d\bar\nu \tag{14}$$

Its conjugate transform pair can be similarly written as:

$$B(\bar\nu) \;=\; 2\int_0^\infty F(\Delta)\cos(2\pi\bar\nu\Delta)d\Delta \tag{15}$$

Equation 15 suggests that values of Δ are taken in infinitesimally small increments from 0 to ∞. The OPD for an interferometer is limited by mirror displacement, x, to a value of $\Delta = 2x = L$. By defining a boxcar function as:

$$\begin{aligned} D(\Delta) &= 1, \quad 0 \le \Delta \le L \\ D(\Delta) &= 0, \quad otherwise \end{aligned} \tag{16}$$

and its corresponding Fourier transform as:

$$
\begin{aligned}
J(\bar{\nu}) &= \mathcal{F}\{D(\Delta)\} \\
&= \frac{\sin(2\pi\bar{\nu}L)}{2\pi\bar{\nu}L} \\
&= sinc(2\pi\bar{\nu}L)
\end{aligned}
\tag{17}
$$

Equation 15 can be further modified by applying the boxcar function as follows:

$$
B'(\bar{\nu}) = 2\int_0^\infty F(\Delta)D(\Delta)\cos(2\pi\bar{\nu}\Delta)d\Delta
\tag{18}
$$

where $B'(\bar{\nu})$ is defined as the convolution of $B(\bar{\nu})$ with $J(\bar{\nu})$, described below:

$$
B'(\bar{\nu}) = B(\bar{\nu}) \bigotimes J(\bar{\nu})
\tag{19}
$$

Finally, data will be sampled in every δt seconds or, alternatively, in OPD increments of $\delta\Delta = 2V\delta t$. Consequently, a discrete Fourier cosine transform is more applicable. By sampling the interferogram represented by Equation 18 in equal intervals of $\delta\Delta$ with the first sample captured at ZPD and the last at $\Delta = L$, a total of $N = 1 + \frac{L}{\delta\Delta}$ samples are obtained, and the following discrete cosine transform pair is used [10]:

$$
\begin{aligned}
F(\Delta) &= \sum_{\bar{\nu}=0}^{N-1} B'(\bar{\nu})\cos(\frac{2\pi\bar{\nu}\Delta}{N})d\bar{\nu} \\
B'(\bar{\nu}) &= \frac{2}{N}\sum_{\Delta=0}^{N-1} F(\Delta)D(\Delta)\cos(\frac{2\pi\bar{\nu}\Delta}{N})d\Delta
\end{aligned}
\tag{20}
$$

3.4 Imaging Fourier Transform Spectrometer

Imaging Fourier Transform spectrometers exploit the functionality of a Michelson inteferometer with added imaging capability. Associated with any imaging system is its étendue, or optical throughput. Another commonly used term for this is the $A\Omega$ product, since optical throughput is, by definition, the product of area (A) and solid

angle, Ω.

A lens system is used in the foreoptics of an IFTS to collimate the light associated with the object scene. The collimated light enters the Michelson interferometer, which has a mirror that moves with velocity, V, as defined previously. The output of the Michelson interferometer is projected onto an FPA with a focusing lens, and the spatial extent of the object scene is retained in the image scene (FPA data). As discussed in the previous section, discrete cosine Fourier transforms must be implemented to retrieve the spectral information of the scene in the desired form. The resulting hyperspectral image consists of one spectral and two spatial dimensions.

3.5 Telops FIRST System

Telops, Inc. has developed two imaging Fourier Transform spectrometers for chemical detection applications. The LWIR system (FIRST-LW) has been developed and used in testing by several groups, some of which have published results that were described previously in Chapter II. The FIRST-LW system design and performance have been detailed in [14; 15; 79; 21; 22], and are summarized in the subsection that follows. The MWIR system (FIRST-MWE) was delivered to AFIT in April 2008, and this one-of-a-kind system was used for this research. The design and performance of the FIRST-MWE system is presented at the end of this section, and in Chapter IV.

3.5.1 Telops FIRST-LW.

The FIRST-LW is a non-scanning IFTS with an MCT FPA, which allows it to operate effectively in the LWIR (8-11.5 μm). It is a field-portable instrument that has been used to detect gases and chemicals, such as SF_6, NH_3, Phosgene, TEP, DMMP, and composite mixtures (i.e., SF_6 and NH_3), released from smokestacks at a standoff distance of 500 meters. Spectral resolution is variable between 0.25 cm^{-1} and 150

cm^{-1}. With a relatively high spectral resolution of 4 cm^{-1} and a 320x128 pixel image (0.35 mrad pixel FOV), chemicals can be tracked as the plume trails away from the source, due to the high frame rate of 1 hyperspectral datacube every 4 seconds. [22]

3.5.2 Telops FIRST-MWE.

The FIRST-MWE is also a non-scanning IFTS, but uses an InSb FPA, which is best suited for imaging in the MWIR (1.5-5.5 μm). As with the FIRST-LW, it has an adjustable spectral resolution of 0.25-150 cm^{-1}, and an individual pixel FOV of 0.35 mrad. The InSb FPA has 320x256 pixels, and uses a 16-tap read-out integrated circuit (ROIC) as opposed to the 4-tap ROIC in the FIRST-LW system. Due to increased sampling required in the MWIR, the additional taps on the ROIC does not result in additional performance capability over the 4-tap LWIR instrument. Instrument performance of the FIRST-MWE follows in the next chapter, in addition to some early work on analysis of MWIR IFTS combustion events.

IV. Preliminary Results

4.1 Introduction

Fourier transform spectrometry of combustion events has been utilized in a non-imaging sense for characterization of explosive detonation fireballs in recent years [26]. For these high-temperature events, the midwave infrared (MWIR) region of the electromagnetic spectrum is well-suited, and it has been postulated that hyperspectral imagery of the explosive detonation scene will result in an improved capability to remotely characterize these fireballs. The Telops, Inc. FIRST-MWE (Field-portable Imaging Radiometric Spectrometer Technology - Midwave Extended) was acquired, and initial testing of the instrument demonstrated some of its unique capabilities in this regard. In addition to the explosive detonation research that the Air Force Institute of Technology (AFIT) Remote Sensing group has been actively involved with for the past ten years, a new path is being paved with a goal of remote detection and characterization of sources that approach ambient temperature. As a starting point in this vein of research, we have taken an initial step down this path without deviating from our expertise in combustion events by collecting hyperspectral data from the plumes of a propane torch and diesel-filled jet engine.

4.2 Telops FIRST-MWE Spectro-radiometric Performance

The FIRST-MWE is an imaging Fourier transform spectrometer with a spectral range of 1800-6667 cm^{-1} (1.5-5.5 μm) and user-defined spectral resolution between 0.25-150 cm^{-1}. It has a Stirling-cooled InSb (Indium Antimonide) focal plane array (FPA) that consists of 320x256 pixels. The spatial extent of the scene can be windowed to improve temporal resolution with a smaller field of view. The FIRST-MWE has an individual pixel field of view (IFOV) of 0.35 mrad and uses a 16-tap read-out

integrated circuit (ROIC) to achieve fast data rates. Interferogram time is entirely dependent on instrument settings. For example, it takes just over 2.5 seconds to record a single frame interferogram with the instrument set to a spatial window of 128x128 pixels, integration time of 7 μs, and a spectral resolution of 1 cm^{-1}. Similarly, the same spatial and temporal settings (128x128 pixels and 7 μs integration time) with a spectral resolution of 16 cm^{-1} results in a single frame interferogram in just over 100 ms. In this work, we obtained an interferogram of a 32x32 pixel scene, with a 30 μs integration time, and a spectral resolution of 0.25 cm^{-1} in 3.68 seconds. In addition to the spectral mode, which uses a Michelson interferometer with one fixed and one moving mirror to resolve spectral information, the moving mirror can be fixed by setting the FIRST-MWE to camera mode. In camera mode, high-speed broadband (1.5-5.5 μm) IR imagery can be recorded at up to 350 Hz for a 320x256 pixel scene and up to 4.8 kHz for a 128x128 pixel scene.

4.2.1 Spatial Characterization.

With the spectral resolution set to 32 cm^{-1} and an integration time of 50 μs, hyperspectral imagery of a 3 inch external blackbody at 65°C was recorded using a 32x32 pixel window. The resulting interferogram from each pixel was Fourier transformed, giving its corresponding uncalibrated spectra. Instrument gain and offset curves were computed using the two-blackbody calibration process detailed in [21] using the two internal instrument blackbodies set to temperatures of 40°C and 80°C. The instrument gain and offset curves were applied to the uncalibrated data, resulting in calibrated spectra at each pixel. Using a nonlinear least-squares fitting routine, this pixelated spectra (which includes atmospheric absorption from source to instrument) was fitted to a Planckian curve, as defined in [17] and displayed in Equation 21 in terms of W/(cm$^2\cdot$ sr $\cdot$ cm^{-1}):

$$L_{BB}(\nu, T) = \frac{2hc^2\nu^3}{\exp(\frac{hc\nu}{k_B T}) - 1} \tag{21}$$

where ν is the spectral value in wavenumbers (cm^{-1}), h is Planck's constant, k_B is Boltzmann's constant, and c is the speed of light in vacuum (cm/s). The fitting routine assumes the blackbody to be ideal with unit emissivity, and ignores the spectral region of high CO_2 atmospheric absorption from 2200-2400 cm^{-1}. The resulting fit of a single pixel data to its corresponding best-fit Planckian model is depicted graphically in Figure 1. This resulted in a corresponding Planckian temperature for each pixel. A spatial map of the resulting temperature profile is shown in Figure 2. The blackbody function in Equation 21 was inverted to solve for temperature for the center pixel at all spectral bins between 1800 and 2100 cm^{-1}. This resulted in a mean temperature of 64.51^oC and standard deviation of 0.29^oC. Due to the nearly 0.5^oC bias between the external blackbody temperature and the mean fitted temperature value, an analysis of spatial uniformity followed. Using the same spectral region as in the single-pixel case, a least squares fit of pixel spectra to a Planckian function was performed on each pixel in the 32x32 pixel FOV. As with the single-pixel temperature calculated by inverting the Planckian function, the mean fitted temperature over all pixels in the 32x32 pixel FOV was 64.51^oC, with a spatial temperature standard deviation of 0.15^oC. For both spatial and single-pixel temperature measurements, the mean calculated temperature was 0.49^oC less than the blackbody temperature setting of 65^oC, with standard deviation within an order of magnitude of values of noise equivalent temperature difference (NETD) that have been reported for MWIR camera systems [65]. Further investigation will need to be accomplished to determine the cause of the temperature bias, but it is likely due to either improper calibration of the 3 inch external blackbody or one of the two internal instrument blackbodies.
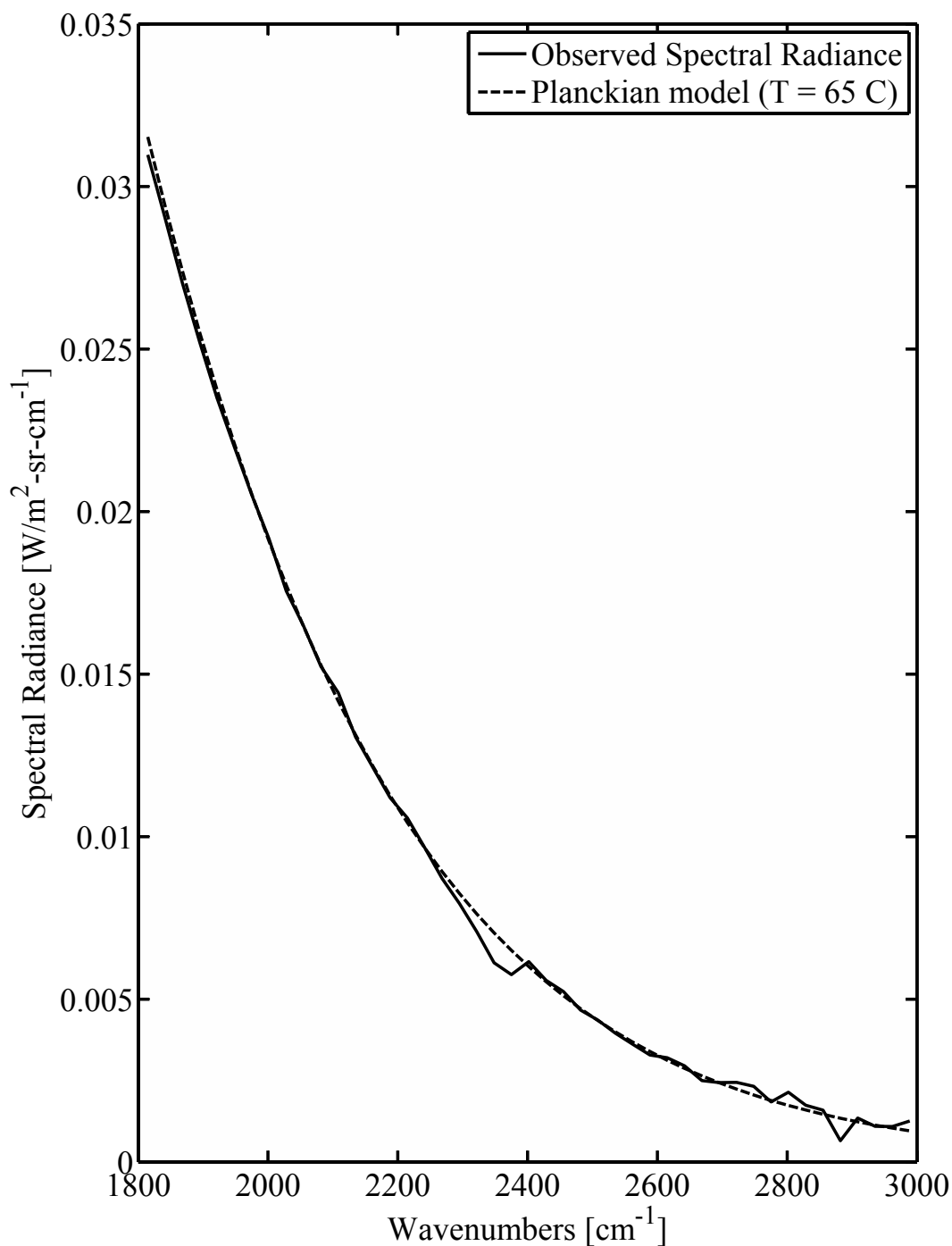
Figure 1. Nonlinear least squares fit of Planckian function to the spectra of an individual scene pixel. The hyperspectral image associated with this plot is a 32x32 pixel view of a 3 inch blackbody at 65°C. The region of high CO_2 absorption (2200-2400 cm^{-1}) was ignored to eliminate the need of atmosphere inversion prior to fitting the measured pixel spectra to the Planckian model.

28
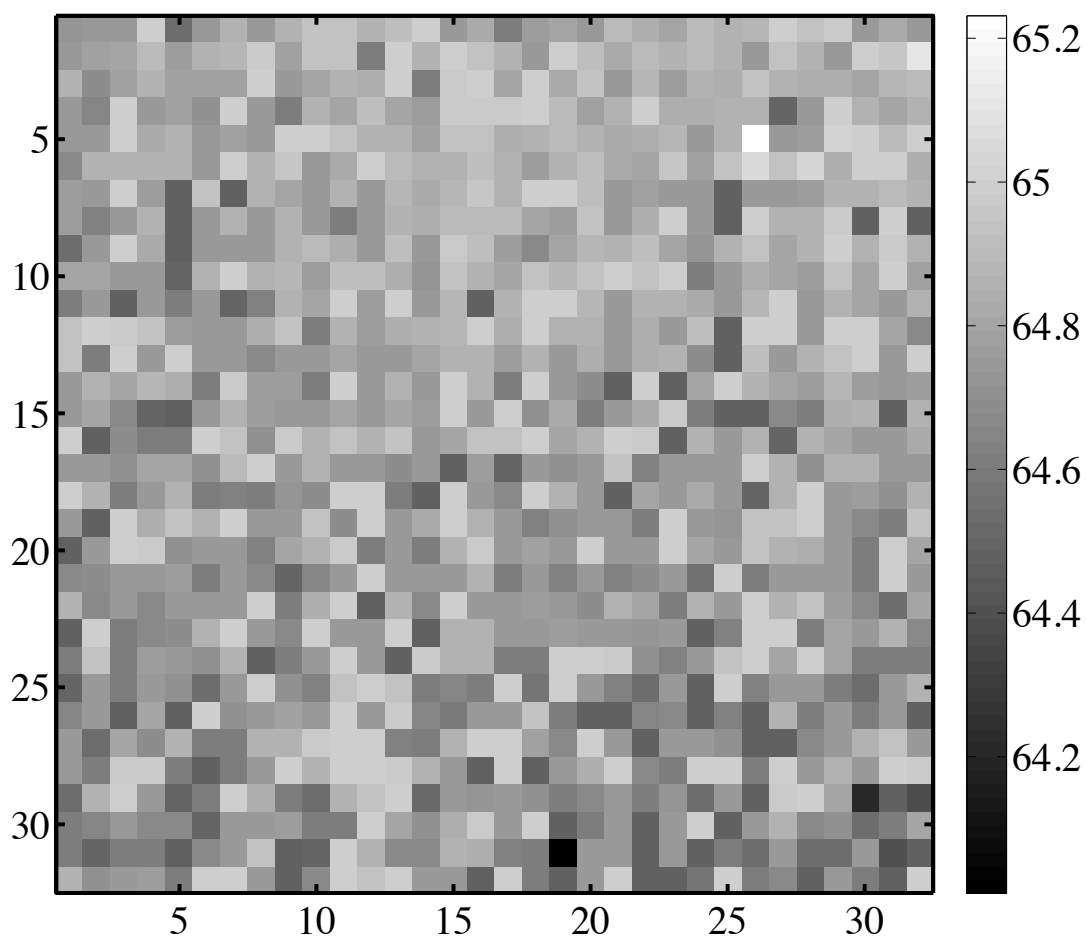
Figure 2. Spatial temperature profile of a 3 inch blackbody at 65°C, obtained by a nonlinear least squares fit of a Planckian function to each pixel's spectra as shown in Figure 1 for a representative pixel.

4.2.2 Spectral Characterization.

The Telops FIRST-MWE has a variable spectral resolution, with user-defined settings ranging from 0.25 - 150 cm^{-1}. To characterize the spectral resolution capabilities of the instrument, a 12 inch blackbody set to a temperature of 150 ^{o}C was placed a distance of 10 meters from the FIRST-MWE. The FIRST-MWE was set to a spectral resolution of 0.25 cm^{-1} with a 128x128 pixel window. Figure 3 plots the spectral radiance from a single pixel along with the atmosphere model obtained using a non-linear least squares fit of the data with atmospheric parameters of temperature, H_2O concentration, and CO_2 concentration, from a line-by-line radiative transfer model (LBLRTM) based on the HITRAN database.

Figure 4 zooms in on the spectral region from 1800-2100 cm^{-1}, depicting the close fit of the atmospheric model to the data in the region where absorption due to water lines is prevalent.

4.2.3 Noise Characterization.

Noise Equivalent Spectral Radiance (NESR) is often used when discussing Fourier Transform Spectrometer performance, since it defines the minimum source spectral radiance required for a signal-to-noise ratio (SNR) of one. The theoretical and measured NESR of the FIRST-LW (the longwave version of the Telops FIRST Imaging Fourier Transform Spectrometer) have been published previously [22] using radiometric calibration, as presented in [21].

NESR is calculated in theory using the following relation [21]:

$$NESR = \frac{NEP}{0.5 \cdot \tau \cdot ME \cdot \Theta \cdot \Delta\nu \cdot t^{\frac{1}{2}}} \tag{22}$$

where NEP is the noise equivalent power [W/Hz$^{\frac{1}{2}}$], τ is the sensor transmittance, ME is the modulation efficiency, Θ is the single pixel throughput [m$^2\cdot$ sr], $\Delta\nu$ is the
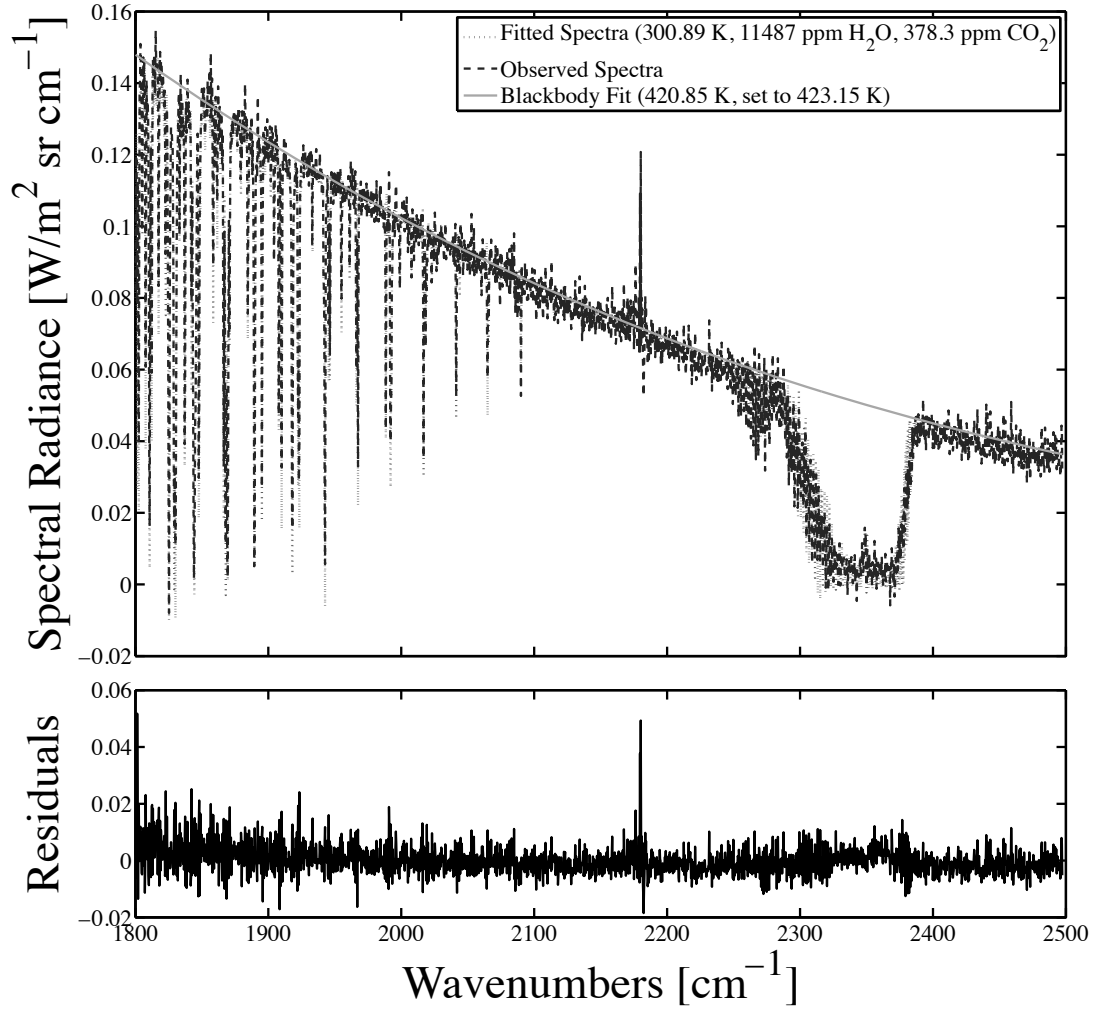
Figure 3. Measured spectral radiance of the atmosphere and the associated temperature and chemical concentrations of CO_2 and H_2O in the environmentally-controlled laboratory. Temperature and chemical concentrations were determined by a nonlinear least squares fit of the measured data to a line-by-line radiative transfer model (LBLRTM) of the atmosphere based on HITRAN database values at the instrument spectral resolution of 0.25 cm^{-1}. Residuals (Data - Model) is also plotted in terms of spectral radiance.
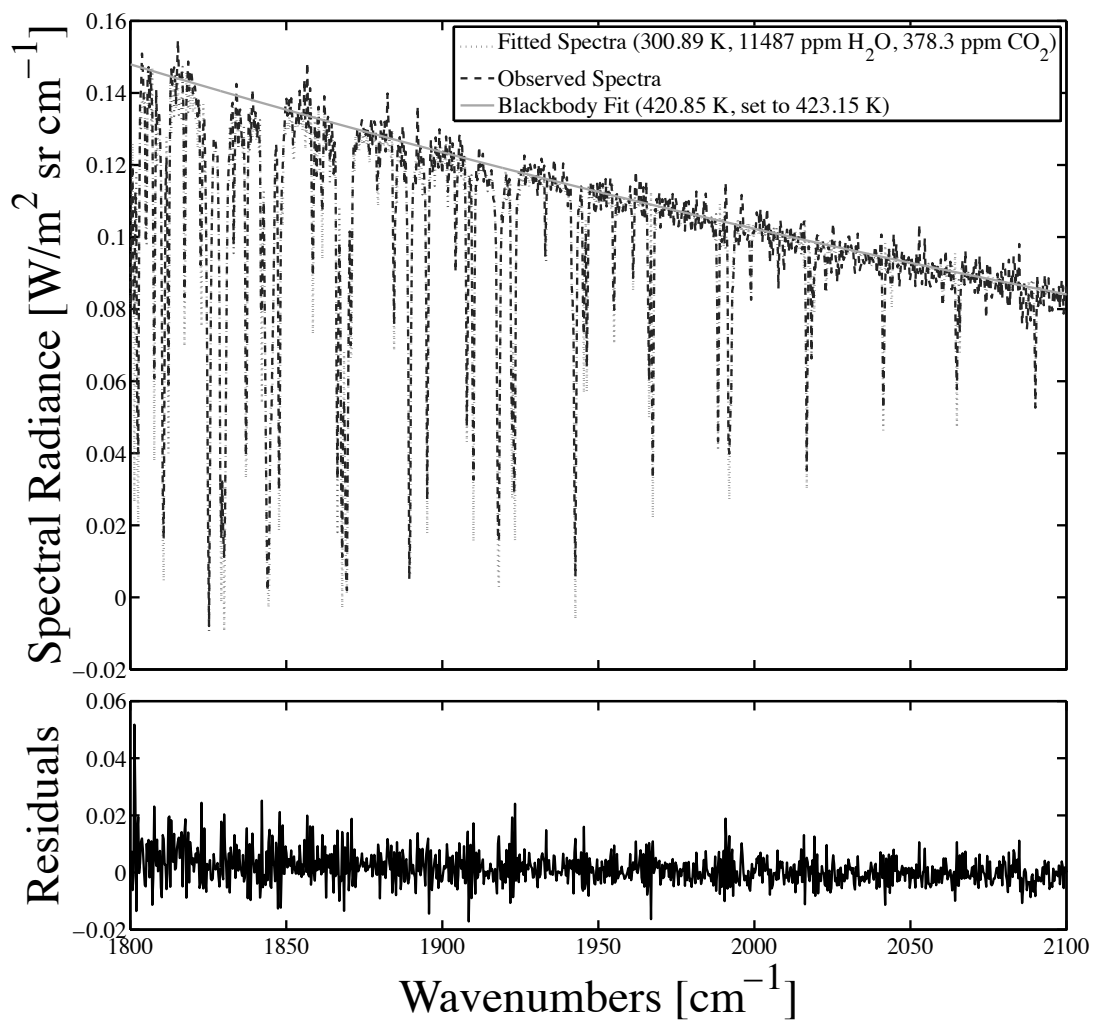
Figure 4. Close-up of 1800-2100 cm^{-1} region of spectra to view fit of modelled versus measured atmospheric water absorption lines. Residuals (Data - Model) are also plotted in terms of spectral radiance.

spectral bin spacing [cm^{-1}], and t is the measurement time [s].

NESR measurements are taken utilizing the radiometric calibration procedure detailed in [21], which describes the instrument response by a linear expression consisting of instrument gain and offset. Measurements from the FIRST-MWE can be expressed as follows [21]:

$$\bar{M}(\nu) = \bar{G}(\nu) \cdot (L(\nu) + \bar{O}(\nu)) \tag{23}$$

where $\bar{M}(\nu)$ is the complex measured spectrum [a.u. (arbitrary units)], $\bar{G}(\nu)$ is the complex instrument gain [a.u./(W/m$^2 \cdot$ sr $\cdot$ cm^{-1})], $L(\nu)$ is the true spectral radiance of the scene [W/m$^2 \cdot$ sr $\cdot$ cm^{-1}], and $\bar{O}(\nu)$ is the complex instrument offset [W/m$^2 \cdot$ sr $\cdot$ cm^{-1}].

Using the two internal blackbodies of the FIRST-MWE, set at a cold and hot temperature, respectively, and assuming the detector has a linear response, the complex gain and offset functions, $\bar{G}(\nu)$ and $\bar{O}(\nu)$, can be solved for directly. $L(\nu)$ for each of the internal blackbodies is assumed to be equivalent to an ideal blackbody function of unit emissivity at its temperature. [22]

With the FIRST-MWE properly calibrated, scene measurements of an external blackbody (also assumed to be ideal) were collected. The measured NESR is the temporal standard deviation of the radiance of this ideal, non-varying scene for each spectral bin. [22]

The NESR of the FIRST-MWE was measured for a 128x128 pixel window at 32 cm^{-1} spectral resolution using a blackbody at 25°C. The resulting NESR was plotted and overlayed with Planckian curves of blackbodies at temperatures characteristic of sources of interest to our current and future research efforts in Figure 5.

Since the Telops FIRST-MWE is a one-of-a-kind instrument, operational testing of the instrument is in its early stages. As such, a few hardware and software
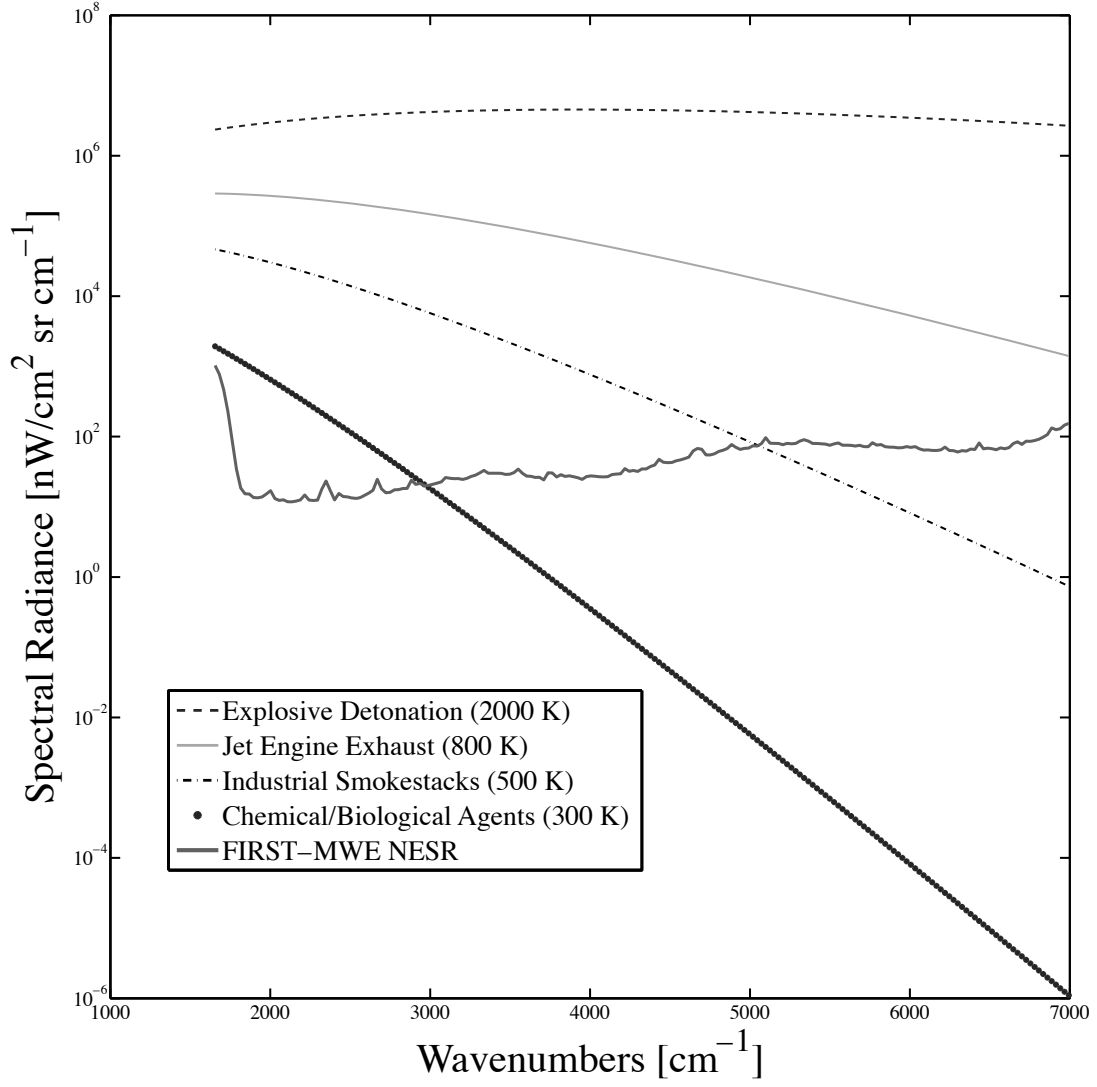
Figure 5. Measured Noise Equivalent Spectral Radiance (NESR) of Telops FIRST-MWE compared to modelled spectral radiance of blackbody sources at temperatures of interest. NESR was measured using a 128x128 pixel window and 32 cm^{-1} spectral resolution.

problems were encountered during our recent field tests, which have demonstrated themselves in the data as additional sources of noise. Improvements to the FIRST-MWE in the near future are expected to remove or significantly decrease the effects of several sources of instrument noise associated with the FPA and Stirling cooler. Included in these is a software modification to the servo loop that controls the Stirling cooler to dramatically reduce the vibration-induced noise and a modified read-out integrated circuit (ROIC). These instrument modifications are expected to decrease the system NESR by nearly an order of magnitude, significantly increasing the utility of the instrument for imaging near-ambient temperature sources, such as chemical and biological threat agents.

4.3   Propane Torch

Following instrument characterization, the FIRST-MWE was used to collect hyperspectral and broadband IR imagery of a propane torch. The torch was positioned immediately in front of a 12 inch blackbody set to a temperature of 65^oC, as depicted in Figure 6.

Hyperspectral imagery of the scene was collected with the FIRST-MWE set to a 128x128 pixel window, 16 cm^{-1} spectral resolution, and 20 μs integration time. The window size was selected based on the field of view of the desired scene, which consists of part of the torch, the entire plume, and the blackbody background. With the field of view selected, integration time was chosen based on the desire to have between 80 and 85 percent saturation of the FPA at the hottest pixel, increasing signal-to-noise without saturating the FPA. A modest spectral resolution of 16 cm^{-1} was selected to ensure a high level of signal-to-noise in the data. Temporal information was not important for this particular data collection, but improving spectral resolution would result in a loss of temporal information (fewer frames per second). Figure 7 presents
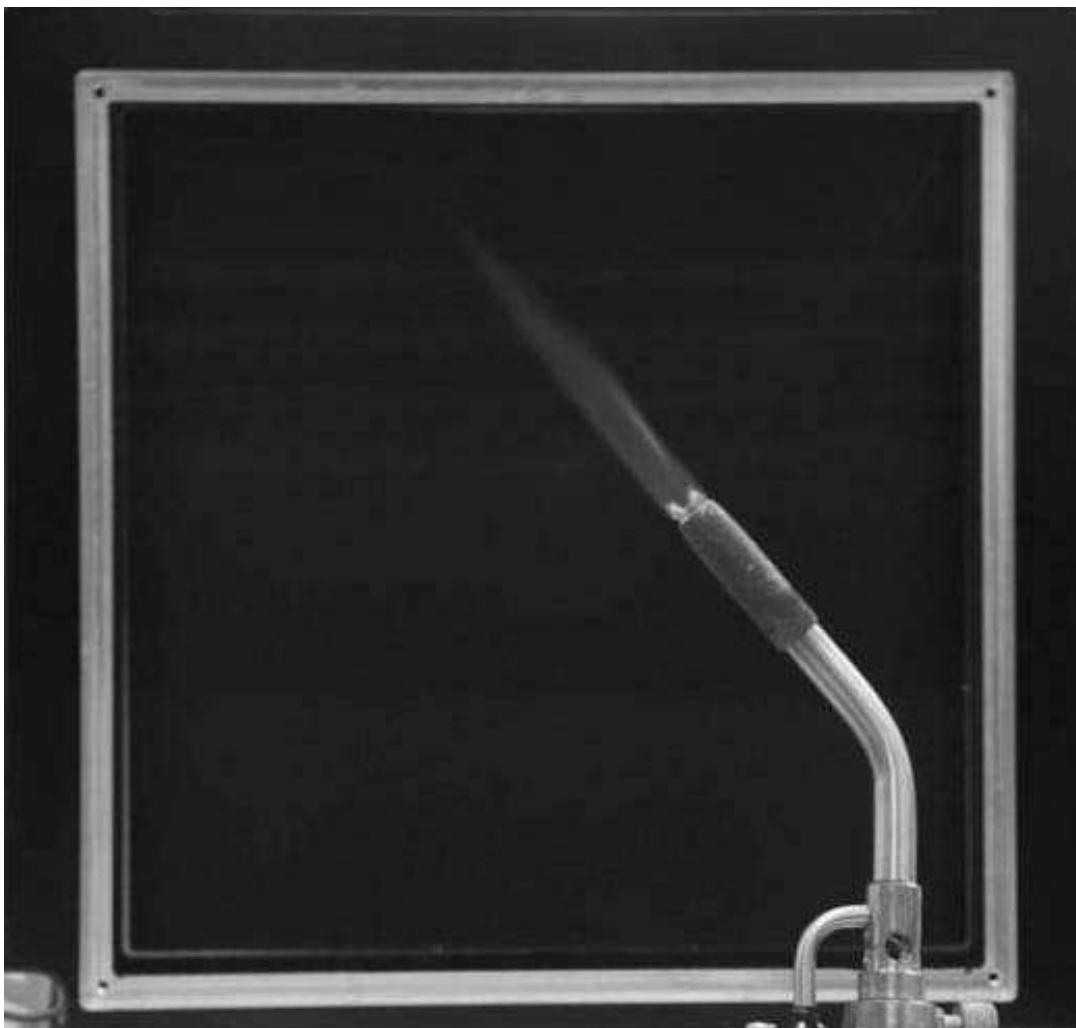
Figure 6. Experimental Setup to collect propane torch spectra. The propane torch was locked in place directly in front of a blackbody background source at 65°C. The FIRST-MWE was set to a spectral resolution of 16cm^{-1} and windowed to a spatial view of 128x128 pixels. Data was collected in both spectral and camera modes.

an IR image of the torch scene that was extracted from the hyperspectral data.
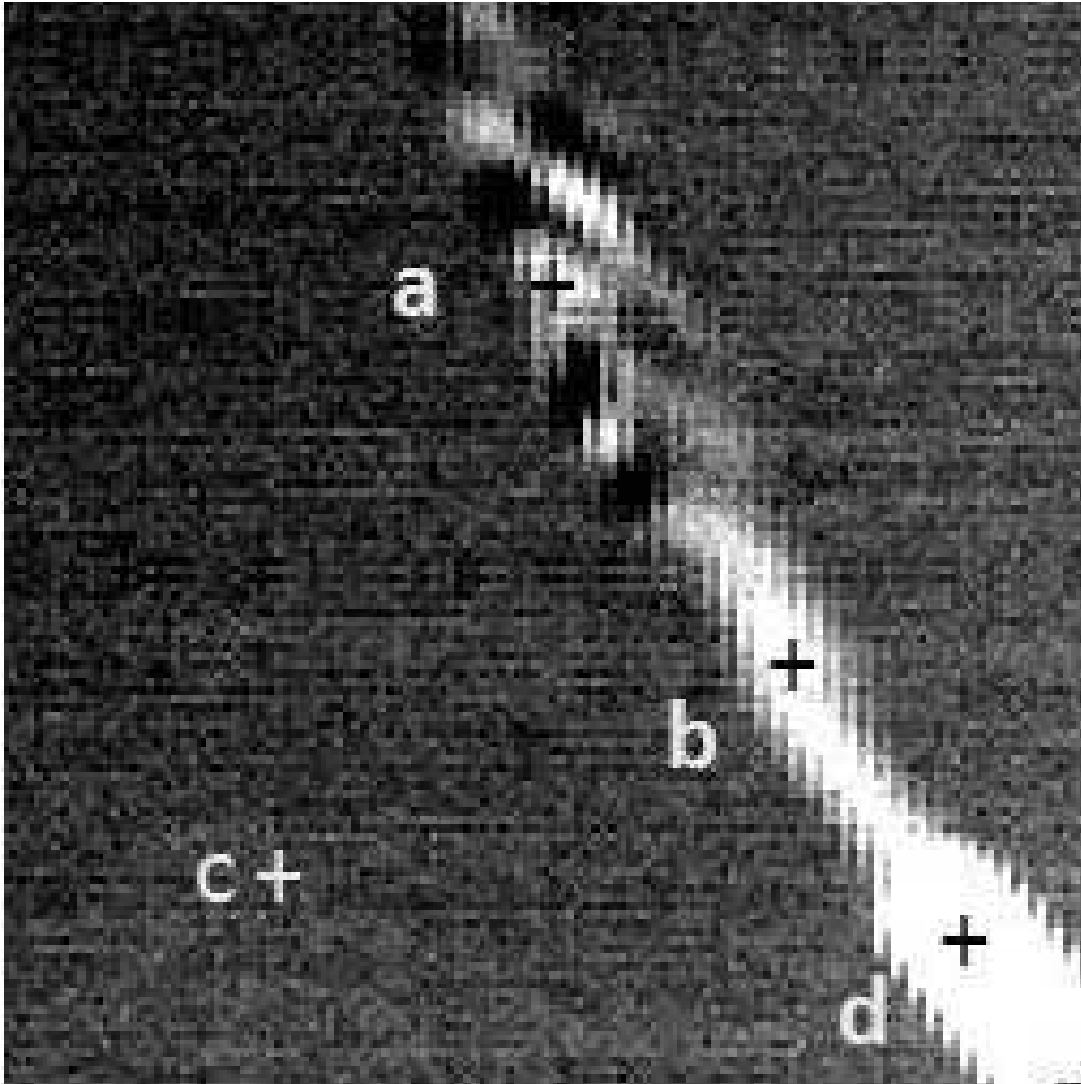
Figure 7. IR image of torch scene, with four objects of interest labelled within the scene: (a) flickering plume, (b) hot steady plume, (c) blackbody background source, and (d) hot metal torch.

Figure 8 shows the characteristic spectra of each of the four identified constituents within the scene. Subimage (a) of Figure 8 depicts the spectra characteristic of a flickering plume. Due to the rapidity with which the plume scene changes away from the tip of the metal torch, scene change artifacts (SCAs) are imposed on each frame of the hyperspectral datacube. The SCAs due to the plume flicker result in a mixed-pixel phenomenon between plume and blackbody background source. As a result, the

37

flat baseline associated with the hot plume spectra in Figure 8(b) is not present in the flickering plume pixel, which has a more curved baseline near the edges of the CO_2 window (2100-2400 cm^{-1}). The negative spectral radiance values on either side of the CO_2 window further suggest that the curve in the spectra is an effect of SCAs, as opposed to contributions due to spectral emission from other molecules, such as H_2O. In both cases, however, the presence of hot CO_2 in the plume results in highly pronounced emission lines in this spectral region. Subimages (c) and (d) are both Planckian in nature, with the former a much colder temperature Planckian due to the low-temperature (65^oC) blackbody background source and the latter being hot Planckian-like emission due to the high-temperature metal torch. Unlike the plume pixel spectra in subimages (a) and (b), the torch pixel spectra in subimage (d) does not exhibit emission of hot CO_2. It does exhibit absorption of atmospheric CO_2 due to the cooler ambient atmosphere between the hot torch and the FIRST-MWE. Since the blackbody is near ambient temperature, no significant signal due to absorption or emission of CO_2 is present in the spectra of subimage (c).

Using the spectral characteristics of the propane torch scene, a hyperspectral detection algorithm was employed to automatically characterize pixels based on the difference of two measurements. The first measurement calculated the integrated spectral radiance associated with each pixel. The second measurement calculated the integrated spectral radiance within the CO_2 band (2100-2400 cm^{-1}). Each of these measurements was computed and normalized, upon which the difference between the two (normalized total radiance - normalized CO_2 radiance) was plotted as a two-dimensional spatial image. The resulting image segregated the scene into four regions of interest, as shown in Figure 9.

Due to the high volume of data contained in a hyperspectral scene, data reduction techniques are necessary before implementing more complex analysis. By applying
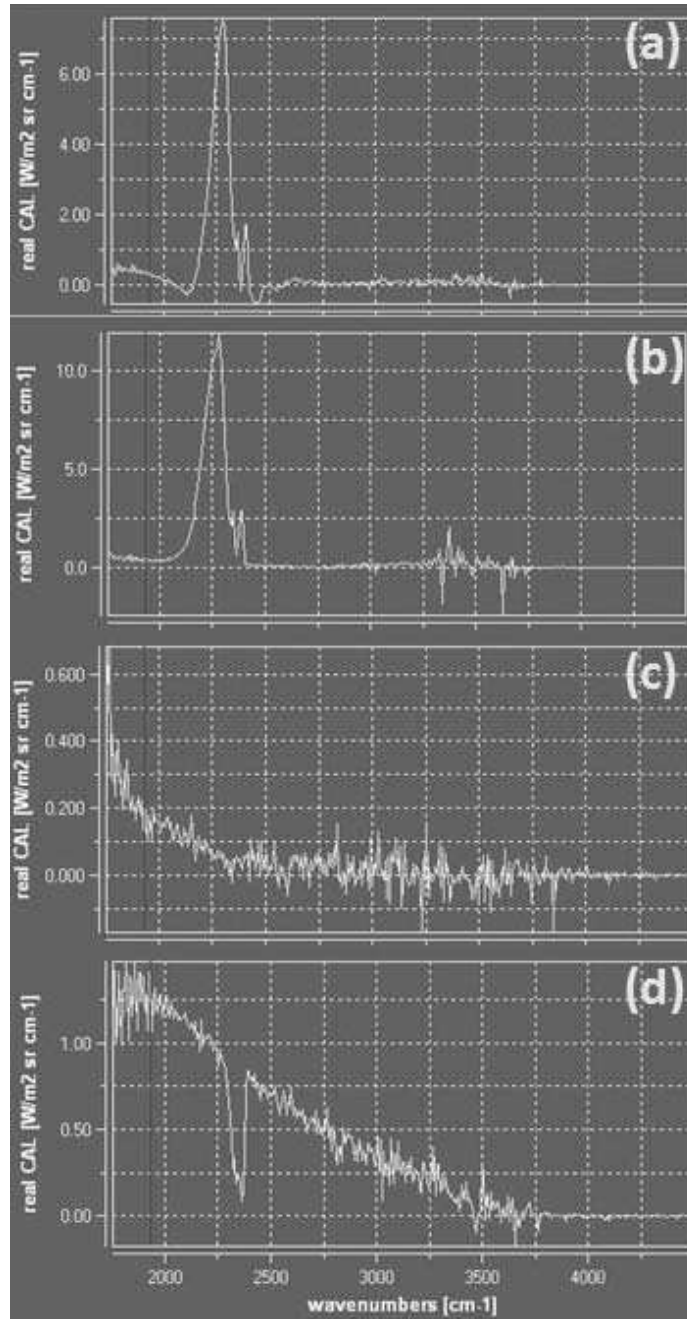
Figure 8. Spectra of four distinct items of interest within the IR scene (Figure 7): (a) flickering plume, (b) hot steady plume, (c) blackbody background source, (d) hot metal torch.
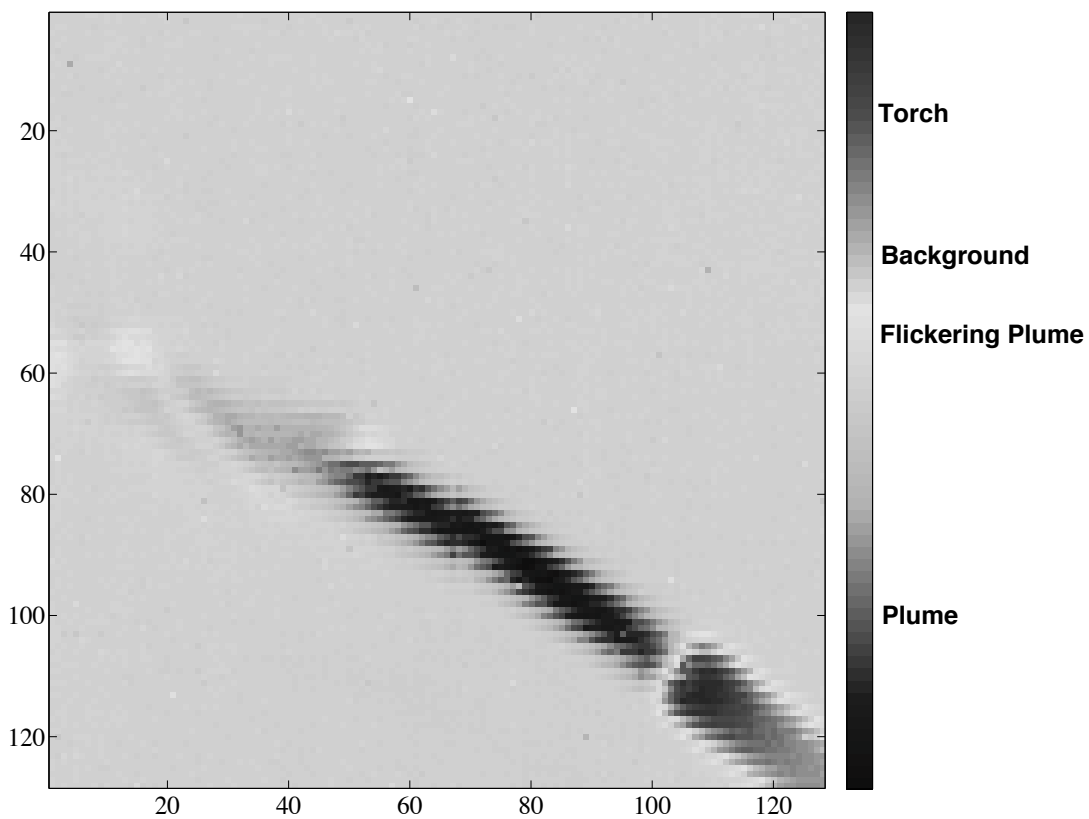
Figure 9. Hyperspectral detection technique based on subtraction of normalized CO_2 radiance from normalized total radiance.

an appropriate threshold to the normalized differential radiance function from the plume data, all plume pixels can be identified and extracted from the datacube. The remaining scene pixels can be ignored, reducing the dataset significantly for a more detailed chemical and temperature analysis.

4.4   Turbine Technologies, Ltd. SR-30 TurboJet Engine

The FIRST-MWE was used to collect hyperspectral imagery of the exhaust from a diesel-fueled Turbine Technologies, Ltd. SR-30 TurboJet engine. Figure 10 depicts the experimental setup, with a blackbody background source at 65^oC positioned directly behind the plume at a distance of 2 meters, and the FIRST-MWE a distance of 4 meters in front of the plume.

Figure 11 is an IR image of the exhaust plume taken from the vantage point described above. The engine was set to the highest thrust level, resulting in a temperature reading of 720^oC from the internal temperature gauge near the engine exhaust outlet. The FIRST-MWE was set to a spectral resolution of 8 cm^{-1} with an integration time of 20 μs and spatial window of 128x128 pixels. The window size was selected based on the field of view of the desired scene, which consists of part of the engine and the exhaust plume. With the field of view selected, integration time was chosen based on the desire to have between 80 and 85 percent saturation of the FPA at the hottest pixel, increasing signal-to-noise without saturating the FPA. A modest spectral resolution of 8 cm^{-1} was selected to ensure a high level of signal-to-noise in the data. Temporal information was not important for this particular data collection, but improving spectral resolution would result in a loss of temporal information (fewer frames per second).

Figure 12 contains the spectra of the plume within a truncated spectral region of 1800-3000 cm^{-1} for the plume pixel labelled with a cross in Figure 11. Although the
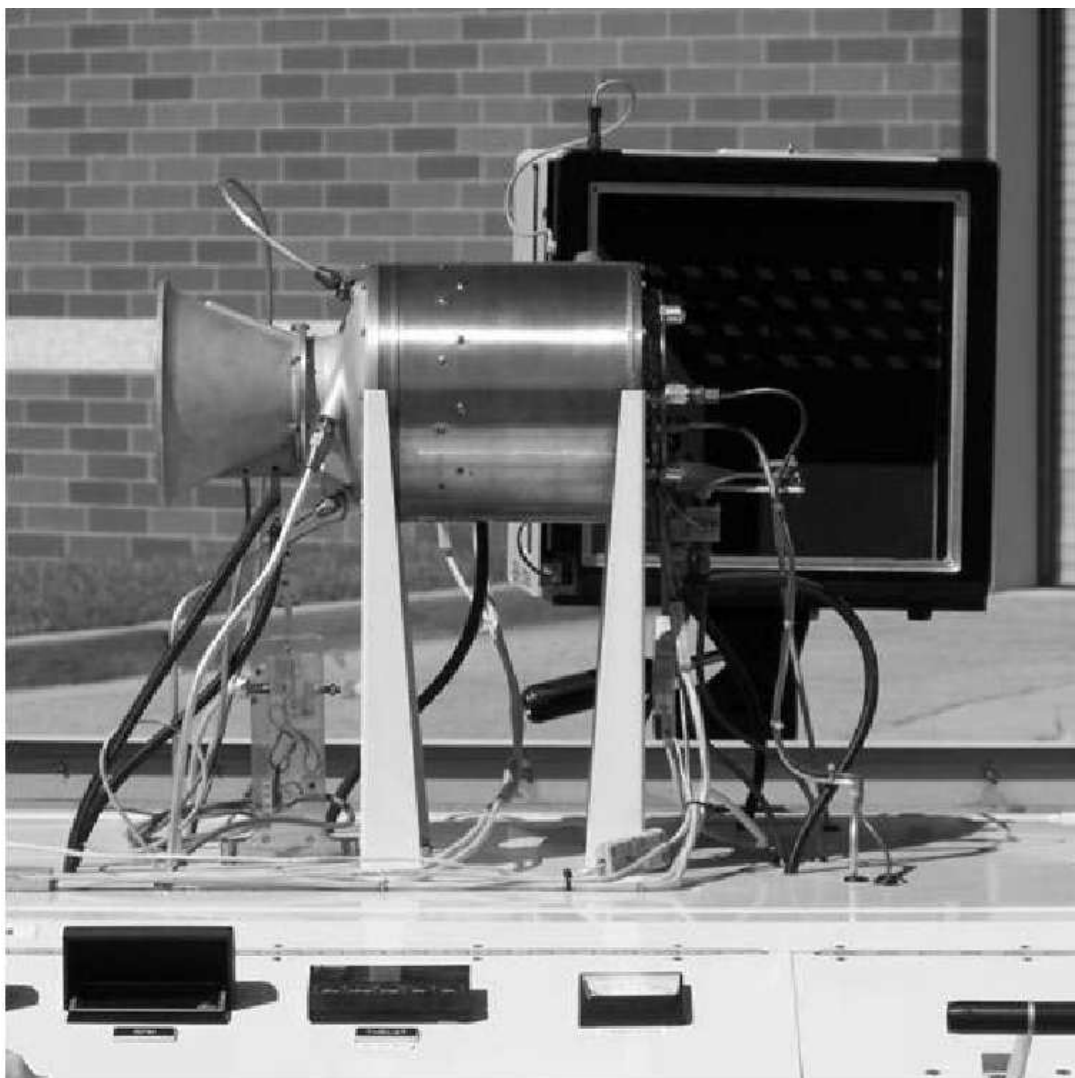
Figure 10. Experimental Setup to collect TurboJet Engine data.
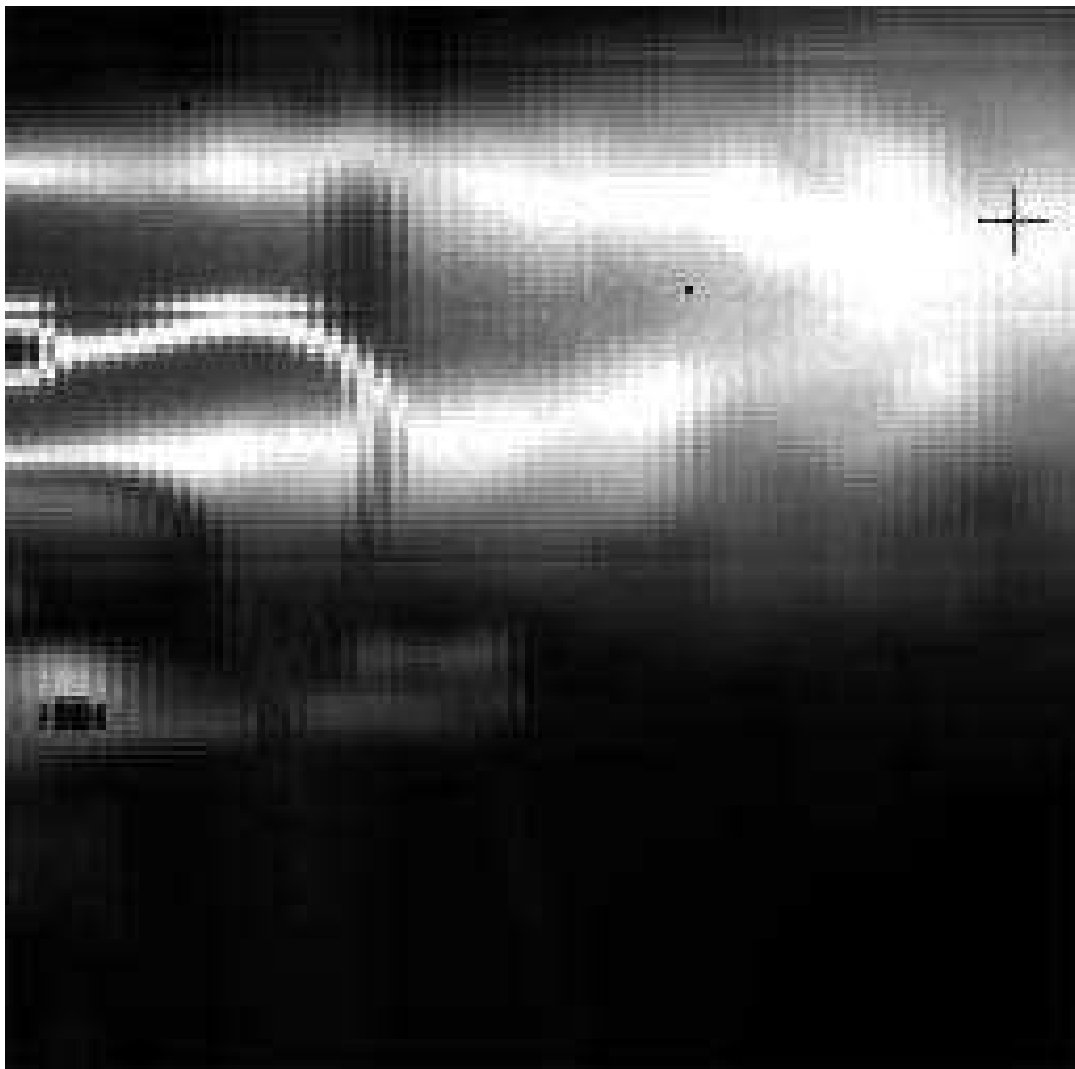
Figure 11. IR image captured by FIRST-MWE at 8 cm^{-1} spectral resolution of the exhaust plume from a diesel-fueled TurboJet Engine running at high thrust.

spectra is characteristically noisy, emission lines associated with hot CO_2 within the plume pixel are clearly visible between 2200-2400 cm^{-1}.

The FIRST-MWE also comes equipped with an optional telescope, allowing for long-distance remote sensing of plume sources. With the telescope fixed to the instrument, and the instrument settings as described previously, the FIRST-MWE was positioned a distance of 200 meters from the jet engine. Figure 13 depicts the IR image of the scene. Pixel (a) in Figure 13 contains the background. Pixel (b) is a hot plume pixel, pixel (c) consists of plume reflection either from the asphalt or internal optics, and pixel (d) is part of the hot metal engine near the exhaust outlet.
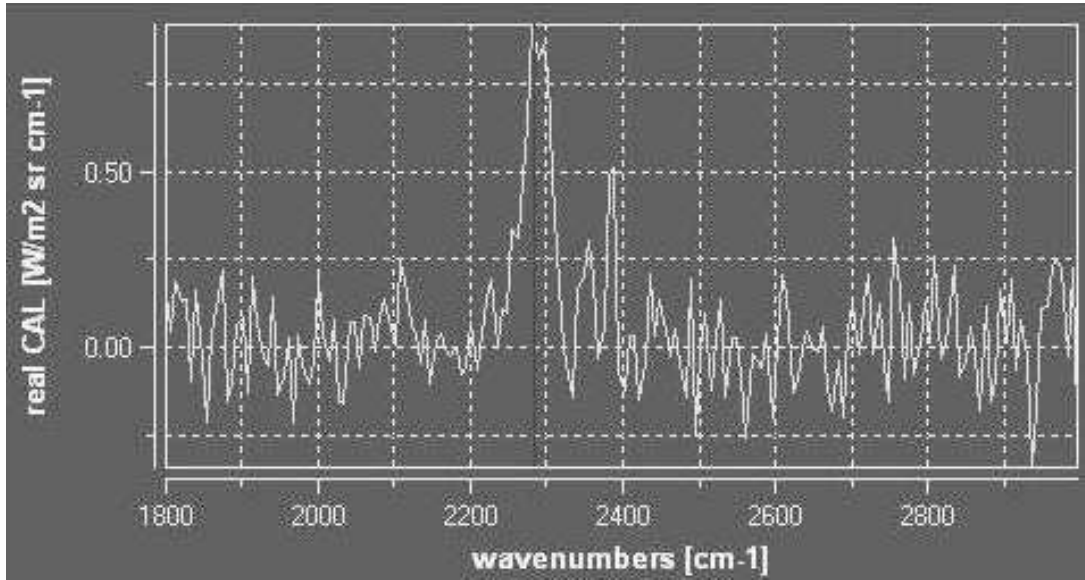
Figure 12. Spectrum associated with marked pixel in IR image of Figure 11.

Figure 14 shows the spectral signatures of each of the four pixels that are labelled in Figure 13. The background (a) and hot metal (d) both exhibit continuum Planckian-like emission. As with the torch data, CO_2 absorption is clearly discernible between 2200-2400 cm^{-1} in Figure 14(d), and much less evident in Figure 14(a), due to their respective temperature differences from ambient. Figure 14(b) clearly shows hot emission of CO_2, as does Figure 14(c), at a smaller scale due to the effect of

44
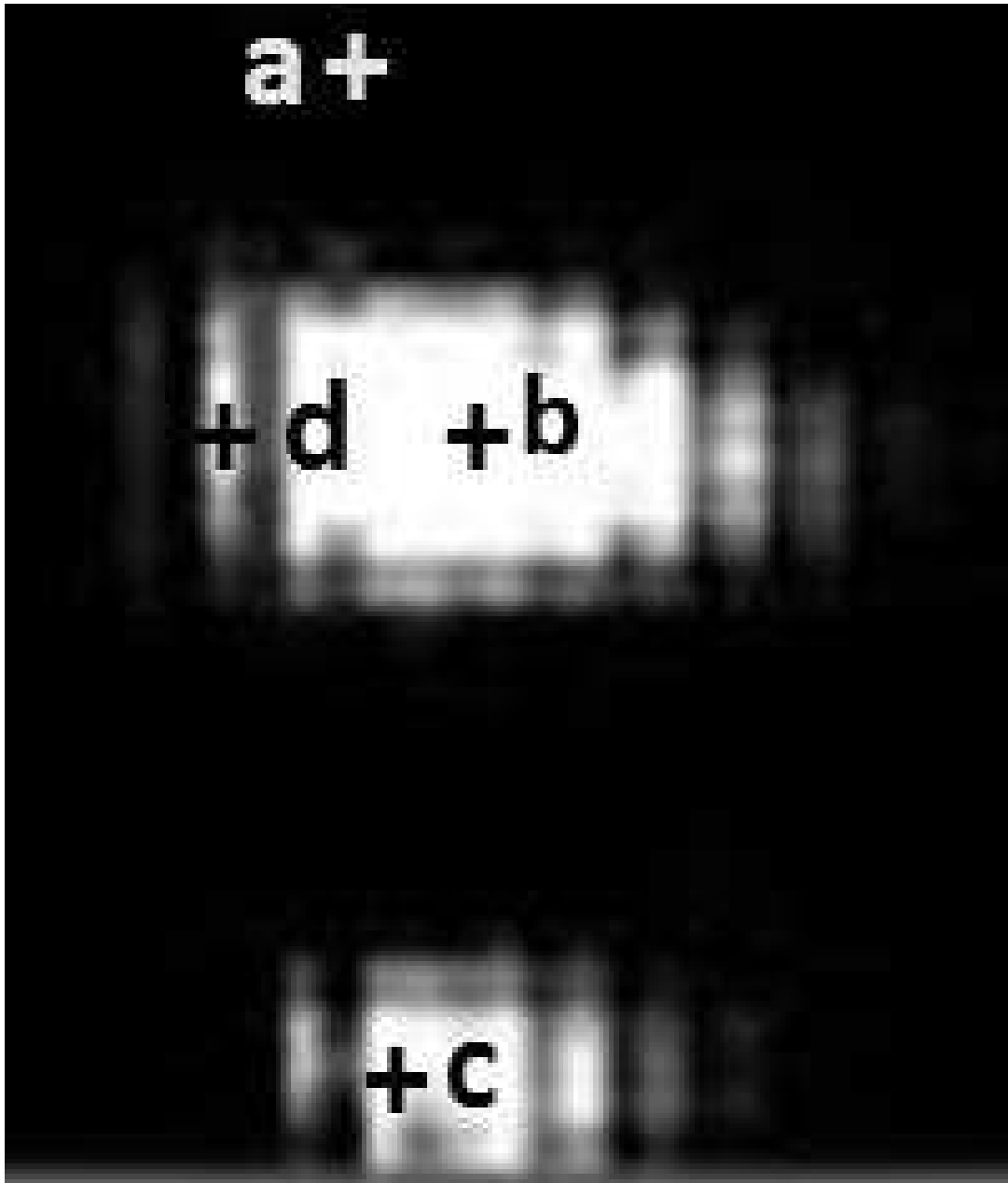
Figure 13. IR image of jet engine scene, with four objects of interest labelled within the scene: (a) background, (b) hot plume, (c) reflection of hot plume either from asphalt or internal optics , and (d) hot metal jet engine.

the reflectivity either from the asphalt or internal optics. Ghosting has been witnessed in other data collections, when viewing a scene with high spectral radiance that saturates the FPA at the hot pixel, and cannot be ruled out without further investigation.

4.5   Conclusions

Hyperspectral imagery of propane torch plumes and diesel-fueled jet engine exhaust were captured with the Telops FIRST-MWE to demonstrate the ability to analyze combustion events using imaging Fourier transform spectrometry. Spectra associated with individual scene pixels were used to categorize the scene content. Turbulent plumes introduce scene change artifacts (SCAs), due to the temporal response of the FIRST-MWE, whereas laminar flow, as seen in the plume near the base of the propane torch, exhibits less dynamic scene behavior. It has also been demonstrated that SCAs present themselves down-plume in more laminar flow fields due to mixing of the hot plume gases with ambient air. The SCAs associated with plume turbulence are expected to be problematic for the analysis of many combustion events, such as jet engine exhaust. Future work will employ a combination of time-averaging and spatial binning to decrease the extent to which SCAs affect the ability to characterize plumes, without significantly degrading the spatial and temporal resolution of the data. Time-averaging of flickering plume pixels will result in a weighted average of plume and background, with respective weights of the spectral features dependent upon the relative time in which each is present in the pixel of interest. It is expected that extracting plume temperature information from flickering plume pixels after temporal averaging may be more difficult due to this nonuniformity in the scene. Despite these challenges, which must be addressed, it is proposed that MWIR imaging Fourier transform spectrometry can be used to produce a spatial map of both
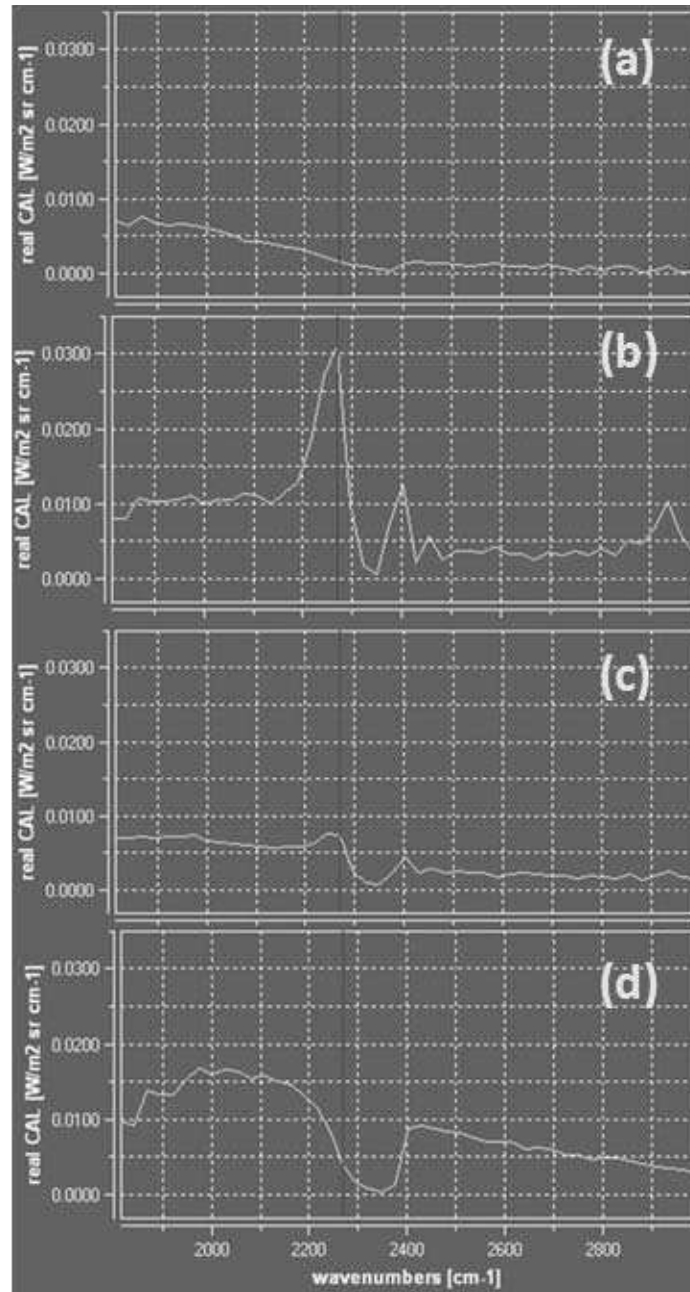
Figure 14. Spectra of four distinct items of interest within the IR scene (Figure 13): (a) background, (b) hot plume, (c) reflection of hot plume either from asphalt or internal optics, and (d) hot metal jet engine.

temperature and chemical concentrations of plumes from combustion sources.

V. Analysis of Jet Engine Exhaust IFTS Data

5.1 Introduction

The analysis of combustion systems requires the capability of assessing information about the exhaust plume. While thermocouples are often employed as combustion thermometers, they suffer some limitations. First, inserting a thermocouple into the plume is an invasive method of extracting temperature information. Second, extracting spatial information about the plume temperature using an array of thermocouples is both cumbersome and labor-intensive. Additionally, the introduction of thermocouples into the plume alters the downstream flow, and only a few temperature datapoints are able to be collected simultaneously. [47]

Several active optical techniques have been implemented in an attempt to extract plume temperatures remotely, with varying levels of success. The method of laser absorption spectroscopy (LAS) has been well established, and includes many techniques such as sum-frequency mixing [3], Coherent anti-Stokes Raman scattering (CARS) [56], H_2O thermometry [34], UV absorption of CO_2 [44], and direct absorption spectroscopy [46], but all of these methods are narrow-band, which limits the amount of information obtainable from active measurements.

Passive techniques may be the ideal solution, as they are non-intrusive and are capable of wide-band spectral measurements. Among passive techniques, Fourier transform spectrometry (FTS) is the method of choice for several reasons. FTS is both flexible and versatile. It enables the detection of many chemicals due to large spectral bandwidth, with spectral features obtained at a user-defined spectral resolution by setting the maximum optical path difference (MOPD) of the interferometer element. Previous work demonstrated the ability to extract jet engine exhaust plume information from spectra non-intrusively using non-imaging FTS [70]. Recent techno-

logical achievements have resulted in the ability to spatially scan a single-pixel FTS over the object scene (scanning imaging FTS) for the purpose of analyzing jet engine exhaust remotely during normal airport operations and obtaining spatially varying spectra [66].

In this work, we employ an imaging Fourier transform spectrometer (IFTS) utilizing a focal plane array (FPA) as opposed to a single-element detector and scanning system, and demonstrate the potential to extract spatially-varying plume temperature and concentration of plume constituents from MWIR hyperspectral imagery. IFTS opens up some key advantages over standard non-imaging and scanning FTS. For example, each pixel has a small instantaneous field-of-view (IFOV), such that the range of temperatures sampled perpendicular to the line-of-sight is minimized. Additionally, due to the simultaneous spatial imagery obtained, variations in temperature and effluent concentration throughout the plume could now be inferred from the spatially-resolved spectra. Furthermore, by using the plume symmetry dictated by imagery, it may be possible to recover the temperature and concentration gradients along the line-of-sight.

We have demonstrated that temporal-averaging of hyperspectral imagery of turbulent scenes, such as those associated with jet engine exhaust, can remove much of the turbulent noise inherent in the data, and that the resulting spectra, after temporal averaging, approximates that of a steady-state plume. [58] Based on this analysis, the 1 cm^{-1} MWIR hyperspectral data of diesel-fueled jet engine exhaust was temporally averaged. This chapter demonstrates the ability to significantly reduce the dimensionality of the data by clustering pixels based on spectral similarity, shows the high-fidelity with which the clustered spectral data can be fitted, in a least-squares sense, to a single-temperature radiative transfer plume model, and displays the resulting spatially-varying temperature and plume constituent column density profiles,

with discussion as to steps that can be taken to further refine this research.

5.2 Experiment

Jet engine exhaust from a Turbine Technologies, Inc. SR-30 turbojet engine was observed from a side-plume vantage point with the FIRST-MWE positioned 11.2 meters from the engine, as shown in Figure 15 during combustion of low-sulfur diesel fuel at a fuel flow rate of 300 $\frac{cm^3}{min}$. The SR-30 turbojet engine uses a single stage axial flow turbine and single stage centrifugal (with radial outflow) compressor with an engine compression ratio of 3.4 and maximum rotation rate of 87,000 RPM. The engine diameter is 17 cm, with an engine length of 27 cm, and reported maximum exhaust gas temperature of 993 K and mass flow rate of 0.5 $\frac{kg}{s}$.

Figure 15. Experimental setup for collecting exhaust data from a turbojet engine (a) with the Telops FIRST-MWE (b). The turbojet engine was filled with diesel fuel and run at a fuel flow rate of 300 $\frac{cm^3}{min}$.

The Telops FIRST-MWE forms a hyperspectral datacube by collecting an intensity image on its InSb FPA (1800-6667 cm^{-1}) as the moving mirror of the in-

ternal Michelson interferometer scans from zero path difference (ZPD) through the user-defined maximum optical path difference (MOPD). The instrument employed an MOPD of 0.6 cm, corresponding to a spectral resolution of $\frac{0.6}{MOPD} = 1$ cm^{-1}, and a 200x64 pixel region of the 320x256 pixel Stirling-cooled InSb FPA, which corresponds to a 78.4 cm x 25.1 cm region in object space, centered on the engine exhaust. An integration time of 50 μs was used and an aperture stop was fitted to the instrument, as depicted in Figure 16, to avoid saturation.
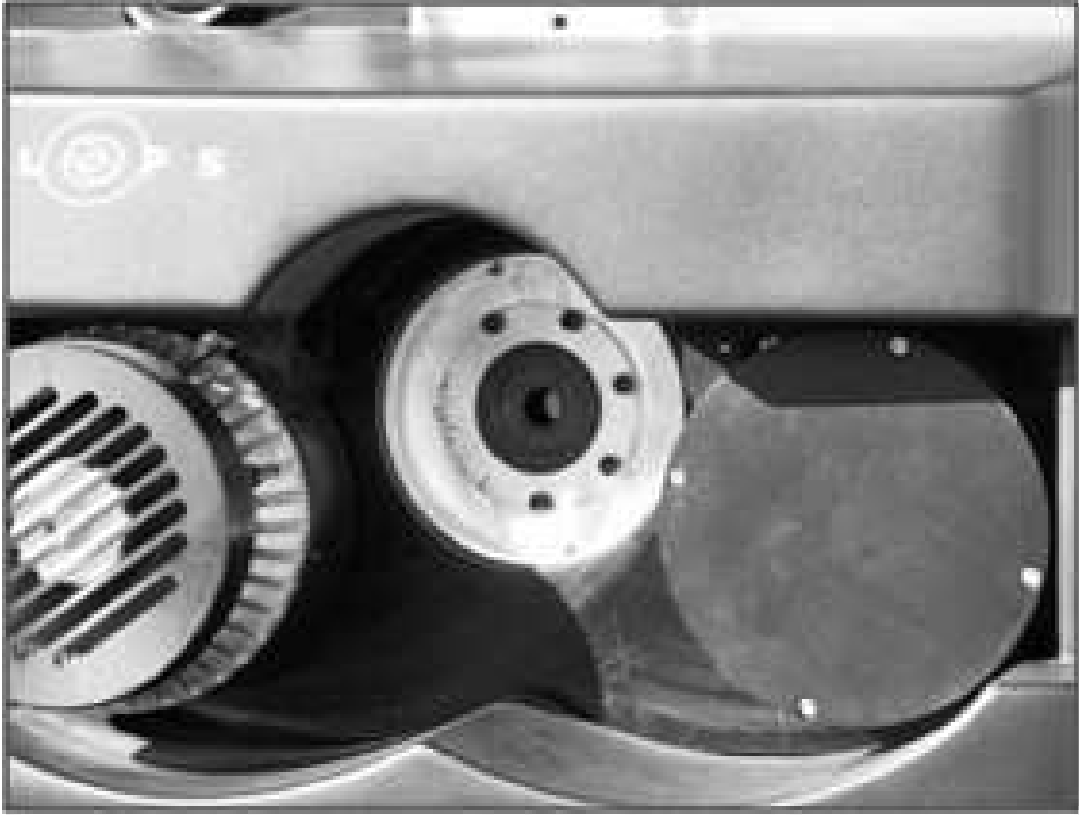
Figure 16. Variable-aperture stop fitted to Telops FIRST-MWE during data collection to avoid saturation. The aperture was adjusted prior to data collection, and was set as shown during collection of both plume and calibration data.

A large (66x66x122 cm^3) water-chilled ambient temperature corner-cube blackbody was placed immediately behind the engine exhaust and overfilling the instrument FOV, as shown in Figure 15, to ensure a constant background scene. Additionally, a rake of six k-type thermocouples was introduced into the plume, as shown in Figure

17, to make *in situ* temperature measurements. Three thermocouples were placed 21 cm downplume of the engine exit plane, while the remaining three were placed 42 cm downplume. The tip of individual thermocouples within a row were separated by 2 cm. The thermocouple row 42 cm downplume was offset to the left of the near-exit row by 1 cm, such that the left and middle thermocouples were each approximately 1 cm left and right of engine centerline, respectively. This alignment offset is depicted in Figure 18, which shows the near-exit row of thermocouples in-focus and the downplume row out-of-focus.

Figure 17. Rake of six k-type thermocouples to make *in situ* temperature measurements of the jet engine exhaust plume, viewed at an angle to portray locations of individual thermocouples with respect to the engine.

For dynamic scenes, such as those associated with turbulent exhaust from a jet engine, some of the variation in interferogram intensity with OPD is associated with variations in source intensity, as opposed to interference modulation due to the Michel-
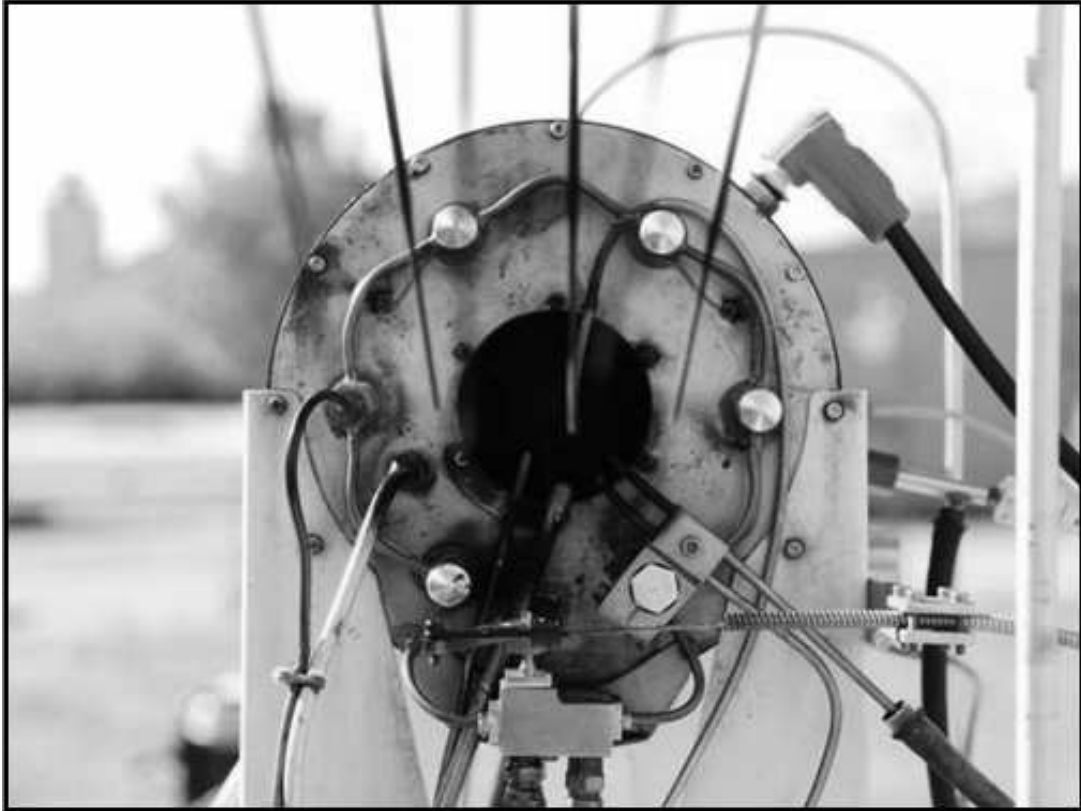
Figure 18. Rake of six k-type thermocouples to make *in situ* temperature measurements of the jet engine exhaust plume. The out-of-focus row of thermocouples located approximately 42 cm downplume is offset by approximately 1.5 cm left of centerline, while the row of thermocouples located 25 cm downplume (in-focus) are centered on the engine.

son interferometer. Previous work has demonstrated that SCAs appear in the interferogram as zero-mean noise that can be greatly reduced by temporal averaging of several interferograms [58]. A total of 150 hyperspectral datacubes were collected, and each interferogram within the 200x64 pixel time-averaged datacube was converted to a spectrum by applying a Fourier transform.

A two-temperature calibration process was applied to the uncalibrated temporally-averaged datacubes, which consisted of collecting 40 datacubes with each of two internal instrument blackbodies. The internal blackbodies were set to temperatures of 90^oC and 20^oC, and when in place, filled the entire FOV of the instrument. The instrument settings during collection of blackbody calibration data were identical to those used during collection of engine exhaust plume data. Calibration is generally used to determine and compensate for the response of the InSb detector (gain) and self-emission inside the instrument (offset). Self-emission within the instrument during the three hours of data collection varied greatly, leading to an unusable offset term. To compute a detector gain curve, a least-squares smoothing spline gain curve was computed from the spectral gain function that consisted of high frequency absorption features. An improved calibration process is currently being developed that addresses the issue of instrument self-emission variability. Since the goal of calibration is to address the broad spectral response of the detector to photons, a very degraded (32 cm^{-1}) spectral resolution will be used, allowing for collection of a large number of datacubes in a relatively short period of time. During the shorter collection time, variability of instrument self-emission should be minimized, and the offset term can be used to perform absolute data calibration.

5.3   Results and Discussion

Uncalibrated spectra from several spatially-averaged plume regions of the image scene were background-subtracted, with the background spectra obtained from a non-plume region of the image scene, to remove instrument self-emission and stray radiance. These spectra are overlayed in Figure 19, and demonstrate the highly pronounced red and blue spikes associated with CO_2 emission between 2180-2400 cm^{-1}. Also visible are water emission lines between 1800-2000 cm^{-1} and the P-branch of CO between 2000-2200 cm^{-1}. The R-branch of CO is highly obscured by the rising CO_2 red spike beginning at 2180 cm^{-1}.
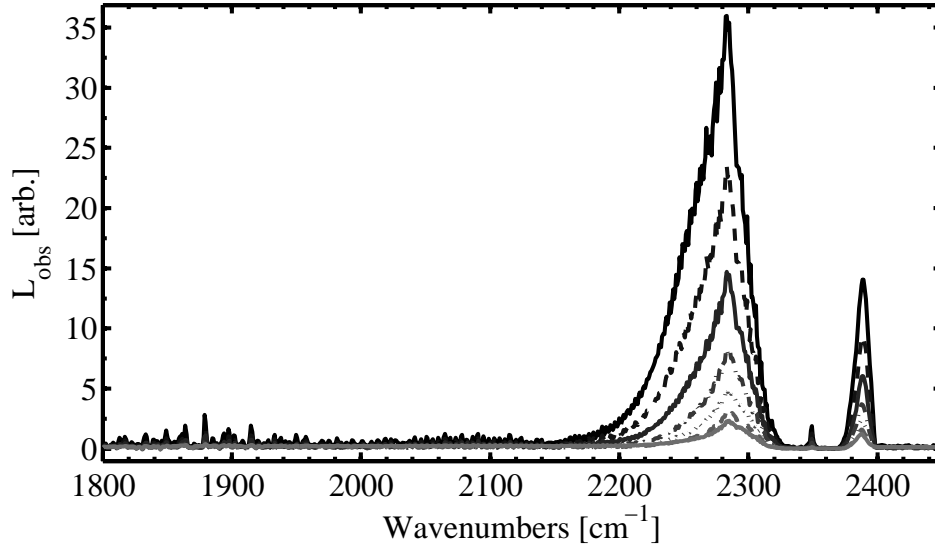
Figure 19. Uncalibrated spectra associated with spatially-averaged plume regions of the image scene following background-subtraction to remove instrument self-emission.

By peak-normalizing the uncalibrated data, spectral broadening of the CO_2 red spike was observed for pixels closest to the engine exit plane, as shown in Figure 20. Pixels in Figure 20 are separated by 3.9 cm, with pixel (170,31) at centerline approximately 3.9 cm downplume from the engine exit plane, and pixel (120,31) at centerline 23.4 cm downplume. Increased spectral broadening for pixels closer to

the engine exit plane are associated with increased population of higher level ro-vibrational states of CO_2, due to increased plume temperature.
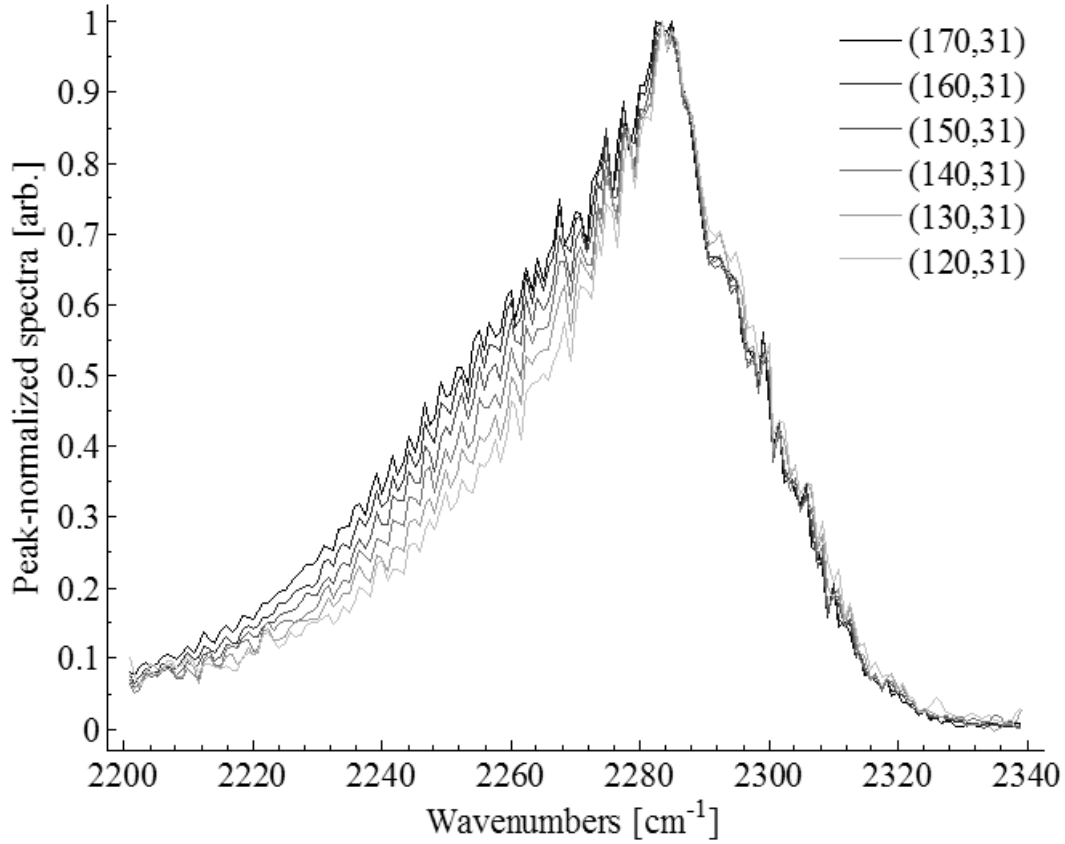
Figure 20. Close-up of peak-normalized CO_2 red spike for individual pixels along engine centerline, each separated by 3.9 cm. Spectral broadening of the red spike for pixels closer to the engine exit plane is due to increased temperature.

To reduce the dimensionality of the data, K-means clustering was implemented, using information gained from spectral analysis of the uncalibrated data. The goal of clustering is to group pixels into clusters such that the in-cluster variance among datapoints is small compared to out-of-cluster variance [18]. K-means clustering begins with the user defining the number of partitions (K) into which the data will be clustered. The clustering algorithm selects K pixels at random, each a centroid for one of the partitions. The remaining pixels are then assigned to the partition whose centroid is most similar to itself. With all pixels assigned to one of the K partitions,

center-of-mass for each partition is computed, and a corresponding centroid pixel is identified for each partition. As in the first iteration, all non-centroid pixels are again free to be assigned to the partition whose centroid is most similar to itself. This process of centroid determination and pixel reassignment continues, until centroid locations do not change between iterations [61].

Since it would be prohibitive to perform K-means clustering on the entire hyperspectral datacube, twelve spectral regions were selected from spectral lines associated with individual plume constituents, as detailed in Table 1. Spectral features from all plume constituents were identified and incorporated into the K-means clustering routine.

These twelve spectral features from every pixel's spectra were provided as input to the standard MATLAB K-means function using a cosine distance measurement, in search of a pragmatic choice of K=20 clusters. Average spectra and standard deviation of each region was computed, and the clusters were sorted based on integrated spectral radiance of the CO_2 blue spike (2380-2420 cm^{-1}). Brightness temperature was computed at the peak of the CO_2 red spike (2283 cm^{-1}) for each of the plume clusters, and the resulting brightness temperature map is shown in Figure 21.

Of the twenty clusters, nine distinct plume regions were uncovered. The remain-
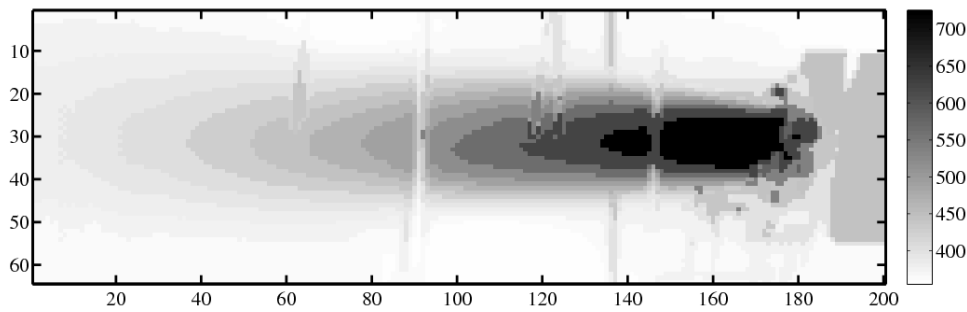
Figure 21. Brightness temperature map of clustered engine data. Temperatures shown are in K. Pixel numbers for the source scene are marked on the left and bottom axes, with individual pixel dimensions of 3.9 cm x 3.9 cm.

Table 1. Spectral features used as inputs to the K-means clustering algorithm from spectral lines associated with identified exhaust plume constituents.

Spectral region (cm^{-1})	Corresponding plume constituent
1860-1866	H_2O
1877-1881	H_2O
2040-2060	CO
2060-2080	CO
2080-2100	CO
2150-2200	CO_2
2200-2250	CO_2
2250-2275	CO_2
2275-2300	CO_2
2300-2335	CO_2
2370-2385	CO_2
2385-2395	CO_2

ing clusters consisted of background, jet engine parts, and various components of the thermocouple rake system, including metal stands and the thermocouples, which protrude into the plume near columns 60 and 120 in Figure 21. A representative calibrated spectra from the hottest plume region, shown with a brightness temperature of 720 K in Figure 21, is provided in the top subplot of Figure 22, accompanied in the bottom subplot by a line-by-line radiative transfer model (LBLRTM) transmittance profile for an 11.2 m path through atmosphere defined by the following measured meteorological conditions: P = 1 atm, T = 300 K, RH = 35%.

A single-temperature plume model was developed to estimate plume temperature and concentrations of H_2O, CO, and CO_2. The modeled radiance, $L_{mdl}(\nu)$, is described by the product of the plume spectral emissivity, $\varepsilon(\nu, T_p)$, modified by atmosphere transmittance, $\tau_{atm}(\nu, T_{atm})$, and a Planckian function: $L_{BB}(\nu, T_p) = \frac{2hc^2\nu^3}{\exp(\frac{hc\nu}{k_B T_p})-1}$, where T_p is the plume temperature, T_{atm} is the atmosphere temperature, h is Planck's constant, k_B is Boltzmann's constant, and c is the speed of light in vacuum:
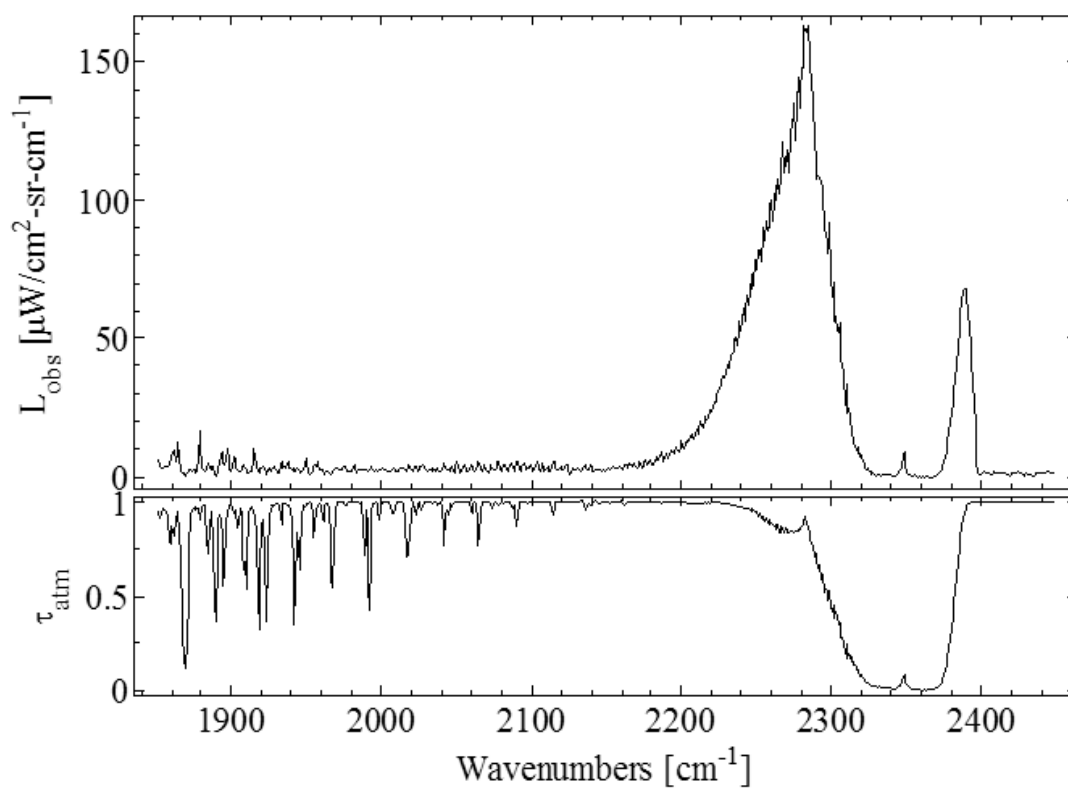
Figure 22. Jet engine plume spectra. Top: Representative plume spectra from a pixel in the hot plume region in close proximity to the engine exit plane - pixel (170,31) in Figure 21. Bottom: LBLRTM transmittance profile for 11.2 m path through atmosphere.

$$L_{mdl}(\nu, T_p) = \varepsilon(\nu, T_p)L_{BB}(\nu, T_p)\tau_{atm}(\nu, T_{atm}) \tag{24}$$

The model incorporates a few simplifying assumptions. First, since the source is very hot, and a constant ambient-temperature blackbody background source was introduced into the scene, both background and stray radiance are assumed to be negligible. Second, all molecules within a given plume region are assumed to be at a single temperature, T_p. Third, the atmosphere between plume and sensor is assumed to be at constant temperature, T_{atm}, for the 11.2 m pathlength. The constant atmosphere assumption allows for the atmosphere transmittance function (τ_{atm}), shown in the bottom subplot of Figure 22, to be included in the plume model for all plume regions. Plume spectral emissivity, $\varepsilon(\nu, T_p)$, for each gas was computed based on Beer's Law: $\varepsilon(\nu, T_p) = 1 - e^{-\sum_i q_i l \sigma_i(\nu, T_p)}$, where q_i is column density of molecule i and l is plume pathlength, using a line-by-line radiative transfer model (LBLRTM) to compute absorption cross-sections, $\sigma_i(\nu, T_p)$, using the high temperature spectroscopic (HITEMP) database for H_2O and the carbon dioxide spectroscopic databank (CDSD) for CO_2. In all cases, the Boltzmann distribution is factored into σ_i.

A nonlinear least squares fitting routine was implemented to produce a best fit of the average spectrum from each plume region to the plume model. Fit parameters consisted of plume temperature, T_p, and column densities for each of the plume constituents ($q_i l$).

Figure 23 shows the capability of fitting the engine exhaust data to a simplified plume model, with fit parameters associated with plume temperature and column densities of H_2O, CO, and CO_2. The plot of residuals (L_{obs} - L_{mdl}) in the bottom subplot of Figure 23 show that the model is in good agreement with the data, with an overall error of 6.39%. The largest residual values are located between 2200-2400 cm^{-1}, and are associated with difficulty in fitting the CO_2 red- and blue-spikes of a

61

combustion plume with large thermal gradient in the direction of instrument line-of-sight to a single-temperature plume model. The fitted temperature in this region was 978 ± 2 K, with H_2O, CO, and CO_2 column densities of 0.138 ± 0.005 cm^{-2}, 0.0038 ± 0.0002 cm^{-2}, and 0.0980 ± 0.0009 cm^{-2}, respectively. It is reasonable to assume temperature and concentration gradients exist in the mixing layer between the hot plume and ambient atmosphere, and a more sophisticated, multiple-layer model is needed to accurately describe the spectrum.
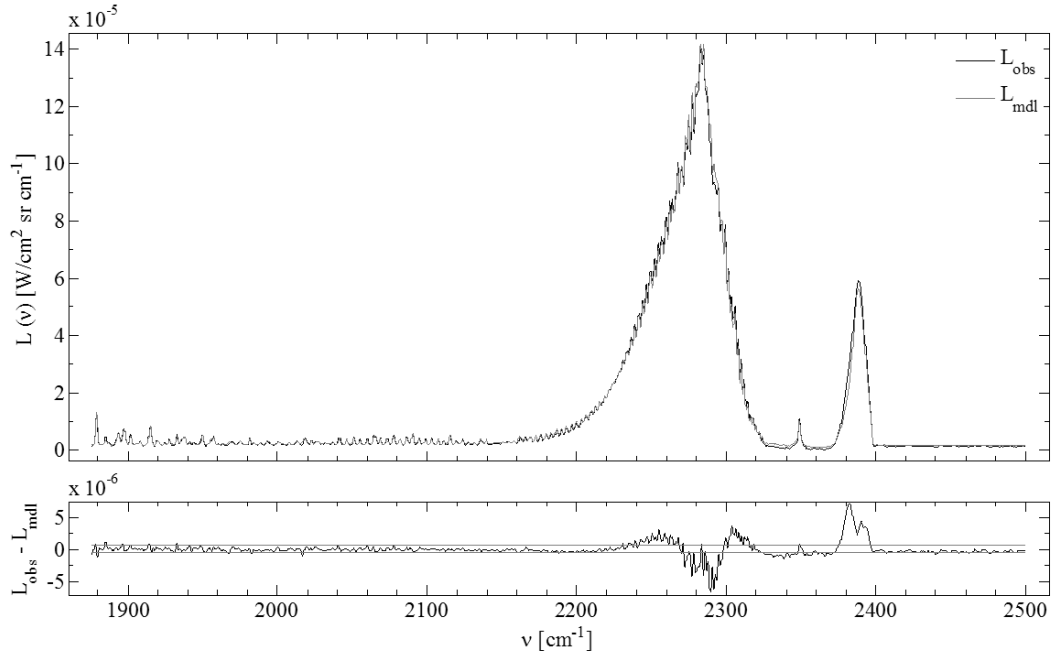
Figure 23. Spectral fit of jet engine plume data. Top: Plot of data and model for the plume region closest to the engine exit plane. Bottom: Plot of residuals (L_{obs} - L_{mdl}).

Figures 24 and 25 show calculated temperatures obtained using the plume model described previously for each of the plume regions identified by clustering, as a function of plume diameter and plume length, respectively. Static temperatures obtained from thermocouple measurements near plume centerline for each row of the thermocouple rake are shown in each plot, with Thermocouple 1 corresponding to the center thermocouple in the row of thermocouples 21 cm downplume from the engine exit plane, and Thermocouple 2 corresponding to the right thermocouple (closest to cen-

terline) in the row located 42 cm downplume. *In situ* measurements of 719 K and 522 K were obtained from thermocouple static temperatures, compared to model-derived values of 811 ± 1.5 K and 543 ± 1.6 K, respectively.
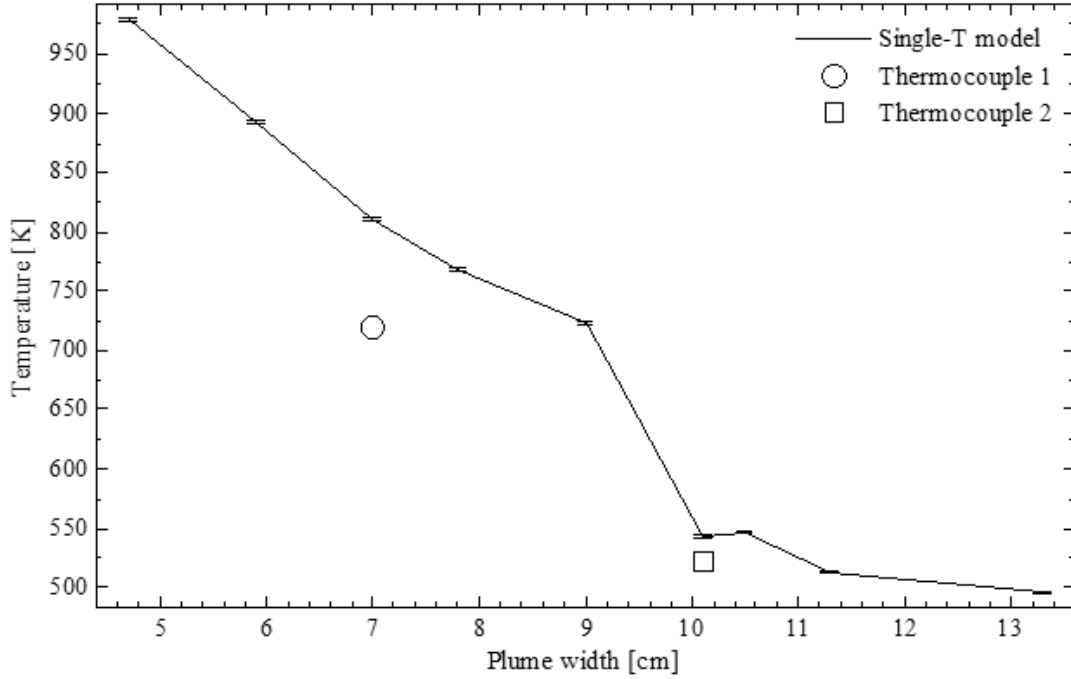
Figure 24. Spatial profile of plume temperature as a function of plume width.

Thermocouple temperature measurements were obtained for all six thermocouples in the rake for the duration of the data collection, as shown in Figures 26 and 27 for the row of thermocouples 21 cm and 42 cm downplume from the engine exit plane, respectively. The temperature spikes in both plots near t=170 s for all six thermocouples corresponds to initial engine flare-up, followed by settling and a gradual ramp-up to steady-state near t=210 s. Even in steady-state, temperature fluctuations were evident in the temporal plots depicted for all six thermocouples. Plume temperatures 2 cm left of centerline at 21 cm downplume are on the order of 200 K cooler than those measured by the centerline thermocouple, while temperatures measured 2 cm left of the middle thermocouple at 41 cm downplume are approximately 75 K cooler
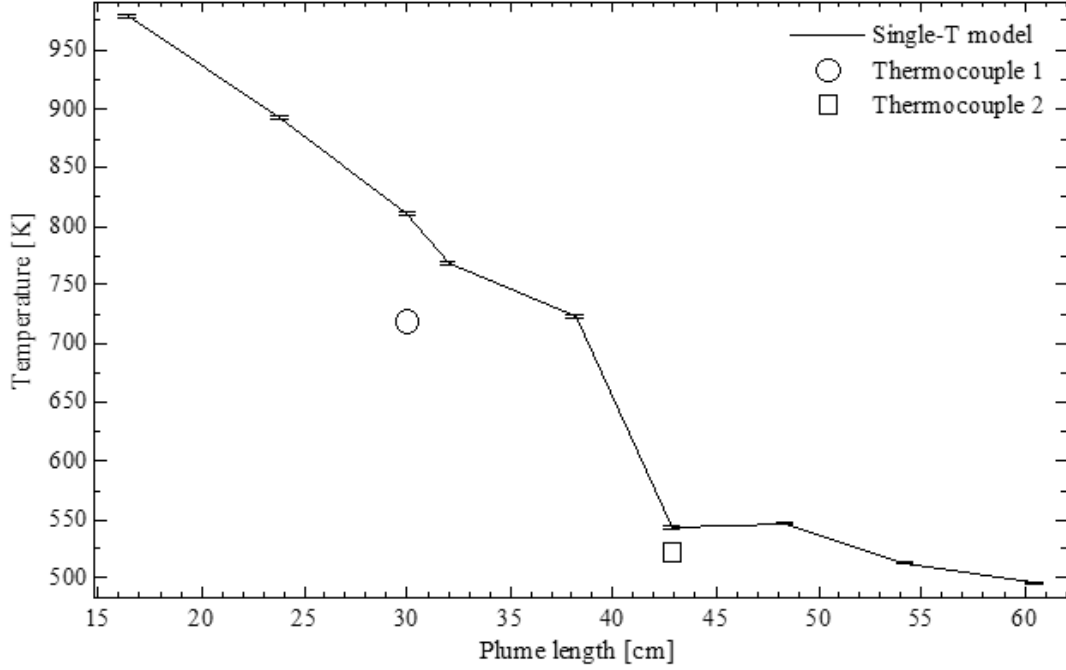
Figure 25. Spatial profile of plume temperature as a function of plume length.

than at the center thermocouple location. These measurements give clear indication of the steep temperature gradient in the direction of instrument line-of-sight.

Temperatures obtained by fitting data to the single-temperature plume model for the plume region 21 cm downplume and 42 cm downplume differed from thermocouple measurements near the same locations by 92 K and 21 K, respectively. This difference is possibly due to a combination of factors. First, the plume model assumes a single temperature, while it is known from the thermocouple data that a plume temperature gradient exists across the plume in the direction of instrument line-of-sight. Second, thermocouple placement within the plume was not precise, and individual thermocouples within the array were not perfectly aligned. Consequently, thermocouples may be located in plume regions slightly cooler than those observed radiometrically by the instrument.

Spatial profiles of column densities of CO, CO_2, and H_2O in terms of volume mixing ratio per unit area (cm^{-2}), and concentration of atmospheric CO_2 (ppmV) are

64
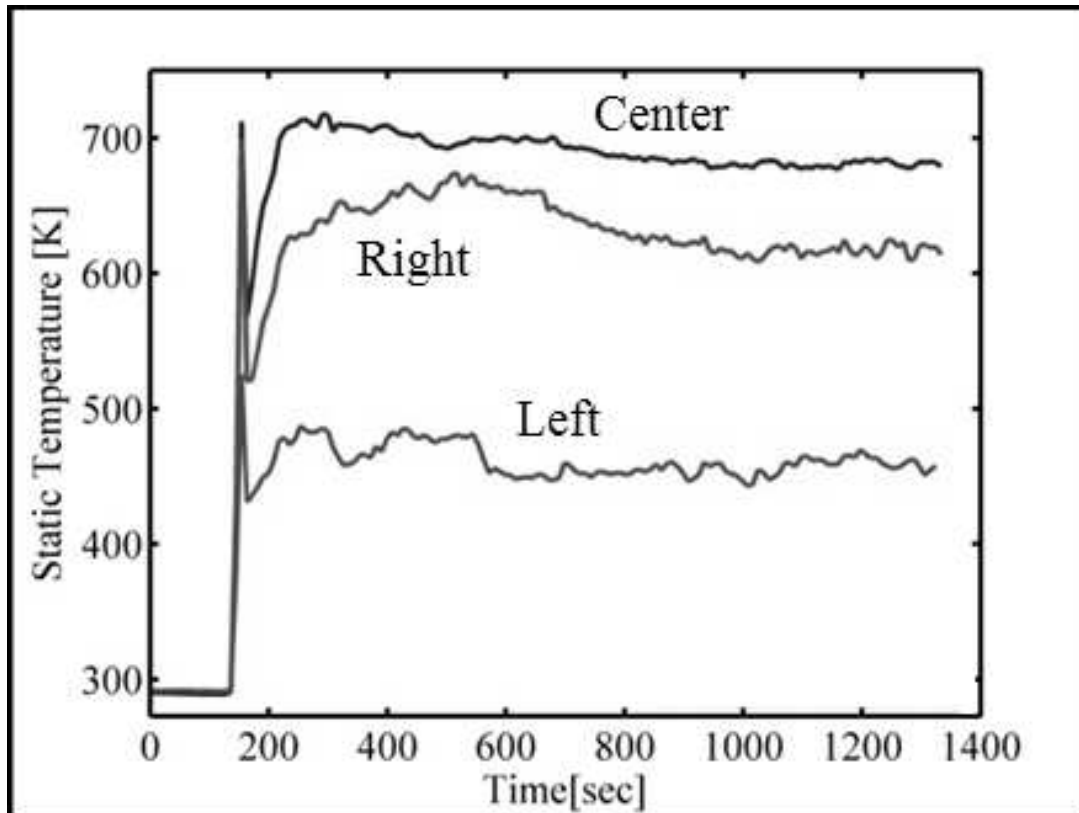
Figure 26. Temporal plot of plume temperatures obtained from thermocouple measurements for the near-plume row of thermocouples at 21 cm downplume from engine exit plane.
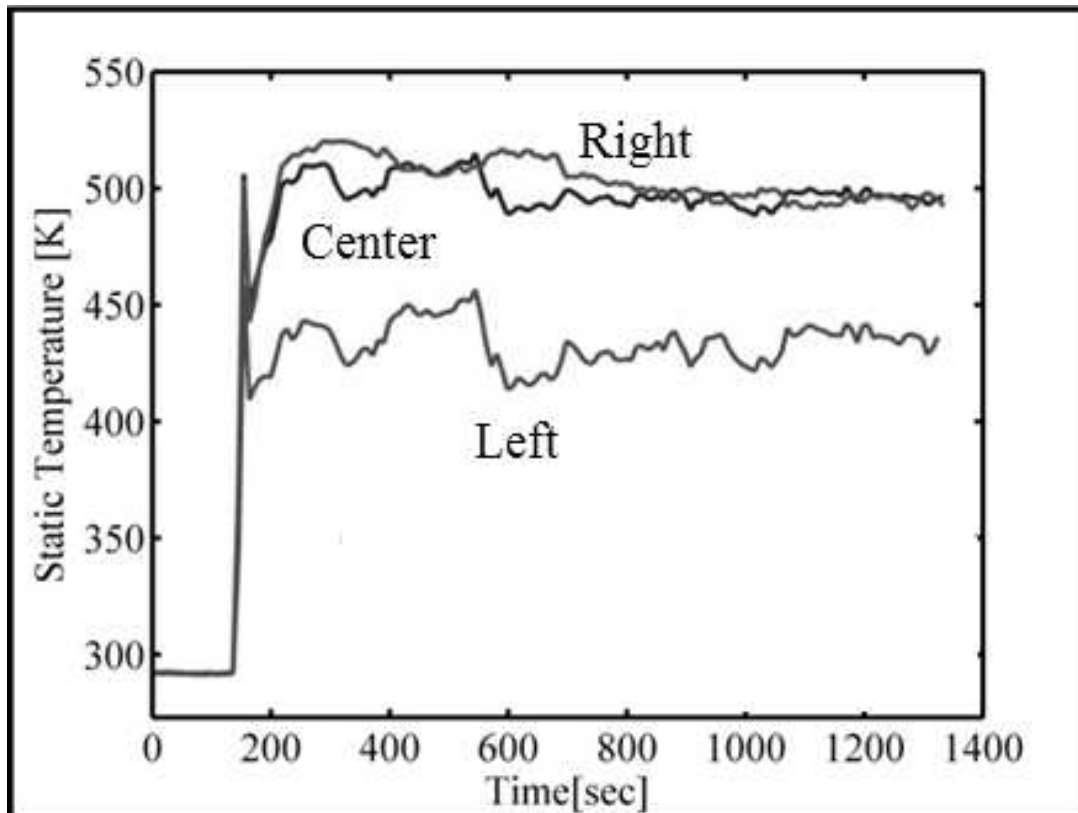
Figure 27. Temporal plot of plume temperatures obtained from thermocouple measurements for the far-plume row of thermocouples at 42 cm downplume from engine exit plane.

shown in Figure 28 as a function of plume length. Through the first five plume regions, up to 38 cm downplume of the engine exit plane, column density values steadily decrease, followed by a sudden increase in column densities for each of the plume constituents and concentration of atmospheric CO_2 at just over 40 cm downplume. Although the exact reason for this sudden increase is unknown, it is possibly due to entrainment of the exhaust gases by the background blackbody corner cube.
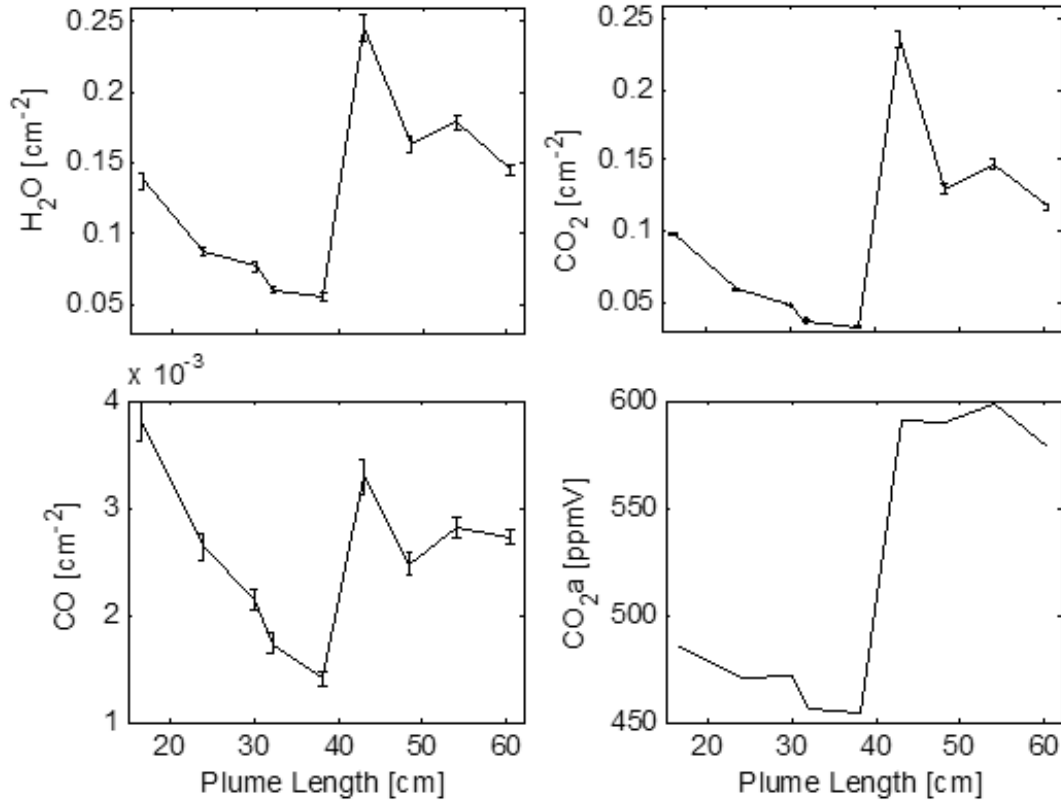
Figure 28. Spatial profile column densities of plume constituents and atmospheric CO_2 as a function of plume length.

A combination of temporal averaging and clustering of pixels based on spectral similarity significantly reduced the data from 150 datacubes, each containing 12,800 individual pixel spectra to 9 plume cluster spectra from the temporally-averaged datacube. The 9 plume cluster spectra were fitted to a single-temperature radiative transfer plume model with temperature variation of 92 K and 21 K at thermocouple

locations, and with low overall residual error (6.39%). Spectrally significant residuals were associated with fitting a single-temperature model to spectra of a plume with a large thermal gradient in the direction of instrument line-of-sight. Temperature was measured *in situ* with a rake of 6 k-type thermocouples and were compared to those observed radiometrically. Temperature gradients were observed both downplume and across plume, moving away from engine centerline. The sharp rise in column densities of plume constituents and atmospheric CO_2 at 40 cm downplume is likely attributable to entrainment of plume gases at the far wall of the corner cube blackbody, but the exact cause is not yet understood completely.

Although the single-temperature model was able to fit the data with small residual error, the spectra poses some significant challenges that should be addressed in future work. First, the dominant spectral features throughout the plume data are the CO_2 red and blue spikes. This region poses the greatest challenge in fitting to a single-temperature plume model. Spectral lines associated with CO and H_2O are much weaker, and in some cases, barely rise above the noise level. With only 1 cm^{-1} spectral resolution, the CO and H_2O lines do not lend themselves to more thorough analysis, whereas collecting spectral data at better resolution, would result in a reduced SNR, longer data collection time. Future data collection at improved (0.25 cm^{-1}) spectral resolution may be useful, but more datacubes must be collected and temporally averaged to reduce the noise level and a smaller window size should be used to reduce the data collection time. However, the most significant problem left to be solved is developing a multi-layer plume model that, in theory, will lead to extraction of more reliable plume information. Implementation of this higher-order model will come at a cost in analysis time, and will result in added complexity, but the overall potential benefits make it a worthwhile pursuit.

VI. Remote Detection and Quantification of Industrial Smokestack Effluents by MWIR IFTS

6.1 Introduction

It is often desirable to monitor industrial smokestack effluents remotely, and both active and passive remote detection techniques have been developed. Active techniques include differential absorption lidar (DIAL) [19; 82] and tunable diode laser spectroscopy (TDLS) [74]. Solar light has been used as a source for absorption techniques, such as differential optical absorption spectroscopy (DOAS) [20; 62] and correlation spectroscopy (COSPEC) [57; 81].

Plume monitoring via infrared emission spectroscopy uses the plume itself as the source, and can be performed without the presence of solar radiation or illumination by a laser. Passive techniques are advantageous for several applications. First, it is the only method to simultaneously collect spectra of multiple chemical species, since illumination by a laser source must be tuned to an individual chemical. Second, active plume interrogation to obtain spectrally resolved information requires spatial scanning of the laser spot. Finally, interrogation of a plume with a laser may not be desirable for covert plume detection operations. The most common passive technique is Fourier transform spectrometry [35; 11; 64; 16]. In recent years, imaging techniques have demonstrated potential for remote monitoring of industrial smokestack effluents. Among these techniques are ultraviolet (UV) imaging with a UV digital camera to monitor sulfur dioxide (SO_2) emissions [8], multispectral thermal imaging with a filter wheel [80; 2], imaging spectroradiometry using tunable filters [76; 53], and scanning imaging Fourier transform spectrometry [13; 7; 59; 28].

An imaging Fourier transform spectrometer (IFTS) utilizing a focal plane array (FPA) as opposed to a single-element detector and scanning system has proven itself

useful for detection and analysis of chemical plumes in the longwave infrared (LWIR) [43]. Spectra of coal-burning smokestack plumes can be challenging to quantitatively interpret for several reasons: (1) structured emission from several different species overlap in the spectrum; (2) the plume is not necessarily optically thin; (3) temperature and effluent concentrations vary spatially across the plume and along the line-of-sight; (4) spatial averaging over a sizable portion of the plume entails averaging over different rotational-vibrational distributions; (5) exhaust flow is turbulent in the plume. IFTS has the potential to remove difficulties associated with the last three items. With each pixel having a small instantaneous field-of-view (IFOV), the range of temperatures sampled perpendicular to the line-of-sight is minimized. Variations in temperature and effluent concentration throughout the plume could now be inferred from the spatially-resolved spectra. It has also been demonstrated that background spectra can be collected simultaneously, and it may be possible to perform atmosphere correction of spectral data by using information obtained from the broadband stack emission. Furthermore, by assuming axial symmetry and using the spatially-resolved spectra, it may be possible to recover the temperature and concentration gradients along the line-of-sight. This chapter presents the first MWIR hyperspectral imagery of an industrial smokestack plume collected with an IFTS consisting of a Michelson interferometer and an InSb (indium antimonide) FPA, and demonstrates dimensionality reduction of the data via K-means clustering based on spectral similarity of plume features. The resulting plume spectra are fit to a single-temperature radiometric transfer plume model, with fit parameters of temperature and concentration in the region of the plume nearest stack exit very close to those obtained by *in situ* measurement techniques.

6.2 Experiment

6.2.1 Stack Measurements.

Plume emissions from a coal-burning industrial smokestack near Wright-Patterson Air Force Base, Ohio were observed with the Telops FIRST-MWE, at a location approximately 600 meters east-southeast of the stack source. The instrument location is depicted with a cross in the bottom-right corner of Figure 29 and the three industrial smokestacks, each of height 76.2 meters and diameter 4.2 meters, are represented by circles in the left half of Figure 29. Hyperspectral imagery of exhaust from the center stack was collected at night with a cold sky background. Cloud coverage, which blanketed the sky earlier in the evening, had diminished considerably by the time that data was collected, giving us a clear view of the cold sky background. During data collection, local temperature of 300 K, relative humidity of 40% and an average wind velocity of 0.9 m/s northeast were measured at the instrument location. The line-of-sight of the instrument is depicted by a dashed arrow proceeding from the instrument location and directed towards the center stack, which was operating at full capacity. It should be noted that the left stack was operating at half-capacity, forming a smaller plume that propagated towards the center stack, due to wind direction. A body of water runs along the east property line of the industrial facility. The compass in the top right corner of Figure 29 orients the reader geographically, so that wind velocity and instrument line-of-sight are correlated to the test setup during data collection.

6.2.2 Instrument.

The Telops FIRST-MWE forms a hyperspectral datacube by collecting an intensity image on its InSb FPA (1800-6667 cm^{-1}) as the moving mirror of the internal Michelson interferometer scans from zero path difference (ZPD) through the user-defined maximum optical path difference (MOPD). The instrument employed
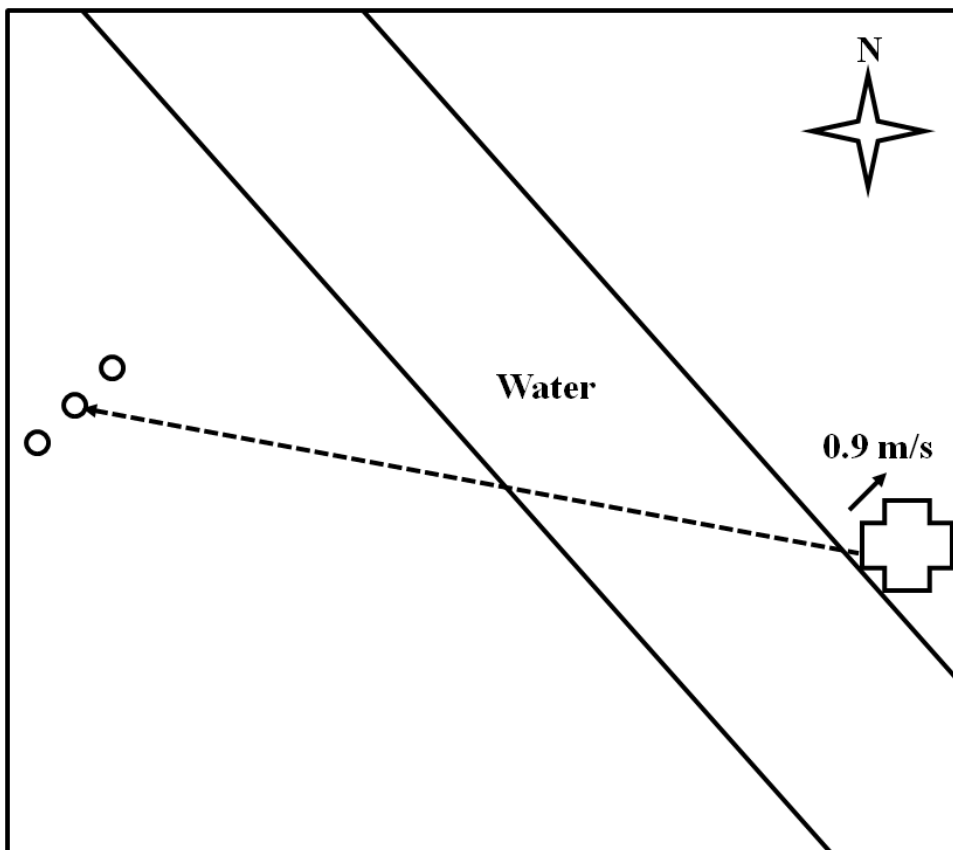
Figure 29. Experimental setup for collecting industrial smokestack effluent data.

an MOPD of 2.4 cm, corresponding to a spectral resolution of $\frac{0.6}{MOPD} = 0.25$ cm^{-1}, and a 128x64 pixel region of the 320x256 pixel Stirling-cooled InSb FPA, with an integration time of 100 μs per frame. Each pixel has an IFOV of 0.35 mrad, which corresponds to a 21 cm x 21 cm spatial dimension at the stack source. With these instrument settings, approximately four hyperspectral datacubes of assymetric interferograms (37,928 points on the long-side of the interferogram and 14,285 points on the short-side) were collected per minute for over 25 minutes. For dynamic scenes, such as those associated with turbulent plumes, some of the intensity variations in the interferogram is due to source fluctuations, as opposed to interference modulation due to the Michelson interferometer. Previous work has demonstrated that source fluctuations appear in the interferogram as a noise term that can be greatly reduced by temporal averaging of several interferograms [58]. A total of 100 datacubes were collected and temporally averaged, after which each interferogram within the 128x64 pixel time-averaged datacube was converted to spectra by applying a Fourier transform.

A two-temperature calibration process was applied to the uncalibrated temporally-averaged datacube, which consisted of collecting 300 datacubes with each of two internal instrument blackbodies. The internal blackbodies were set to temperatures of 90°C and 20°C, and when in place, filled the entire FOV of the instrument. The instrument settings during collection of blackbody calibration data were identical to those used during collection of stack plume data, with the exception of an integration time of 50 μs to avoid saturation. Calibration is generally used to determine and compensate for the response of the InSb detector (gain) and self-emission inside the instrument (offset). Self-emission within the instrument during the three hours of data collection varied greatly, leading to an unusable offset term. Additionally, spectral lines associated with atmospheric absorption features appeared in the resulting

73

calibration gain curve. To compute a detector gain curve, a least-squares smoothing spline gain curve was computed from the spectral gain function that consisted of high frequency absorption features. An improved calibration process is currently being developed that addresses the concerns of instrument self-emission variability. Since the goal of calibration is to address the broad spectral response of the detector to photons, a very degraded (32 cm^{-1}) spectral resolution will be used, allowing for collection of a large number of datacubes in a relatively short period of time. During the shorter collection time, variability of instrument self-emission should be minimized, and the offset term can be used to perform absolute data calibration.

6.3   Results and discussion

6.3.1   Spectral Assignment.

A background-subtracted emission spectrum of a temporally averaged plume pixel at stack centerline approximately 1 m downplume of the stack exit plane is provided in Figure 30. The intense features in the regions 2050-2130 cm^{-1} and 2200-2400 cm^{-1} arise from CO_2 emissions in the $\nu_1 + \nu_2^1 \rightarrow 0$, $\nu_1 + 2\nu_2^2 \rightarrow \nu_2^1$, $2\nu_1 \rightarrow \nu_2^1$, $\nu_2^1 + \nu_3 \rightarrow \nu_2^1$ (red spike), and $\nu_3 \rightarrow 0$ (blue spike) ro-vibrational transitions [83]. The red and blue spike are formed by strong attenuation of the emission spectra from 2280-2380 cm^{-1} due to absorption by atmospheric CO_2. The simple pattern of widely spaced lines at 2600-3000 cm^{-1} are easily assigned to HCl. The characteristic rotational structure of the $\nu_1 + \nu_3$ bending mode of SO_2 near 2500 cm^{-1} is also readily apparent [37]. The simple rotational structure of NO and CO is superimposed with the CO_2 emission at the longer wavelengths.

An atmosphere transmittance function, shown in the bottom subplot of Figure 30 was computed using a pathlength from source to sensor of 600 meters, with a constant air temperature of 300 K and 40% relative humidity. Spectral features
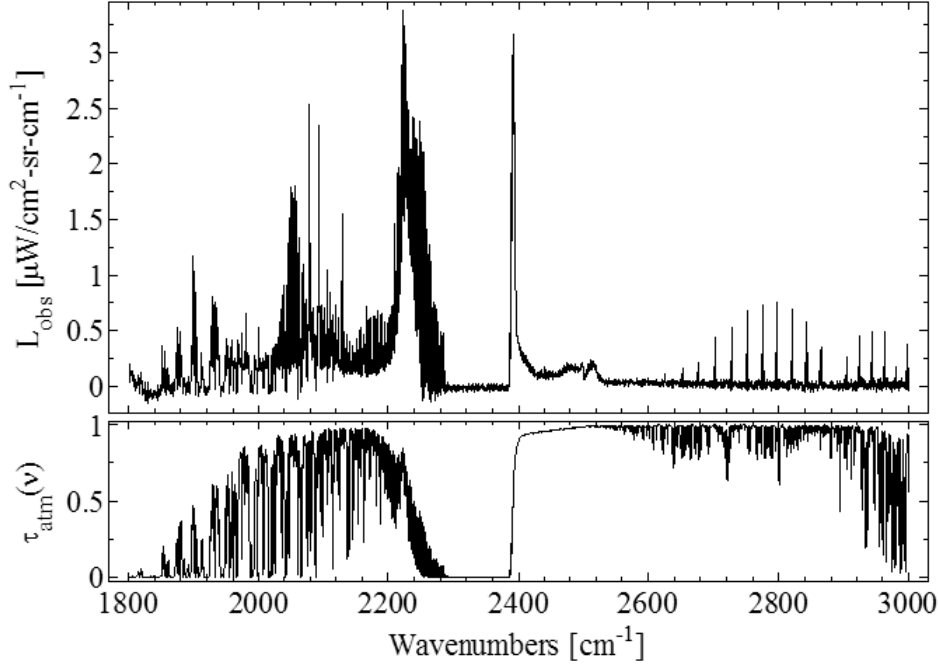
Figure 30. Industrial smokestack plume spectra. Top: Representative Background-subtracted plume spectra from a single hot pixel. Bottom: Atmosphere transmittance function for 600 m path from plume to sensor.

from peak-normalized atmosphere-attenuated molecular absorption cross-section basis functions, computed using the HITRAN (high-resolution transmission molecular absorption) database, were compared to the plume spectrum associated with the central plume region near the stack exit plane to aid in assignment of plume constituents. The top subplot of Figure 31 shows the observed spectral radiance of this plume region from 1890-2200 cm^{-1}, accompanied by plots of peak-normalized atmosphere-attenuated plume emissivities of H_2O, NO, CO_2, and CO. The bottom subplot of Figure 31 shows the observed spectral radiance of the same plume region from 2430-2930 cm^{-1}, accompanied by plots of peak-normalized atmosphere-attenuated plume emissivities of CO_2, SO_2, and HCl. Residuals associated with fitting the observed spectral radiance from this plume region to a single-temperature plume model are also shown for both spectral bands immediately beneath the spectral radiance plots.

It should be noted that the spectral resolution of the data and model were degraded to 0.4 cm^{-1} to allow for improved signal-to-noise without losing the ability to resolve narrowly-defined spectral features of plume constituents. The method used to fit the data to a plume model will be discussed following a detailed discussion of some of the notable spectral features of observed plume constituents.

For example, three Q-branches of CO_2 are observed in the top subplot of Figure 31 between 2070-2150 cm^{-1}, identified as the $\nu_1 + \nu_2^1 \rightarrow 0$, $\nu_1 + 2\nu_2^2 \rightarrow \nu_2^1$, and the $2\nu_1 \rightarrow \nu_2^1$ ro-vibrational transitions, proceeding from left to right, with the P-branch of the $\nu_1 + \nu_2^1 \rightarrow 0$ transition observed between 2020-2070 cm^{-1}. Spectral lines associated with the P-branch of CO are observed within the 2070-2150 cm^{-1}, and spectral lines associated with the R-branch of CO are identified between 2150-2200 cm^{-1}.

In the bottom subplot of Figure 31, the $\nu_1 + \nu_3$ bending mode of SO_2 is evident within the spectral region 2460-2530 cm^{-1}. Within this region, there is very little atmosphere attenuation, and almost no overlap from other molecular species within the plume, allowing for the spectral signature to be easily identified.

The P and R branch structure of the HCl emission spectra shown to the right of the SO_2 spectra in the bottom subplot is readily assigned with the rotational line spacing of 2B = 21 cm^{-1} easily discerned. The spectral resolution is sufficient to discern both the $H^{35}Cl$ and $H^{37}Cl$ isotopes with an abundance ration of 2.5:1. Atmosphere attenuation in this spectral region is due predominately to absorption of atmospheric water. A small baseline slope is present in the data, which may be due to continuum emission from soot or an uncorrected instrument offset.

The spectra vary significantly along the propagation direction. For example, the spectral radiance begins to decrease rapidly for pixels further downplume. Additionally, some small variations in relative line-heights of HCl and widths of CO_2 spectral
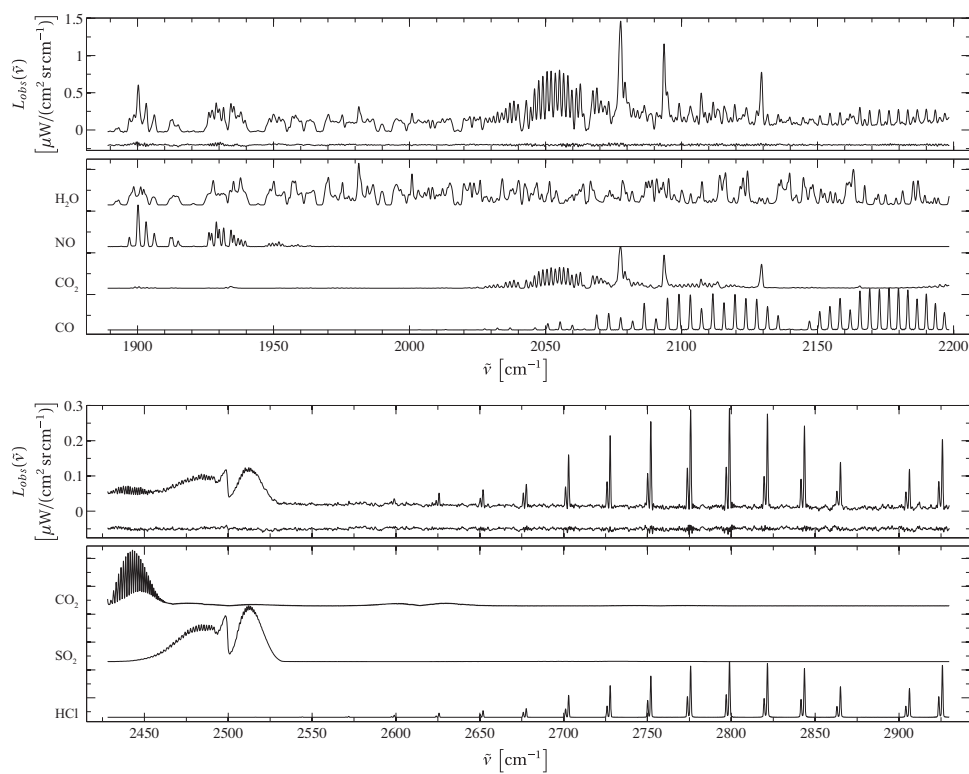
Figure 31. Spectral assignment of industrial smokestack plume constituents.

features is observed. Spectra associated with three distinct plume pixels are provided in Figure 32.

To develop spatial maps of the plume temperature and species concentrations, a two step process is employed. First, plume regions with similar spectra are identified using K-means clustering. Second, a simple radiative transfer model is fit to the average spectra for each plume region.

A single-temperature plume model was used to fit plume temperature and concentrations of spectrally-identified molecular plume constituents. The modeled radiance, $L_{mdl}(\nu)$, is described by the product of the plume spectral emissivity, $\varepsilon(\nu, T_p)$, modified by atmosphere transmittance, $\tau_{atm}(\nu, T_{atm})$, and a Planckian function: $L_{BB}(\nu, T_p) = \frac{2hc^2\nu^3}{\exp(\frac{hc\nu}{k_B T_p})-1}$, where T_p is the plume temperature, T_{atm} is the atmosphere temperature, h is Planck's constant, k_B is Boltzmann's constant, and c is the speed of light in vacuum:

$$L_{mdl}(\nu, T_p) = \varepsilon(\nu, T_p)L_{BB}(\nu, T_p)\tau_{atm}(\nu, T_{atm}) \tag{25}$$

The model incorporates a few simplifying assumptions. First, since data was collected at night with a cold sky background, both background and stray radiance are assumed to be negligible. Second, all molecules within a given plume region are assumed to be at a single temperature, T_p. Third, the atmosphere between plume and sensor is assumed to be at constant temperature, T_{atm}, for the 600 meter pathlength. The constant atmosphere assumption allows for the atmosphere transmittance function (τ_{atm}), calculated previously for spectral assignment, to be included in the plume model for all plume regions. Plume spectral emissivity, $\varepsilon(\nu, T_p)$, for each gas was computed based on Beer's Law: $\varepsilon(\nu, T_p) = 1 - e^{-\sum_i q_i l \sigma_i(\nu, T_p)}$ using the line-by-line radiative transfer model (LBLRTM) applied to molecular absorption features, $\sigma(\nu, T_p)$, from the HITRAN database, where $q_i l$ (product of concentration and pathlength) is the
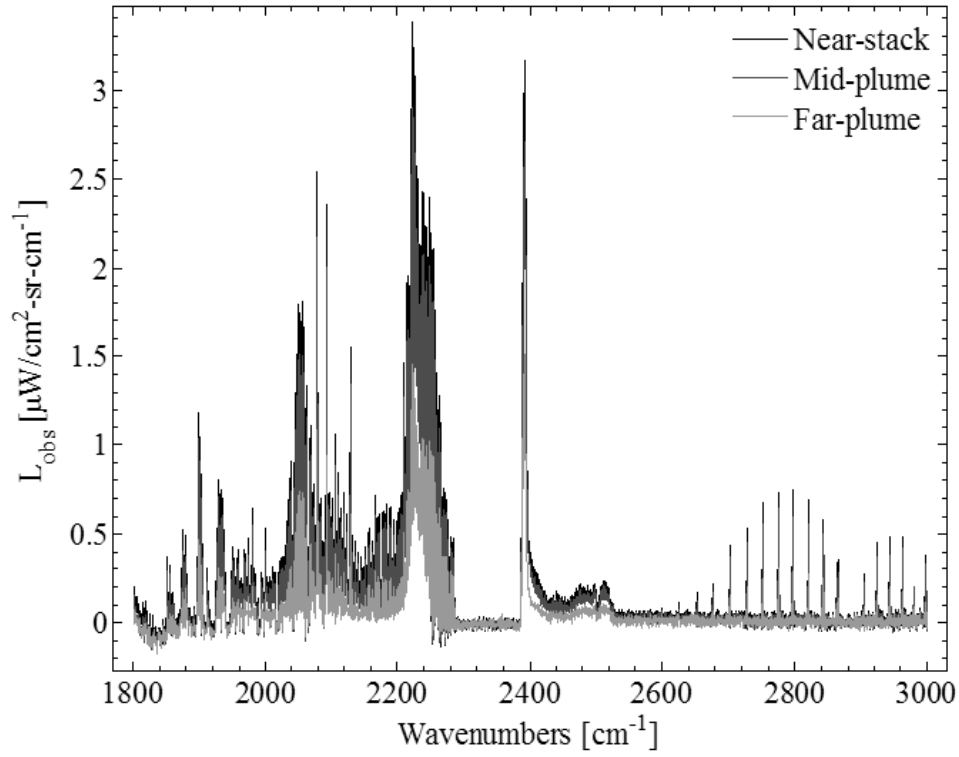
Figure 32. Spectra associated with three distinct plume pixels, after performing background subtraction. The near-plume spectrum is of a pixel within the hottest core region of the plume, while mid- and far-plume spectra are associated with pixels in the mid- and outer-plume regions, respectively.

column density of the ith molecule

Twelve spectral features were selected from spectral lines associated with individual plume constituents, as detailed in Table 2. These twelve spectral features from every pixel's spectra were provided as input to the standard MATLAB K-means function using a cosine distance measurement, in search of a pragmatic choice of K=25 clusters. Average spectra and standard deviation of each region were computed, and the clusters were sorted based on integrated spectral radiance of the CO_2 blue spike (2380-2420 cm^{-1}). Of the resulting twenty-five clusters, eighteen were plume clusters, with the remaining clusters consisting of stack, background, or a combination of stack and plume. The plume clusters are depicted in Figure 33 in terms of fitted temperatures using spectral features to the left of the CO_2 red spike ($\nu < 2200$ cm^{-1}). Stack and background clusters are not included in Figure 33, since spectra associated with these clusters were not fitted to the plume model.

A nonlinear least squares fitting routine was implemented to produce a best fit of the average spectrum from each plume region to the plume model. Spectrum to the left of the CO_2 red spike ($\nu < 2200$ cm^{-1}) and to the right of the CO_2 blue spike ($\nu > 2420$ cm^{-1}) were fitted independently. The spectral region between 2200-2400 cm^{-1} was purposely omitted in fitting the data to the single-temperature plume model, since more optically thin CO_2 spectral features are present in the spectra left of the CO_2 red spike, and the shape of the CO_2 red and blue spikes are highly susceptible to temperature gradients, which are known to exist within the the plume. Fit parameters consisted of plume temperature, T_p, and column densities for each of the plume constituents ($q_i l$). Temperatures based on spectral fits for the eighteen plume regions are shown in Figure 34 for both spectral regions. A better estimate of temperature is expected from the left-side of the spectrum, due to an increased number of temperature-dependent spectral lines associated with CO and CO_2. An

Table 2. Spectral features used as inputs to the K-means clustering algorithm. Spectral regions were selected based on spectral features associated with one of the identified plume constituents. Spectral features from all plume constituents were identified and incorporated into the K-means clustering routine.

Spectral region (cm^{-1})	Corresponding plume constituent
1873-1877	NO
1893-1901	NO
2057.5-2059	CO_2
2076-2080	CO_2
2093-2094.5	CO_2
2128-2130	CO_2
2170-2186	CO
2208-2240	CO_2
2385-2395	CO_2
2460-2530	SO_2
2795-2801	HCl
2960-2964	HCl
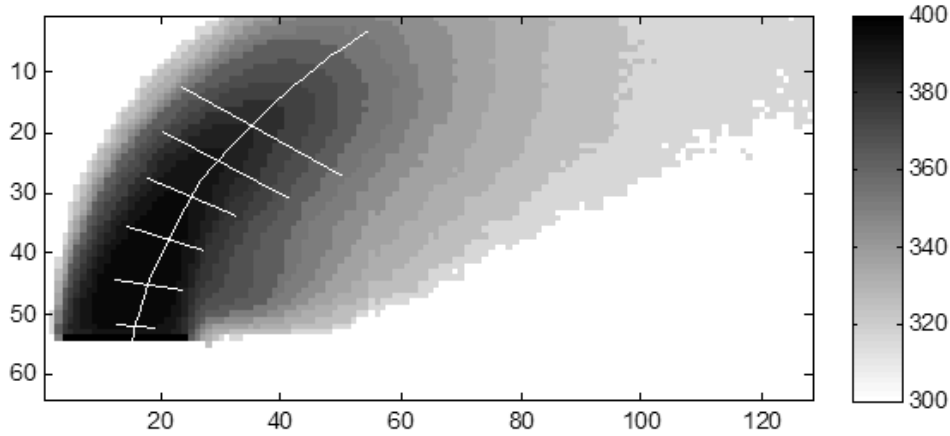
Figure 33. Clustering of all pixels into one of twenty-five regions, based on spectral features from identified plume constituents. The K-means clustering resulted in eighteen distinct plume regions, with fitted temperatures (in K) as shown. Pixel locations are labeled on the left and bottom axes, with pixel dimension at the plume of 21 cm x 21 cm. The stack and background features are not included in this figure, since spectra from only plume regions were fitted to the single-temperature model. The white line that is superimposed on the image, following the plume contour at centerline, is used as reference for measuring plume length, while the grouping of lines perpendicular to plume centerline depict plume width for some of the plume clusters.

in-stack measurement of 406 K was provided by the stack operator, as marked with a circle in Figure 34, compared to the fitted temperature values at the central core region of the plume, closest to the stack exit, of 401 ± 0.36 K and 395 ± 0.36 K, for the left- and right-side spectra, respectively. Error values are based on the statistics of the fit and do not include the effects of systematic errors present in the simplified radiative transfer model. Based on the 5 K temperature difference when fitting the two sides of the spectrum to the single-temperature model, a temperature fitting error on the order of $\pm$ 5 K is not unreasonable.

For the region of the plume closest to the stack, the plume shape is assumed to be cylindrical, with a diameter equal to that of the stack (4.2 m). For this region of the plume, it is possible to estimate molecular concentrations by assuming that the plume depth (l) was equal to its width (stack diameter) and dividing column density for each molecular constituent within this plume region by $l = 420$ cm. In this manner, in-stack measurements of plume concentrations provided by the stack operator could be compared to those obtained via spectral fitting of the data to the single-temperature plume model. Table 3 contains values obtained for all plume parameters alongside those provided by the stack operator. In-stack measurements of H_2O, CO, and HCl were not provided, and an *in situ* measurement of NO_x was provided, as opposed to NO. As with temperature, error bounds on fit parameters are associated exclusively with statistical fitting errors.

From the clustered spectral data, spatial variation in column densities for plume constituents were obtained as a function of plume diameter (Figure 35) and plume length (Figure 36). Only plume regions confined to the extent of the instrument FOV were analyzed in this manner, limiting the dataset to eight points as a function of plume diameter and nine points as a function of plume length. A line was drawn along the centerline of the plume, as shown in Figure 33, and plume length was
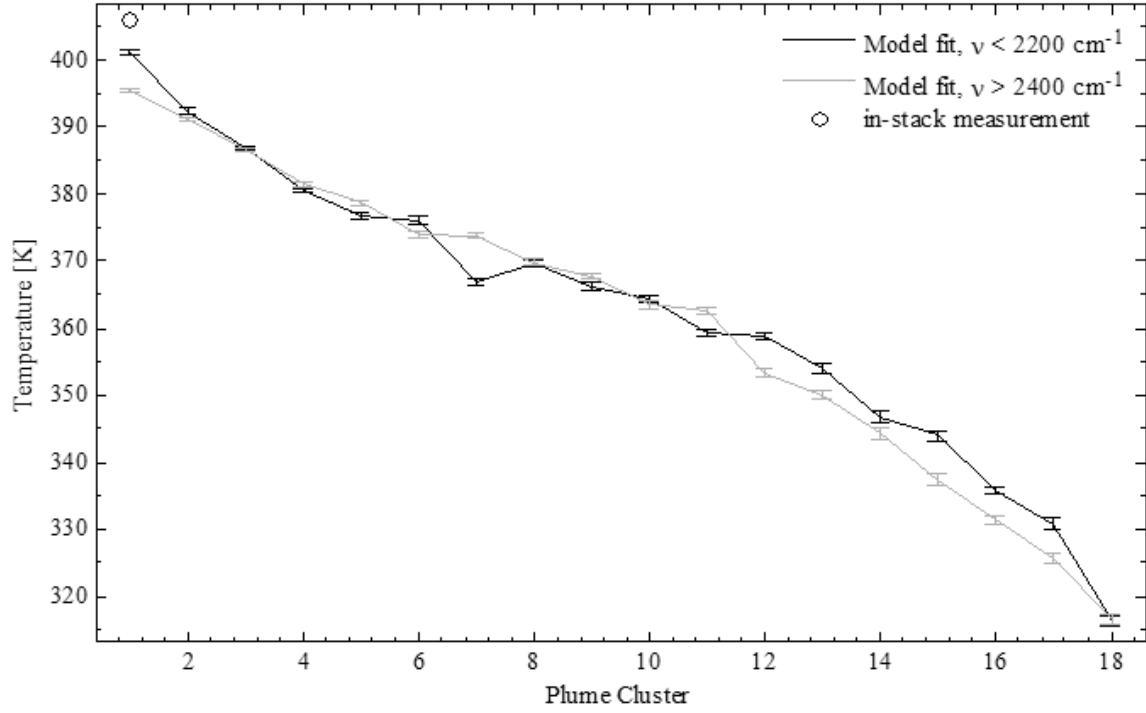
Figure 34. Fitted temperatures for each of the eighteen plume clusters. The plume spectrum to the left of the CO_2 red spike (black) and right of the CO_2 blue spike (gray) were fitted independently, and a small temperature variation between the two is evident. Also shown is the in-stack temperature measurement of 406 K, depicted by a black circle.

Table 3. Comparison of in-stack measurements to those obtained via spectral fitting of the data. Some values (labeled n/a) were not provided by the stack operator. *An in-stack measurement of NO_x was reported, while only NO concentration was obtained spectrally.

	In-stack	Model-fit
Temperature [K]	406	401 ± 0.36
CO_2 [ppmV]	94,000	$110,400 \pm 950$
SO_2 [ppmV]	382	382 ± 4
NO [ppmV]	120*	140 ± 1
H_2O [ppmV]	n/a	$72,976 \pm 800$
CO [ppmV]	n/a	19 ± 0.2
HCl [ppmV]	n/a	111 ± 1

obtained by measuring distance from the stack exit to the tip of each plume region, moving along plume centerline. Similarly, plume diameter was obtained by measuring distance in the direction perpendicular to centerline at the widest point of each plume region. Representative lines associated with plume width measurements for some of the clusters are depicted in Figure 33.

Column density values for all plume constituents decrease rapidly as a function of plume diameter, and appear to asymptotically approach a lower bound at a plume diameter between 5-6 meters, with a stack diameter of 4.2 meters. The rapid decline in column density away from centerline is most likely due to a decrease in plume pathlength, as opposed to a significant decrease in concentration. On the other hand, the decrease in column density for plume constituents as a function of plume length is likely due to a combination of plume expansion, which would result in a change in column density by a factor of $\frac{1}{k^2}$ for a change in plume width by a factor of k downplume, and the cooling of the plume, allowing for mixing of plume with atmosphere, resulting in a decrease in plume concentration. Further analysis of the plume structure would be required to explain these trends in more detail. A better estimation of the plume structure downplume would also result in the ability to separate concentration (q_i) from pathlength (l), resulting in a spatial map of concentrations. With the current analysis, aside from the plume region closest to the stack exit, only column densities were obtained.

In both Figures 35 and 36, the column density profile plots of HCl and SO_2 have a similar shape, as do those of CO_2, CO, and NO. Each grouping of molecules was fit independently of the other, since HCl and SO_2 spectral features are located to the right of the CO_2 blue spike ($\nu > 2420$ cm^{-1}), while spectral features for the other molecular group are located to the left of the CO_2 red spike ($\nu < 2200$ cm^{-1}). It was also noted that fitted temperatures for each of the spectral regions were closely
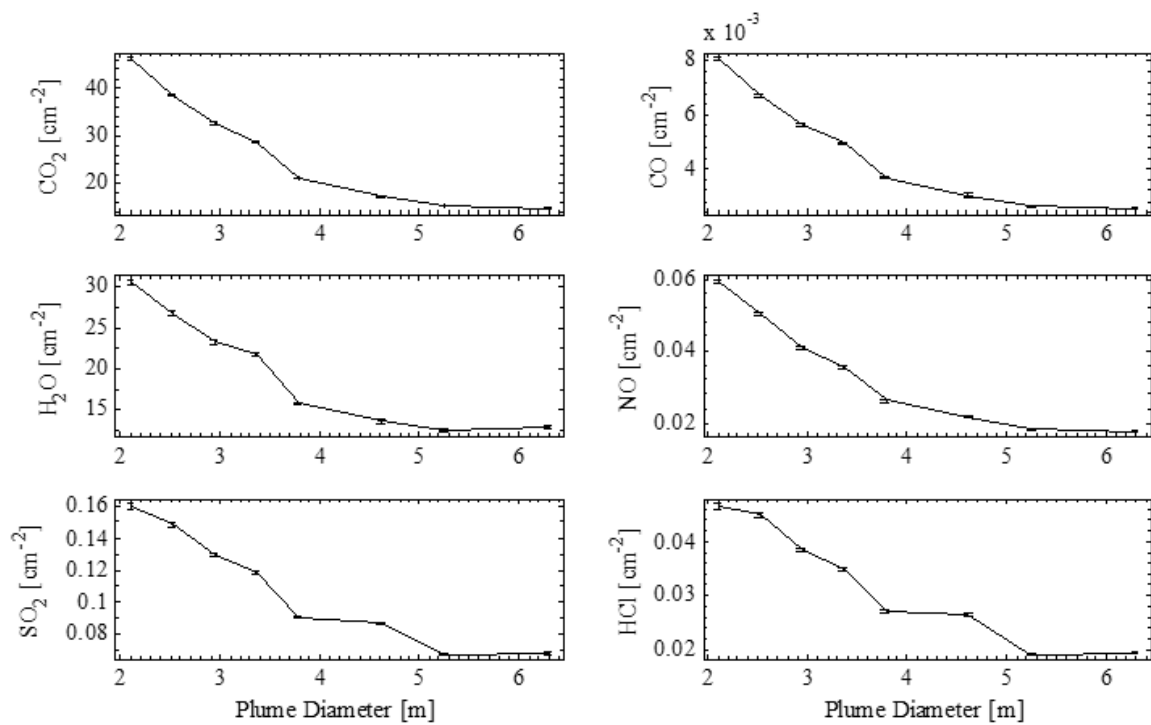
Figure 35. Spatial profile of stack plume effluent column densities as a function of plume diameter.
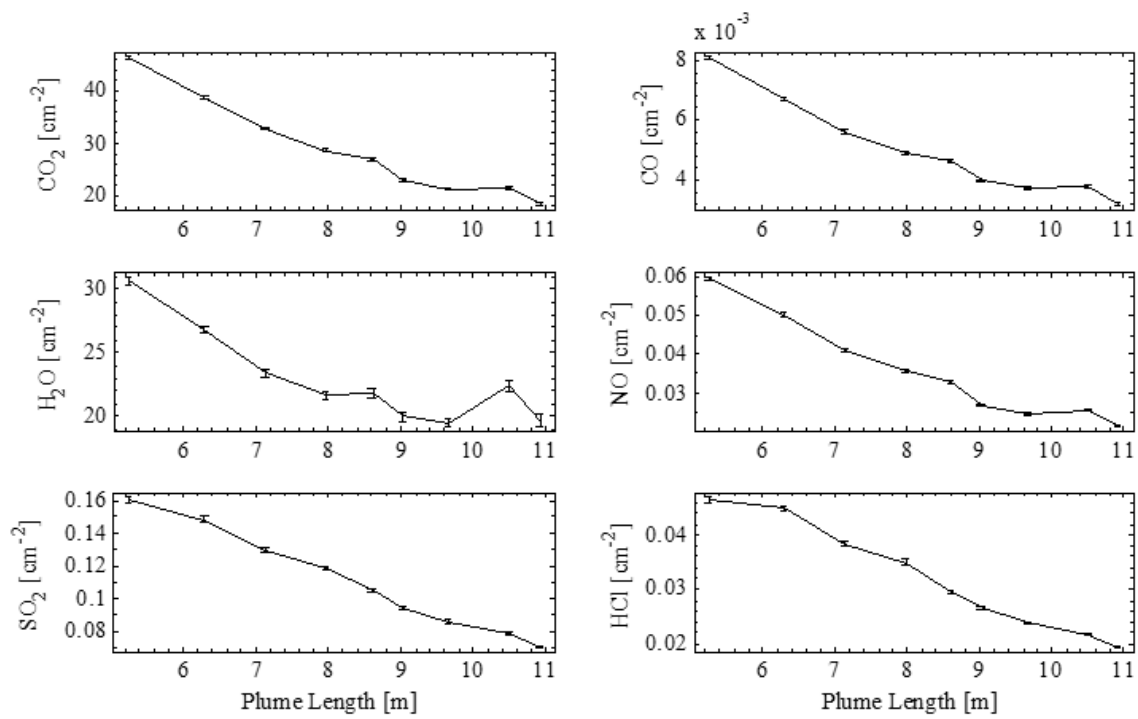
Figure 36. Spatial profile of stack plume effluent column densities as a function of plume length.

aligned (see Figure 34), but a temperature difference was noted between the two. The accuracy with which column densities are obtainable for plume constituents depends upon the accuracy with which temperatures are obtained. Due to the small variation (maximum of 7 K) in temperature between fitting the left- and right-side of the plume spectrum, and the small (5 K) difference between the fitted value near stack exit and the in-stack measured value, it is assumed that fitted temperatures are accurate to within $\pm$ 5 K.

In general, the magnitude of the fit residuals was only a few percent of the measured spetrum. However, sysetmatic variations in the residuals were clearly present. The spectral structure associated with residual error obtained from fitting plume spectra to the single-temperature model was very similar for all plume clusters. Normalized residuals associated with three plume regions are shown in the bottom subplot of Figure 37, with the top subplot displaying the corresponding spectra to the left of the CO_2 red spike, normalized by spectral area. Moving downplume, and away from stack centerline, the error due to fitting the plume spectrum to a single-temperature model decreases considerably. This suggests that at the hottest region of the plume (Cluster 1), a more sophisticated, multiple layer model is needed to accurately describe the spectrum. It is reasonable to assume temperature and concentration gradients exist in the mixing layer between the hot plume and ambient atmosphere. Although the exact number of plume layers needed to model the plume at a given location is not known, it is theorized that there are fewer plume layers as you propagate to plume regions further downplume and away from centerline. Assuming residual structure is due to error associated with attempting to fit spectra from a multi-layer plume to a single-temperature plume model, plume regions that are closer to ambient and have fewer layers should have less pronounced residuals. This trend is observed in the smokestack plume data, and is shown in the bottom subplot of Figure 37.
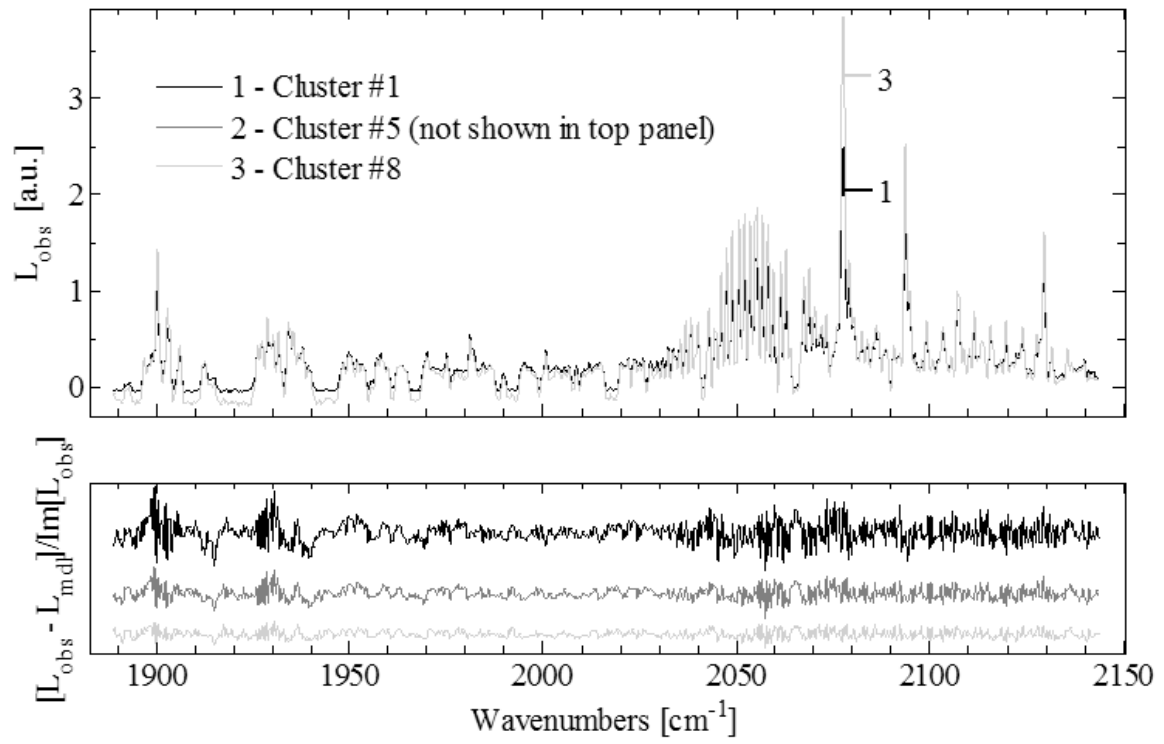
Figure 37. Variation in residuals with plume location.

The first-ever collection of MWIR hyperspectral imagery of industrial stack effluents was obtained at a spectral resolution of 0.25 cm^{-1}. The large dataset was reduced significantly by temporal averaging and k-means clustering to obtain average spectra from similar plume regions. Dimensionality reduction from 100 datacubes, each containing 8,192 pixels to 18 clusters from one temporally-averaged datacube was achieved. The left- and right-side of the spectra from these 18 clusters were then fitted to a single-temperature plume model, resulting in fitted values that resembled those obtained via *in situ* measurement techniques. As with the jet engine exhaust data, systematic errors indicate additional information content related to the radiative transfer problem exists in the spatially clustered stack plume spectra. This indicates that a multiple layer plume model may improve the fit of the data, although at the cost of additional complexity and analysis time. A single-temperature model gives a reasonably good approximation of the plume composition and temperature, and, with a better understanding of plume behavior, may include enough fidelity to be able to obtain spatial mappings of concentrations and temperatures downplume.

Future work should focus on obtaining a better understanding of plume dynamics. A motivated researcher with a strong background in fluid dynamics may be able to approach this dataset, or one similar to it, from a perspective that could allow for a more physical model to be realized. An improved model should take into account both temperature gradients and the geometry associated with plume propagation.

VII. Detection of Chemical and Biological Agents Simulants with the Telops FIRST-MWE

7.1 Introduction

In recent years, homeland defense and national security interests have resulted in an increased focus on chemical and biological agent detection and defeat. Standoff chemical detection has been demonstrated using various imaging spectrometers.[24; 41; 27; 42; 52; 51; 75] Although the emphasis of research has been in the long wave infrared (LWIR) for instrument and algorithm development, the potential for chemical and biological agent detection in the midwave infrared (MWIR) has been demonstrated without a clear understanding of the phenomenology.[41]

Pacific Advanced Technology (PAT) developed a small, handheld imaging spectrometer based on a patented Image Multi-spectral Sensing (IMSS) technique. IMSS uses diffractive optics in combination with image processing to capture spectral information about the object scene. PAT participated in a series of field trials at Dugway Proving Grounds, UT in 2002 to detect chemical and biological agents. Among their notable achievements during this test was the ability to detect *bacillus globigii* (BG), a simulant of anthrax, from a standoff distance of 3.5 km at night in the MWIR. This result was inexplicable, based on spectral absorption characteristics of BG, but a full understanding of this phenomenon may lead to the capability of detecting chemical or biological agents in the MWIR.[41]

The US Army Research Laboratory (ARL) developed a dual-band hyperspectral imager (DBHSI) for chemical and biological agent detection. The DBHSI uses the PAT IMSS lens in conjunction with a DRS Infrared Technologies cooled dual-band Mercury Cadmium Telluride (MCT) focal plane array (FPA). The LWIR image is formed by 1st order diffraction, and the MWIR image is formed by 2nd order diffrac-

tion, resulting in simultaneous capture of two hyperspectral image cubes covering the 4-5.2 μm and 8-10.4 μm regions. A biological standoff detection field test at Dugway Proving Grounds, UT in June 2005 demonstrated detection of BG and BA (*bacillus anthracis*) in both MWIR and LWIR.[27]

The Air Force Institute of Technology (AFIT) Remote Sensing team has collected hyperspectral imagery of multiple plume types, including turbojet engine exhaust and industrial smokestack effluents using the state-of-the-art Telops FIRST-MWE. These combustion events produce relatively high-temperature plumes with strong spectral signatures in the MWIR, and imaging has allowed for the analysis of spatial variation of temperature and chemical concentration within the plume of interest. In an effort to evaluate the capability of the FIRST-MWE to collect hyperspectral imagery of chemical plumes at near-ambient temperature with much weaker spectral linestrength, the AFIT Remote Sensing team participated in the CBDEWS test conducted at Dugway Proving Grounds, UT in October 2008.

This paper details the first attempt to collect and analyze MWIR hyperspectral imagery of chemical and biological agent simulants with the FIRST-MWE. Remote sensing of plumes of methyl salicilate (MeS) using two dissemination methods are discussed, including analysis of the FIRST-MWE hyperspectral data and MWIR non-imaged spectra collected with the indium antimonide (InSb) detector of a Bomem MR-154 Fourier transform spectrometer (FTS). MeS was a chemical of interest, since it is a simulant of a known tissue blistering agent, distilled mustard (HD), which has potential use in chemical warfare or terrorism.[1] Although the fingerprint region of MeS is in the LWIR region, the absorption spectrum of MeS contains weak spectral lines in the MWIR, as well.

7.2 Test Configuration

7.2.1 Chemical Biological Distributed Early Warning System (CB-DEWS) Test Overview.

The Chemical Biological Distributed Early Warning System (CBDEWS) test was conducted at Dugway Proving Grounds, UT from 29 September - 15 October, 2008. Many of the teams that participated in the test had developed instruments and analysis capabilities for the detection and identification of plumes from chemical and biological agent warfare simulants over the course of several years, and the test was aimed at demonstrating these advanced technologies on behalf of the Joint Project Manager Nuclear Biological Chemical Contamination Avoidance (JPM NBC CA) within the Department of Defense.

The AFIT Remote Sensing team became aware of the test and was invited to participate for the purpose of collecting hyperspectral imagery of chemical and biological agent simulant plumes with the Telops FIRST-MWE. Plumes were formed using a variety of methods, including explosive detonations with C4 and constant-flow release from a non-mobile stack. Based on our team's experience with characterizing explosive events using non-imaging spectrometry, and the concern that signatures in the MWIR may not be strong enough to detect with the FIRST-MWE, we also deployed two Bomem spectrometers and a LWIR thermal imager. These instruments are discussed further in Section 7.3, followed by representative results associated with data collected from each in Section 7.4.

7.2.2 CBDEWS Test Range Setup.

The test range at Dugway Proving Grounds, UT was configured as depicted in Figure 38. Various instrumentation teams were placed within the circle of approximately 2 km radius. The straight lines within the figure depict roads for access to
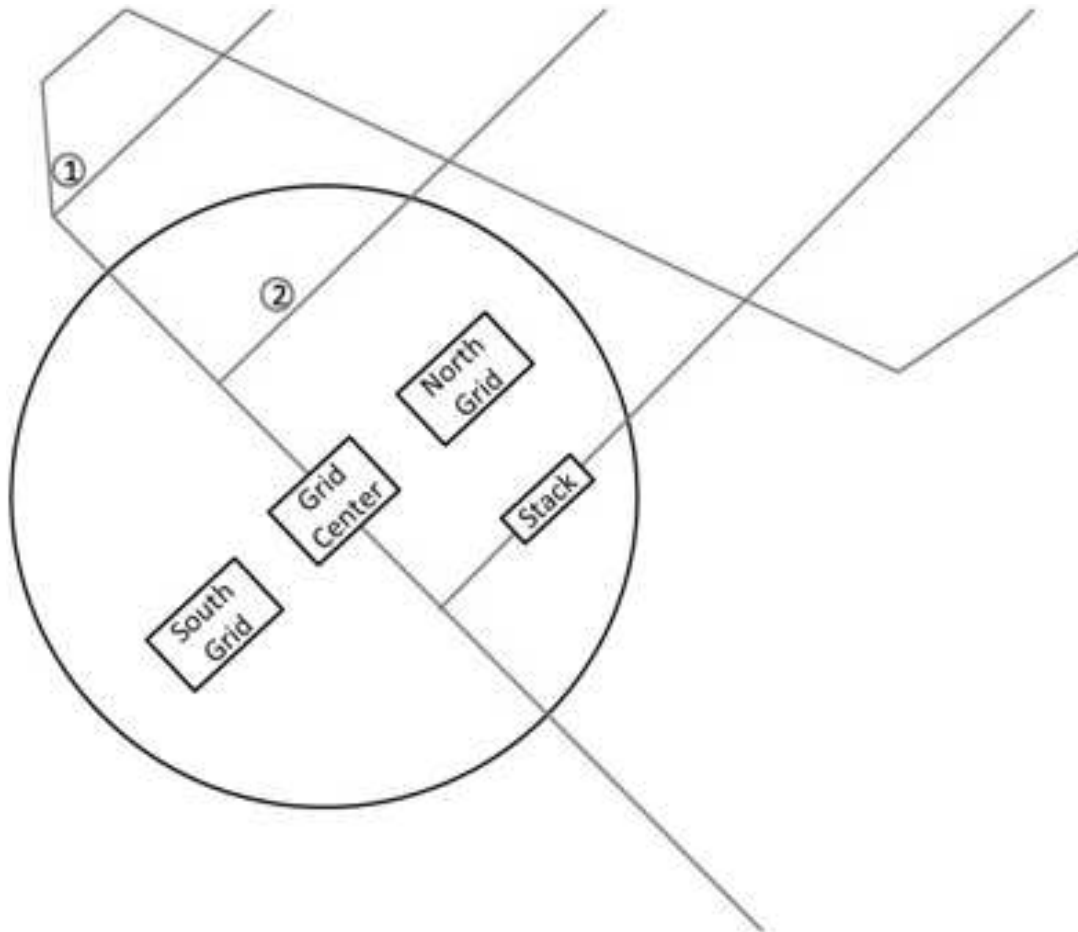
Figure 38. Range setup for CBDEWS Testing at Dugway Proving Grounds, UT. Location 1 refers to the AFIT Remote Sensing team site for the first week of testing. We advanced to site 2 for subsequent weeks of testing. Explosive detonation events were positioned in an array on North Grid and South Grid. Non-mobile stack release events occurred at the location marked Stack. From site 1 to Grid Center was approximately 2 km. Distance from site 2 to Grid Center was approximately 1 km, and provided the team with a much improved view of all event types.

instrumentation team test sites. To the left and right of Grid Center are the two explosive detonation grids, identified in the figure by South Grid and North Grid, respectively. A non-mobile stack was used to produce chemical plumes similar in structure to industrial smokestack effluents, but with the stack configuration parallel to the ground. The non-mobile stack, identified in Figure 1 as Stack, was located approximately 0.5 km behind North Grid. The AFIT Remote Sensing team was positioned at location 1 for the first week of testing. Due to the inability to fill the non-imaging spectrometer field-of-view with the plume source and the weakness of source signal strength following propagation from source to sensor over the 2 km pathlength, the team advanced to location 2 for subsequent weeks of testing. All data presented in this paper was collected from location 2, with telescopes in place on both the FIRST-MWE and non-imaging spectrometers. Since the LWIR QWIP camera was used mainly to provide the team with a wide field-of-view of the test scene, it was not fitted with a telescope for close-in focusing of the plume sources.

7.3 Instrumentation

7.3.1 Telops FIRST-MWE.

The Telops FIRST-MWE is an imaging FTS with a spectral range of 1800-6667 cm^{-1} (1.5-5.5 μm) and user-defined spectral resolution between 0.25-150 cm^{-1}. It has a 320x256 pixel Stirling-cooled InSb FPA. The spatial extent of the scene can be windowed to improve temporal resolution with a smaller field of view. The FIRST-MWE has an individual pixel field of view (IFOV) of 0.35 mrad and uses a 16-tap read-out-integrated-circuit (ROIC) to achieve fast data rates. Temporal resolution is entirely dependent on instrument settings. In observing non-mobile stack releases of chemical warfare agent simulants, a window size of 128x64 pixels was used. For the detonation events, the instrument was set to a 128x128 pixel FOV. For both event

94

Figure 39. AFIT Remote Sensing team test setup at site 2. From left to right, the instruments used to collect test data: Telops FIRST-MWE, with optional telescope in place; FLIR QWIP Camera; Phantom camera; Canon camera; Bomem MR-254 FTS; Bomem MR-154 FTS. A water chiller to help cool the FIRST-MWE is located at the far left of the image, and a wide-area blackbody, used for FTS calibration, is located between the two Bomem spectrometers, to the right of the image. The instruments were monitored by a 3-person team from the control center of computer systems, shaded by the two-sided tent.

types, spectral resolution was set to 8 cm^{-1}, with a constant integration time of 100 μs.

7.3.2   Bomem MR-154.

The Bomem MR-154 is a non-imaging FTS with two liquid nitrogen cooled detectors. The MCT detector responds well to LWIR signatures between 500-2500 cm^{-1}, while the InSb detector has an instrument response in the MWIR between 1800-3000 cm^{-1}. The MR-154 was set to a spectral resolution of 8 cm^{-1} when observing both stack releases and explosive detonations of chemical warfare agent simulants.

7.3.3   FLIR QWIP Camera.

Thermal imagery was obtained with a FLIR LWIR quantum well infrared photodetector (QWIP). With a noise equivalent temperature difference (NETD) of <35 mK, this Stirling-cooled ThermoVision HS series camera is well-suited for the detection of thermal contrast between scene features. Combined with its wide field of view, thermal imagery proved to be an invaluable tool for the purpose of aligning instruments for night-time test events. It has a 320x256 pixel FPA, with a spectral bandpass of 8-9.2 μm (1087-1250 cm^{-1}). Without windowing the FOV from its full size, a frame rate of 420 Hz is possible, allowing for high-speed thermal imagery.

7.4   Results and Discussion

Preliminary analysis of data collected by observing MeS plumes disseminated from a non-mobile stack and by an explosive detonation release is presented in this section. MeS plume characterization using both imaging and non-imaging FTS is discussed.

7.4.1 Non-mobile stack release of methyl salicilate (MeS).

A stack was mounted to a stationary truck with the exit nozzle protruding beyond the truck cab, as shown in Figure 40. MeS was dispersed from the exit nozzle in a relatively steady flow volume for several minutes. The image on the left was collected with a visible camera boresighted to the telescope of the FIRST-MWE. The thermal image on the right was collected with the QWIP camera during the same test event. The much wider field-of-view of the QWIP provided a thermal image of the MeS plume, and displays the plume as it propagates well above the mountains.

Figure 40. Non-mobile stack release of MeS. Left: Visible image acquired with the boresighted camera of the Telops FIRST-MWE during data collection, with telescope in place. Right: LWIR thermal image acquired by the FLIR QWIP camera during the same test event.

The FIRST-MWE hyperspectral data collected during the MeS stack release was converted to spectra, and is presented in Figure 41. The top subplot of Figure 41 shows the spectrum from a plume pixel overlayed by that of a representative background pixel, while the bottom subplot shows the plume spectrum following background subtraction. This difference spectrum (plume - background) contains a broadband feature between 2000 and 2200 cm^{-1}, which is not associated with MeS emission. The spectral assignment of this feature has not yet been determined and is currently being investigated, but it is possibly associated with plume reflectance of

solar radiation or due to other chemicals within the plume.
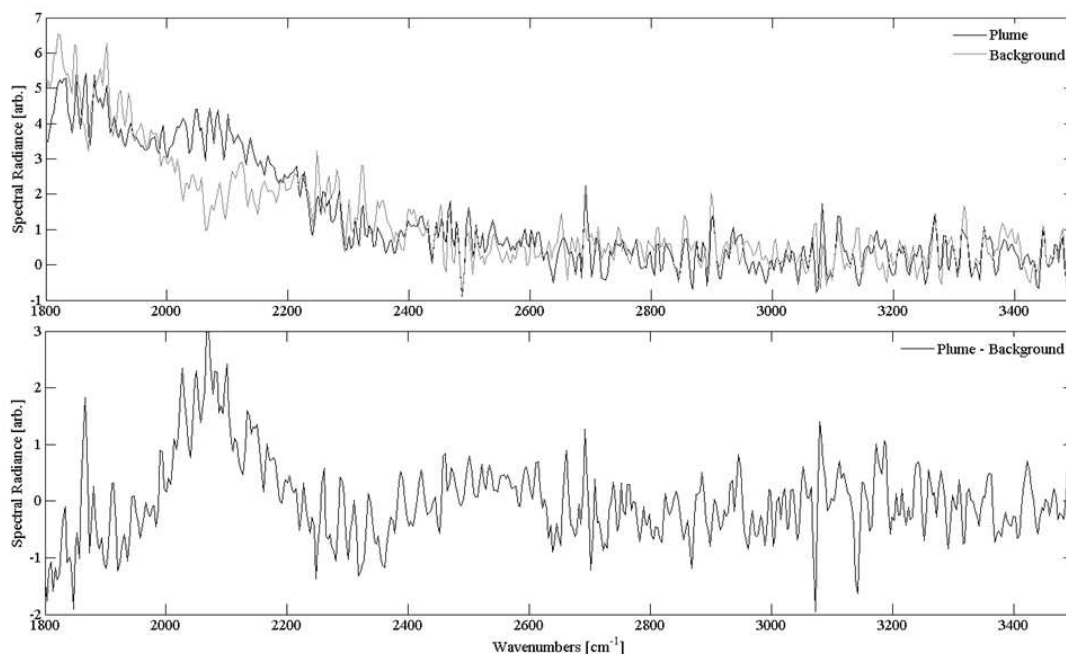
Figure 41. Non-mobile stack release of MeS. Spectra of a plume pixel and background pixel from the same FIRST-MWE hyperspectral datacube, accompanied by a plot of the background-subtracted plume spectrum.

To aid in analysis, non-imaged MWIR spectra of the MeS stack release were collected with the Bomem MR-154. As with the FIRST-MWE, the MR-154 was fitted with a telescope to focus the instrument field-of-view on a region of the plume near the exit nozzle of the stack. The top subplot of Figure 42 shows the plume spectrum collected with the MR-154 immediately before the stack was turned off overlayed by the background spectrum. The imaginary part of the complex spectrum is also plotted, providing an estimate of the noise level in the signal. The bottom subplot of Figure 42 contains a temporal plot of normalized radiance, which reaches its peak at the datapoint which is labeled by a circle at t=8.5 seconds, and recovers to a baseline level just before t=10 seconds. The large value of normalized radiance before t=8.5 seconds is associated with the presence of plume within the field-of-view. The region beyond 10 seconds is associated with the plume no longer being present,

98

since the stack was turned off immediately after the selected temporal datapoint. The mean spectrum from the last five seconds of data was used to calculate the background spectrum. Background subtraction was performed in post-processing, resulting in a plot of the difference between the current spectrum (plume spectrum at t=8.5 seconds) and the mean spectrum (background) in the middle subplot of Figure 42. The difference spectrum from the FIRST-MWE and the MR-154 are very similar, each having broad spectral features between 2000 and 2200 cm^{-1}. This spectral feature is not yet understood completely.
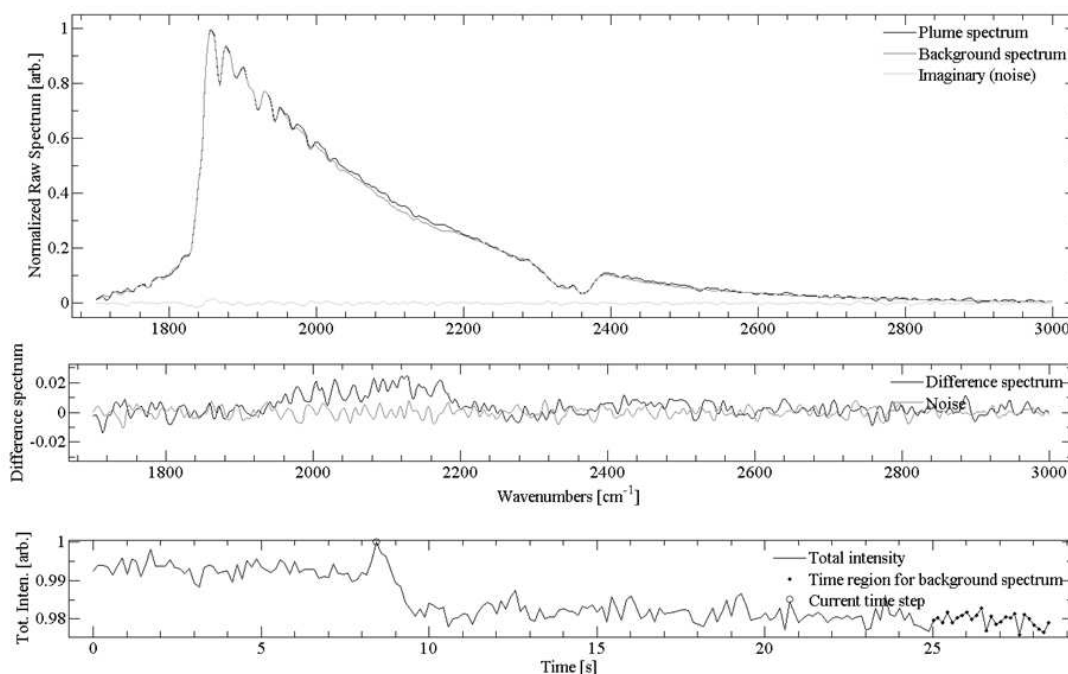
Figure 42. FTS data collected with the InSb detector of the Bomem MR-154 during the non-mobile stack release of MeS. In the top subplot, the MeS plume spectrum immediately before the stack is shut off is overlayed by the background spectrum, calculated as the mean spectrum for the last 5 seconds of data, as marked in the bottom subplot. The middle subplot shows the difference spectrum (plume - background). The bottom subplot depicts the temporal change in normalized radiance, clearly delineating between plume and background scenes.

7.4.2 Explosive detonation release of methyl salicilate (MeS).

An alternate method of producing an MeS plume is by explosive detonation of a plastic container of MeS. This produces a chemical plume that is much less pure than that obtained by release from a non-mobile stack, due to the mixing of dust, particulate matter from the container, and explosive combustion by-products with MeS. Additionally, the plume structure evolves very quickly, unlike the relatively steady plume structure associated with a non-mobile stack release. Figure 43 shows four frames acquired with the FLIR QWIP camera from the simultaneous explosive detonations of four containers of MeS. These are organized temporally from top left to bottom right. The wind direction was from left to right in the image, as demonstrated by the plume movement, most notable in the bottom right image as compared to the bottom left image. The black square within each image frame depicts the corresponding field-of-view of the FIRST-MWE visible camera, with telescope in place. As evidenced by the relatively low thermal contrast between plume and background in the bottom two images, the plume rapidly approached ambient temperature following the detonation event.

As with the thermal images captured by the FLIR QWIP camera, a series of visible images of the explosive detonation release of MeS was acquired with the Telops FIRST-MWE boresighted visible camera. In Figure 7, four such images are organized temporally from top left to bottom right. The black square within each of these image frames corresponds to the field-of-view of the FIRST-MWE imaging FTS. Each visible image collected by the FIRST-MWE corresponds to an image of the scene during the collection of one hyperspectral datacube.

The datacube corresponding to the image in the top right corner of Figure 44 exhibited interesting scene-change features in interferogram space, due to the blast effects that presented themselves during data collection. A MWIR image is acquired
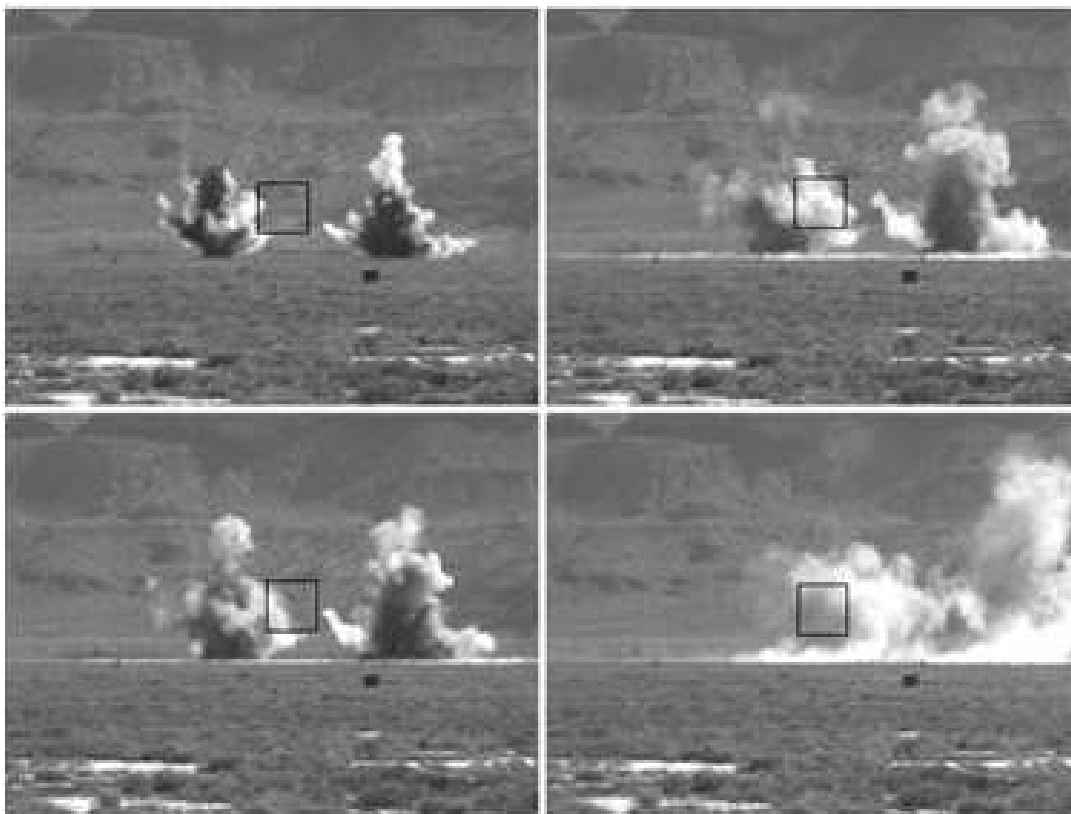
Figure 43. A series of LWIR thermal images of the explosive detonation release of MeS was acquired with the **FLIR QWIP**. Four such images are organized temporally from top left to bottom right. The black square within each image frame depicts the corresponding field-of-view of the **FIRST-MWE** visible camera, with telescope in place.

by the FIRST-MWE at each optical path difference (OPD) of the internal Michelson interferometer. With the instrument settings for this data collection (128x128 pixels, 8 cm^{-1} spectral resolution, 100 sec integration time), the datacube consists of a total of 2370 images at approximately 250 sec temporal resolution, one for each OPD position. The 128x128 pixel images corresponding to OPD positions 354, 375, 400, and 500 in interferogram space are shown in Figure 45.

Figure 44. A series of images of the explosive detonation release of MeS was acquired with the FIRST-MWE boresighted visible camera, with telescope in place. Four such images are organized temporally from top left to bottom right. The black square within each image frame depicts the corresponding FOV of the FIRST-MWE imaging FTS.

Figure 46 shows interferograms extracted from four pixels in the hyperspectral datacube portrayed in the OPD images of Figure 45. The top left interferogram is from a pixel near the bottom left corner of the datacube, pixel (3,3), which at OPD position 354, saw the initial blast front from the detonation event. Subsequent blast
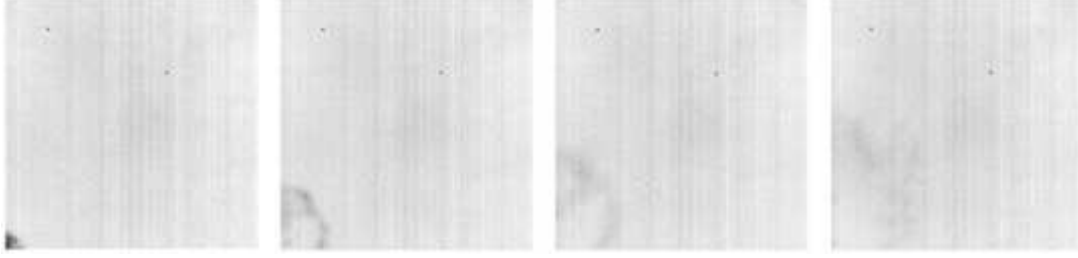
Figure 45. Images extracted from a single hyperspectral datacube from the FIRST-MWE, collected at OPD positions 354, 375, 400, and 500 during the explosive release of MeS depicted in the top right image of Figure 44

effects were witnessed at this pixel location between OPD positions 354 and 500, as evidenced by the sequence of lower-amplitude peaks in the interferogram. The top right interferogram corresponds to pixel (3,5), which captured the first blast effect at OPD position 354, but did not witness the subsequent blast effects, as they did not enter its IFOV. The bottom-left interferogram is associated with pixel (50,50), near the center of the image scene. The ramp-up that occurs near OPD position 500 is likely due to the emergence of the plume into its IFOV. Finally, the bottom-right interferogram corresponds to pixel (100,100), near the top-right of the image scene. It is considered a background pixel, since the plume never enters its IFOV. Subsequently, no significant scene change features are evident in its interferogram.

Non-imaged spectra were collected with the InSb detector of the Bomem MR-154 during the same explosive detonation release of MeS. A temporal plot of normalized radiance is shown in Figure 47. The mean spectral radiance from the first three seconds of data is used as the background spectrum. The detonation event takes place at the localized peak around t=5 s, and marked with a circle in Figure 47. Other temporal features of interest are the minimum value of normalized radiance, labeled with a square approximately 1 second post-detonation, and the new baseline level following a 4-second ramp-up in normalized radiance. This new baseline remains for the duration of the temporal plot. The spectrum associated with the datapoint
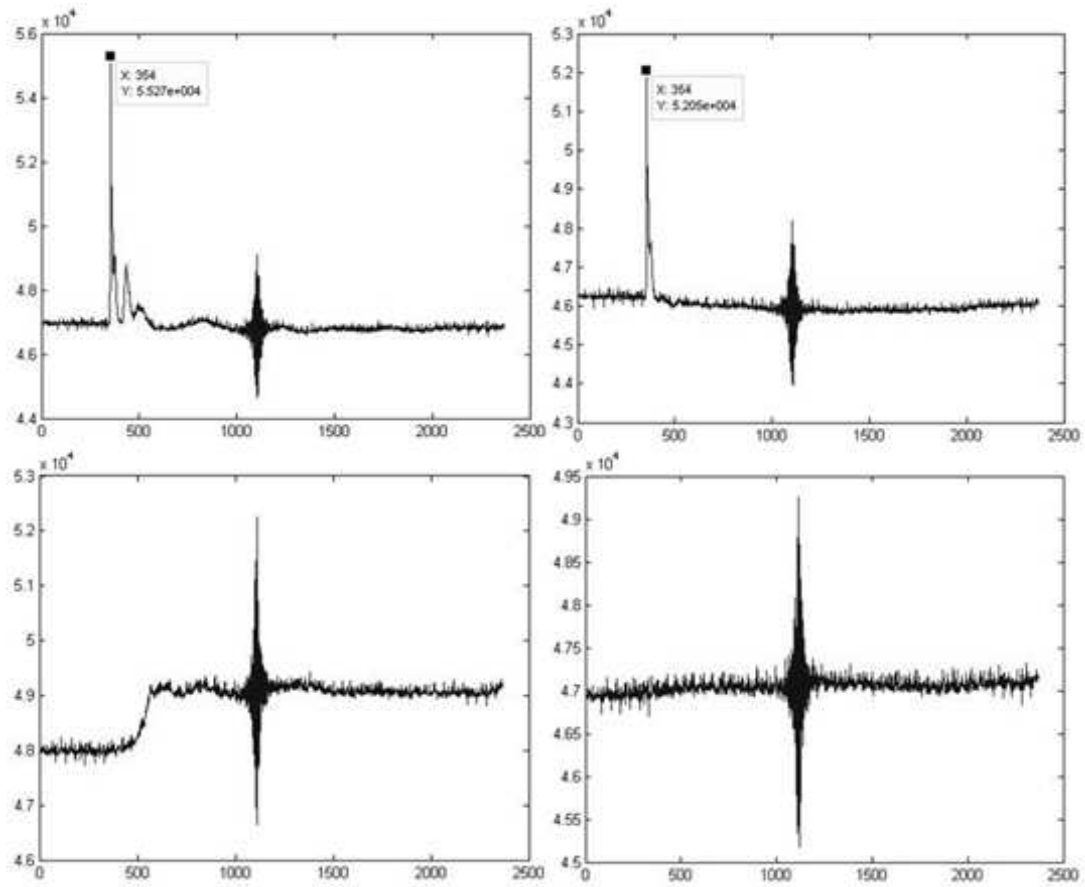
Figure 46. Interferograms extracted from four pixels in the hyperspectral datacube portrayed in the OPD images of Figure 45. From top-left to bottom-right, these interferograms correspond to pixels (3,3), (3,5), (50,50), and (100,100).

labeled with a triangle in Figure 47 will represent this post-detonation baseline region in the analysis that follows.

Figure 48 presents a plot of the normalized spectral radiance corresponding to the detonation event, labeled with a circle in Figure 47. Both the plume spectrum and background spectrum are overlayed on the same figure, along with a plot of the imaginary part of the normalized complex spectral radiance, which gives an estimate of the current instrument noise level. The plume and background spectra are very similar, and background subtraction is necessary to uncover spectral features associated with the plume.
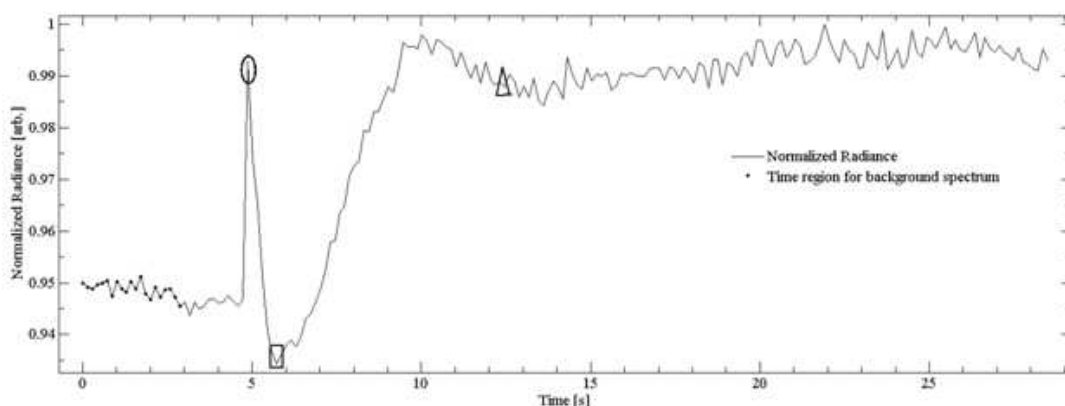
Figure 47. Temporal plot of normalized radiance collected by the MR-154 InSb detector during the explosive detonation release of MeS. Spectra associated with the initial 3-seconds of data is used to compute the background spectrum. The detonation event, labeled with a circle, occurs at t=5 s. This is followed by a temporal minimum, labeled by a square, approximately 1 second post-detonation and a 4-second ramp-up to a new baseline level, with one such datapoint labeled with a triangle.

Figure 49 presents background-subtracted plume spectra for each of the three temporal datapoints identified in the temporal plot of normalized radiance. The three subplots of Figure 49, from top to bottom, correspond to the datapoints labeled with a circle, square, and triangle in Figure 47. The first subplot of Figure 49 corresponds to the background-subtracted plume spectrum associated with the detonation of MeS. Similar to the FIRST-MWE data, a broad spectral feature exists between 1900-2200 cm^{-1}. An additional broad spectral feature, but not as pronounced, exists between

105
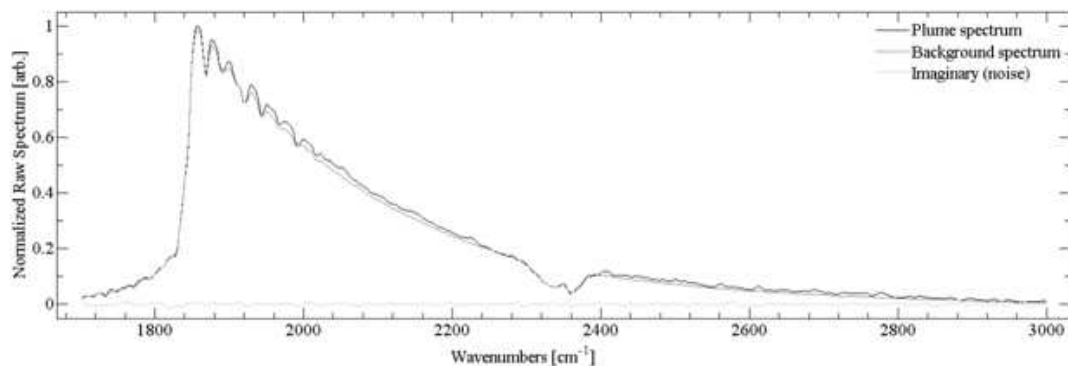
Figure 48. Spectrum associated with the detonation of MeS. The circle in Figure 10 marks the time step associated with the plume spectrum, which corresponds to the localized peak of normalized radiance. This plume spectrum is overlayed with the background spectrum and the instrument noise.
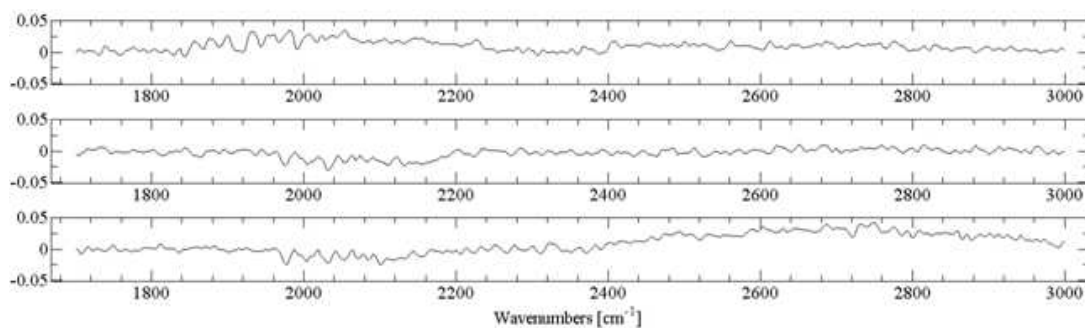
Figure 49. Background-subtracted plume spectra from three distinct temporal data-points. Top: MeS detonation event spectrum. Middle: Spectrum associated with minimum normalized radiance. Bottom: New baseline spectrum, following the 4-second ramp-up from the temporal minimum value of normalized radiance.

2400-2800 cm^{-1}. Neither feature is characteristic of the emission of MeS, but spectral assignment is currently under investigation. The second subplot of Figure 49 shows the spectrum associated with the minimum value of normalized radiance viewed by the MR-154 during this 30-second data collection. This minimum is encountered approximately one second after the MeS detonation event. A negative-valued broad spectral feature between 2000-2200 cm^{-1} is evident, and the spectral feature that was identified in the first subplot beyond 2400 cm^{-1} does not present itself in this spectrum. After reaching a minimum, the normalized radiance gradually increases over a 4 second time period, resulting in a new baseline level, as shown in the temporal plot of Figure 47, and represented by the datapoint marked with a triangle in the same figure. The background-subtracted plume spectrum associated with this temporal datapoint is displayed in the bottom subplot of Figure 49. The plume spectrum during this new baseline region exhibits interesting spectral features. While the spectral region between 2000-2200 cm^{-1} maintains a small negative value, the emergence of a large positive-valued spectral feature beyond 2400 cm^{-1} results in an increase in normalized radiance. These spectral features present potentially interesting phenomena that are not yet understood.

7.5   Conclusion

Remote detection of plumes from dissemination of chemical agent simulants in the MWIR was demonstrated, although further analysis is necessary to evaluate the spectral features present in the imaging and non-imaging FTS spectra. Dissemination of MeS via stack release and explosive detonation were observed remotely by a suite of instruments, including the Telops FIRST-MWE and Bomem MR-154. Further analysis of the MWIR data will be necessary to determine the utility of this spectral region for remote detection of chemical threat agents. Both imaging and non-imaging

Fourier transform spectrometers demonstrated their respective strengths for this type of data collection, with the former being capable of collecting plume and background signatures simultaneously in different pixels of the FPA, while the latter demonstrated its utility for temporal analysis of rapidly evolving chemical plumes disseminated by explosive detonation. In both cases, background-subtracted MWIR spectra of the MeS plumes contained similar features, which have not yet been identified. Future work will focus on the spectral assignment of these broad features.

VIII. Conclusion

Hyperspectral imaging of plumes is a relatively new technique, and the majority of work in this regard is performed in LWIR for purposes of detection of chemicals within a gas cloud. The Environmental Protection Agency (EPA) is planning to assess the capability of IFTS for the purpose of remote detection of industrial smokestack emissions, and jet engine manufacturers have shown interest in the potential utilization of such instruments to validate computational fluid dynamic (CFD) models during the process of engine design and testing. National security interests have the Departments of Defense and Homeland Security constantly on the look-out for instruments that can potentially aid in the fight against terrorism.

With the development of instruments, such as the one used for this research effort, technology has bridged the gap between the possibility of remote detection and analysis of plumes to the first demonstration that spatial and spectral information obtained via hyperspectral imagery can be incorporated, enabling improved remote plume characterization. Although detection and analysis of chemical and biological threat agents will likely always reside most prominently in the LWIR, the MWIR is well-suited for analysis of combustion plumes, including industrial emissions and jet engine exhaust.

8.1 Contributions

This research effort has demonstrated the advantages that imaging Fourier transform spectrometry enjoys over non-imaging spectral techniques in the analysis of two very different combustion sources: industrial smokestack effluents from a coal-burning utility plant and exhaust from a small turbojet engine.

Several key results were achieved by this research effort. We report the first-

ever collection of MWIR hyperspectral imagery of industrial smokestack effluents and jet engine exhaust with an IFTS. Previous work used non-imaging FTS or scanning imaging FTS for analyzing these plume types [40; 6; 28], but none of these efforts contained simultaneous collection of spectra from multiple plume regions or the concurrent collection of background and plume spectra. The Telops FIRST-MWE allowed for this collection capability at high spectral resolution (0.25 cm^{-1} for industrial smokestack effluent data and 1 cm^{-1} for jet engine exhaust data). Temporal averaging of the resulting hyperspectral dataset increased signal strength above noise level by decreasing the modulation associated with the turbulent variability of the plume sources. Spectral features associated with individual plume constituents were readily identified from the pristine datasets.

Using the temporally-averaged plume data, spatial variability of plume spectra was demonstrated for both plume-types, a metric not achieved by the aforementioned research efforts. Due to the increased data volume, a K-means clustering algorithm was employed for dimensionality reduction and separation of plume pixels from non-plume pixels.

A simple radiative transfer plume model was applied to plume regions, allowing for a determination of spatially resolved plume temperatures and concentrations of plume constituents, with very small statistical errors. The spectral structure of the residual error between data and model for both datasets point to a potential improvement that can be met with a multi-layer plume model. This research effort has resulted in an ability to obtain spatially-resolved plume information from simultaneous collection of spectra from an array of pixels within a MWIR hyperspectral image.

8.2 Future Work

As with all successful research findings, the culmination of this research effort leaves several holes to be filled. First, although it was demonstrated that a simple single-temperature plume model was sufficient for close approximation of plume temperature and concentrations, temperature gradients are known to exist in the plume in the direction of instrument line-of-sight. A multi-layer plume model, although more computationally intensive, should result in much better agreement between the data and model. The spatial information obtained from the IFTS data can help define the model framework. For example, clustering has allowed us to separate the plume into distinct regions. The two-dimensional clustered plume image can guide definition of the third-dimension. From the IFTS data, after clustering and fitting to the single-temperature plume model, the following information can be used to develop a more robust model: (1) an estimate of the number of plume layers needed to accurately define the plume at a given pixel location; (2) initial guesses for temperature, column densities, and pathlength for each layer; and (3) initial estimate of residuals. Second, an improved calibration process is necessary to take full advantage of the data that the Telops FIRST-MWE is capable of collecting. The Telops FIRST-MWE FPA was designed for low-light applications, such as viewing stars, and is very sensitive to photons. Although this is an ideal quality for some applications, the FPA is easily saturated by a 90°C blackbody with an integration time greater than 50 μs. Consequently, data collected of high-temperature combustion events are difficult to calibrate and spectra obtained beyond 3000 cm^{-1} can not be converted to calibrated spectra without being highly obscured by noise. The Remote Sensing group at AFIT is currently working with Telops, Inc. to develop a more robust calibration process, which will aid in future data analysis.

Third, although difficult to assess based on the limited amount of data collected

during this research effort, MWIR IFTS may play a future role in detection of chemical and biological threat agents. The AFIT Remote Sensing group was fortunate to be included in the CBDEWS test in October 2008 at Dugway Proving Grounds, UT, and gained a greater appreciation for the challenges associated with collecting and analyzing plumes that are short-lived, at near-ambient temperatures, and obscured by dust.

Further analysis of the existing jet engine and industrial smokestack data should be pursued, with a focus on three key areas. First, for plume analysis up to this point, mean spectra has been obtained by performing a temporal average in interferogram space and converting the mean interferogram into spectra. It has been theorized that, although the mean spectra and median spectra are very similar, the median spectra of a plume pixel is better correlated to plume temperature. Additionally, with large sets of data, statistically varying spectra can be separated into quantiles which have demonstrated some potential correlation with plume turbulence [78]. While computing the mean spectra is much more computationally efficient and gives a good approximation for the steady-state of a turbulent plume, much of the information about the turbulent nature of the combustion plume is lost. This information is likely best found in comparison of median and quantile spectra. A more in-depth study into the phenomenology of plume turbulence as it relates to temporal variation of the dc offset in interferogram space, and the subsequent conversion of quantile interferogram plots into spectra and their analysis is recommended.

Second, a single-temperature model has demonstrated remarkably close approximation to in-stack measurements, but lacks the robustness to provide a more physically realistic model of the plume structure, especially for combustion plumes with large temperature gradients, as is the case with jet engine exhaust. As a next step, the data should be fit to a multiple-layer plume model. It is expected that including

this additional flexibility in the model will result in a fitting algorithm that is more time-consuming and computationally intensive, but will result in more realistic plume temperatures and concentrations, and smaller and less structured residuals.

Third, in addition to the work necessary to improve instrument calibration of the Telops FIRST-MWE, some effort should be put forward in determining the true instrument lineshape. Many of the residuals associated with fitting observed spectra to the simple plume model occur near well-defined spectral features. When the instrument lineshape is not well-defined, accurately modeling the data, even with a robust plume model, will prove to be extremely difficult. Recent research by Harig, *et al.* [29] has demonstrated the benefit of applying a true instrument lineshape for their scanning FTS imaging system as opposed to an ideal lineshape in modeling plume spectra.

Finally, with the first three steps completed satisfactorily, additional data should be obtained for a few purposes. First, jet engine data should be collected at 0.25 cm^{-1} spectral resolution, to allow for improved analysis of spectral features. An decrease in SNR associated with collection at this spectral resolution can be offset by collecting more datacubes, and the associated increase in collection time can be mitigated by reducing the FPA window. Ideally, this data would be collected at night to eliminate, as much as possible, the additional effects of stray radiance. Due to the high temperature of the jet engine plume, temperature difference between plume and background is not a huge concern, but the larger temperature difference associated with a night-time data collection is an added benefit. With improved spectral resolution, collection of data at several engine settings and with varying fuel types may be worthwhile.

The data obtained from the coal-burning industrial stack was phenomenal. Data was collected at night, with a large thermal contrast between plume and background.

113

Spectral features associated with plume constituents were easily assigned, although the spectra was very complicated, due to the larger number of plume constituents, some of which had spectral features that overlapped one another. The observed stack was from a much older, higher-polluting variety that is not required to employ EPA-mandated scrubbers, due to a grandfather provision. It may be worth pursuing a night-time collection of a clean-burning stack with an attempt to extract plume information from the cooler, less emissive plume. A comparison of spectra would be interesting to note, in addition to assessing the capability of the FIRST-MWE to remotely characterize modern industrial stack emissions.

Appendix A. FIRST-MWE Calibration

In addition to the many benefits associated with an IFTS come many challenges that must be addressed. One such difficulty that arises is the spatial non-uniformity of a focal plane array. Essentially, every pixel responds differently to the collection of an equivalent number of photons. Fortunately, a standard technique, described as non-uniformity correction (NUC) can be employed rather easily to overcome this obstacle. A more challenging problem is that of determining the spectral response and instrument self-emission of the IFTS, often defined by spectral gain and offset. An in-depth treatment of these, as applied to the Telops FIRST-MWE can be found in Chapter IV of Captain Spencer Bowen's Master's Thesis [9], but a brief description is found here for convenience.

The NUC process is employed to address two causes of spatial variability of an FPA. First, when no photons are incident on the FPA, a small current, known as dark current, still flows due to the reverse-biased read-out integrated circuit. This dark current varies from pixel-to-pixel, resulting in a spatially varying dark current offset, $o(i,j)$, where i and j are pixel coordinates. When an equal number of photons are incident on the FPA, as is assumed in the case of a large blackbody that fills the instrument FOV, an additional variability due to the degree to which a given pixel converts photons to electrons is present, and can be described as photon response, $g(i,j)$.

By collecting several hyperspectral datacubes of blackbody data at two different temperatures, the values of $g(i,j)$ and $o(i,j)$ can be computed, as described in [9] and repeated in Equation 26 below:

$$
\begin{aligned}
\overline{C_{obs,1}}(i,j,T_1) &= g(i,j)\overline{L_{BB}}(T_1) + o(i,j) \\
\overline{C_{obs,2}}(i,j,T_2) &= g(i,j)\overline{L_{BB}}(T_2) + o(i,j)
\end{aligned}
\tag{26}
$$

where $\overline{C_{obs,1}}(i, j, T_1)$ and $\overline{C_{obs,2}}(i, j, T_2)$ are the individual pixel spectrally-averaged signals obtained when observing blackbodies at temperature T_1 and T_2, respectively, and where $\overline{L_{BB}}(T_1)$ and $\overline{L_{BB}}(T_2)$ are the spectrally-averaged Planckian blackbody functions, defined as the spectral mean of $L_{BB}(\nu, T_i) = \frac{2hc^2\nu^3}{\exp(\frac{hc\nu}{k_B T_i})-1}$.

Non-uniformity correction of hyperspectral data is obtained by applying the dark current offset and photon response to all spectral bins of each pixel (i, j) by subtracting $o(i, j)$ and dividing by $g(i, j)$ from each observed value $L_{obs}(\nu, i, j)$. With the data corrected for non-uniformity, the two-temperature calibration process can be performed to convert uncalibrated spectra to spectral radiance.

Just as the detector material is not uniform spatially, it also varies in its response to photons spectrally. Spectral responsivity of a given detector material justifies its description as being a MWIR detector or LWIR detector. For the Telops FIRST-MWE, an InSb FPA is used, which is responsive in the MWIR. However, it is not equally responsive at all wavelengths within its spectral window. Consequently, the spectral gain must be computed to account for detector response. Although the FPA is shielded as much as possible from emission from other components within the instrument, instrument self-emission, results in a spectrally-varying offset, regardless of the presence of photons.

In theory, pixel-to-pixel variation in detector response and spectral offset is likely. However, with the primary non-uniformity of the detector already accounted for, a spatial average detector response and spectral offset were computed using the two-temperature blackbody calibration data, as follows [9]:

$$
\begin{aligned}
\overline{C_{NUC,1}}(\nu, T_1) &= G(\nu)L_{BB}(\nu, T_1) + O(\nu) \\
\overline{C_{NUC,2}}(\nu, T_2) &= G(\nu)L_{BB}(\nu, T_2) + O(\nu)
\end{aligned}
\tag{27}
$$

116

The resulting spectral structure of $G(\nu)$ and $O(\nu)$ contained high-frequency absorption features corresponding to spectral lines due to primarily atmospheric water and CO_2. A smoothing spline was computed from these highly-structured spectral gain and offset curves to to smooth over the high-frequency content, producing functions that were most easily applied to the data by subtracting the offset and dividing by the gain. In practice, the offset curve was not applied to the data. Instead, a spatial average of spectra from background scene pixels was used as an estimate of instrument self-emission, since stray radiance and other background components were negligible in both sets of hyperspectral data, and instrument self-emission during data collection varied much less than it did during collection of blackbody calibration data. In either case, the same calibration process was applied, with the offset term subtracted from the data and the resulting spectra at each pixel divided by the smoothed spectral gain spline curve. As discussed previously, calibration data was limited to a maximum spectral value of approximately 3000 cm^{-1} due to the decaying signal strength at smaller wavelengths, resulting in much poorer signal-to-noise and a higher level of uncertainty in the spectral response of the FPA.

Appendix B. Spectral Analysis of HCl

Industrial smokestack effluent spectra contained well-defined spectral lines associated with emission of HCl. The spectral resolution of the data was good enough to isolate spectral lines associated with both isotopes, $H^{35}Cl$ and $H^{37}Cl$. An abundance ratio of approximately 2.5:1 was observed between the primary and secondary isotopes. An effort was made to perform some simple calculations based on an assumption that the plume is optically thin in the HCl region of the spectrum.

The plume temperature was measured from the spectral data using the relative heights of the HCl emission peaks. Temperature can be calculated due to the variation in line intensity of rotational-vibrational lines, as detailed in Herzberg [38] and reproduced in Equation 28:

$$
\begin{aligned}
I_{em.} &= \frac{C_{em.}\nu^4}{Q_r}(J' + J'' + 1)\exp\left(\frac{-B'J'(J'+1)hc}{k_B T}\right) \\
&\propto A\nu^4(J' + J'' + 1)\exp\left(\frac{-B'J'(J'+1)hc}{k_B T}\right)
\end{aligned}
\tag{28}
$$

where $I_{em.}$ is the emission intensity peak, A is the J'-dependent Einstein-a coefficient, ν is the spectral frequency location of the emission peak, and B' is the rotational constant, which has a value of 10.44 cm^{-1} for HCl. [38].

By rearranging terms of Equation 28, the following relation can be demonstrated, where δ is an offset term associated with the constant of proportionality between the left and right sides of Equation 28

$$
\ln\left[\frac{I_{em.}}{A\nu^4(J' + J'' + 1)}\right] = \frac{-B'hc}{k_B T}J'(J' + 1) + \delta
\tag{29}
$$

A plot of the left side of Equation 29 as a function of $J'(J' + 1)$ can be fit to a line whose slope (m) is related to temperature (T) as shown in Equation 30.

$$T = \frac{-B'hc}{k_B m} \qquad (30)$$

A sample result obtained using this technique is shown in Figure 50, where six rotational levels of the HCl P-branch, identified by $J' = 1, 2, 3, 4, 5, 6$ were used as data points to fit temperature to an individual plume pixel spectra from the hottest part of the plume, resulting in a plume temperature estimate of 634 ± 20 K, compared to the reported temperature of 406 K. This temperature difference results from applying a thin-plume technique to a plume that is relatively thick, with emissivities on the order of 0.4-0.8 over these spectral lines.

As with temperature, a simple thin-plume calculation can also be performed to estimate concentration from the observed HCl emission spectra. Using the P(4) or $J' = 3$ ro-vibrational line of the primary HCl isotope, which is centered at $\nu = 2798.94$ cm^{-1} and has a lower state transitional level energy of 208.59 cm^{-1} and Einstein-a coefficient of 23.18 $\frac{1}{s}$, the fraction of H^{35}Cl molecules that occupy this level can be computed as follows:

$$P_E = \frac{g(J = 3) \exp \frac{-E_i}{k_B T}}{Z(T)} \qquad (31)$$

where P_E is the probability of a photon being in energy state E_i, $g(J = 3)$ is the degeneracy term $(8(2J + 1) = 56)$, E_i is the transition energy $(hc\nu)$, and $Z(T)$ is the partition function, which at the operator-provided temperature of 406 K, corresponds to a value of 216.

The number of molecules in the excited state (N_1) is equal to this probability (P_E) multiplied by the total number of HCl molecules. For a given volume of plume, V, concentration of HCl can be calculated as:
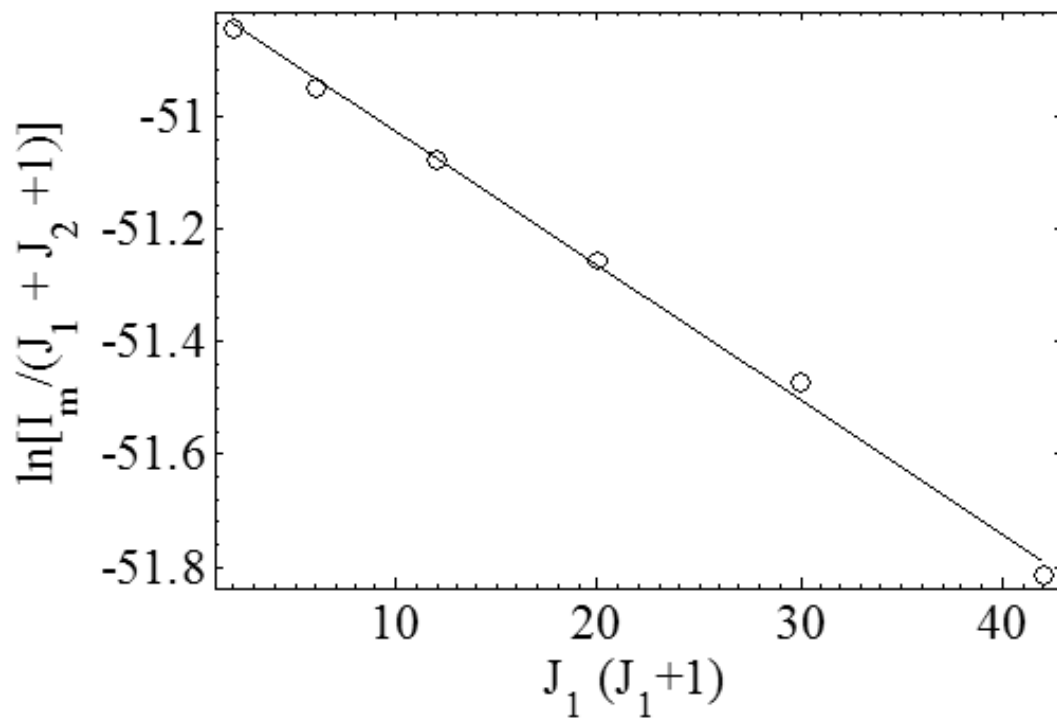
Figure 50. Determination of single-pixel temperature using the variation in line intensities as a function of rotational level due to thermal distribution of rotational levels. Six rotational levels of the P-branch of HCl were used as data points for this temperature fit, resulting in a plume pixel temperature of 634 ± 20 K

$$C = \frac{N}{V} = \frac{N_1}{P_E A l} \tag{32}$$

where C is the concentration of HCl in the plume, A is the projected plume area within instrument line-of-sight, and l is the corresponding pathlength through the plume.

Radiant intensity (I) from HCl, based on a spectral line, can be expressed as:

$$I = \frac{N_1 h \nu_{10} A_{10}}{4\pi} \tag{33}$$

where A_{10} is the Einstein-a coefficient, the product $h\nu_{10}$ converts from photons per second to Watts, and the factor 4π in the denominator results in an intensity value in terms of $\frac{W}{sr}$.

The observed radiance (L) is equal to radiant intensity (I) per unit area, and by integrating over the P(4) HCl line, can be expressed in terms of Equation 33 as:

$$L = \frac{I}{A} = \frac{N_1 h \nu_{10} A_{10}}{4\pi} \tag{34}$$

Replacing N_1 in Equation 34 in terms of concentration, C, as defined in Equation 32, gives the HCl concentration as:

$$C = \frac{4\pi L}{h\nu_{10} A_{10} l P_E} \tag{35}$$

From the observed P(4) HCl line, an HCl concentration of 56 ppmV was obtained

using this thin-plume calculation, compared to a fitted concentration of 111 ± 1 ppmV based on the single-temperature radiative transfer plume model. A factor of 2 difference between the fitted value obtained by the radiometric model and that obtained using this thin plume calculation is due to optical trapping by the plume with an emissivity on the order of 0.8 at the P(4) spectral line.

Appendix C. Plume Analysis Algorithms

Several algorithms were employed for the analysis of calibrated spectral radiance associated with combustion plumes. First, due to the magnitude of data and time necessary to perform radiometric calculations, the hyperspectral image was segmented into regions of similarity via k-means clustering.

Preliminary analysis of plume spectra revealed spectral features associated with plume constituents, and a subset of these features were extracted from each plume pixel and provided as input to the MATLAB k-means clustering algorithm. The clustering algorithm partitioned each set of data spatially, such that regions containing similar spectral content were grouped together. This aided analysis of plume pixels in three ways. First, clustering greatly reduced the dimensionality of the data. Second, background pixels were grouped together, and could be spatially averaged to produce an accurate estimate of instrument self-emission, since background radiance from the combustion data was negligible in comparison. Third, following background-subtraction to remove instrument self-emission, a spatial average of plume pixels within each cluster improved the signal-to-noise ratio. These spatially-averaged plume spectra were then passed to the radiometric fitting algorithm to be modelled spectrally for temperature and plume concentrations.

An estimate of the atmosphere (τ_{atm}) between source and sensor was computed based on molecular absorption cross-sections from the HITRAN database ($\sigma_i(\nu, T_p)$), and initial guesses of plume temperature (T_p) and constituent column densities ($q_i l$) were used to form an initial plume model (Equation 36 to accompany the spatially-averaged observed plume spectra in the fitting algorithm.

$$L_{mdl}(\nu, T_p) = \varepsilon(\nu, T_p) L_{BB}(\nu, T_p) \tau_{atm}(\nu, T_{atm}) \tag{36}$$

where $\varepsilon(\nu, T_p) = 1 - e^{-\sum_i q_i l \sigma_i(\nu, T_p)}$.

Due to uncertainty in absolute radiometric calibration, both the calibrated plume spectral radiance (L_{obs}) and model-derived plume spectral radiance functions (L_{mdl}) were normalized by integrated spectral radiance, and column densities and plume temperatures were adjusted using a least-squares fitting algorithm until the residual sum-square error was below a pre-defined threshold or until a maximum number of iterations was attempted.

Model-derived values of plume column densities were converted to concentrations by making some simplifying assumptions as to the spatial extent of the plume. Since the imagery of the plume only provides a two-dimensional projection of the plume, the third dimension (l) was obtained by estimating that plume expansion was cylindrical in nature. In other words, the plume would spread in the direction of instrument line-of-sight as it had perpendicular to line-of-sight, and each clustered region was treated as an individual plume volume.

Although these assumptions are not completely accurate physical representations of the plume, especially that of a single-temperature model, the residuals obtained by fitting the data to this model were very low, and the model-derived temperature and concentration values were very close to those provided by the stack operator at the industrial plant or measured with thermocouples in the jet engine exhaust plume.

Appendix D. Additional Jet Engine Data Sets

Chapter V reports on the collection and analysis of only one set of jet engine exhaust data, since no significant variation between datasets was evident from an initial analysis of the data. However, it should be noted that four sets of MWIR hyperspectral imagery of jet engine data were collected, each with the same instrument settings as defined in Chapter V. The engine was run with two different fuel types (diesel and kerosene), each at two fuel flow rates ($300 \; \frac{cm^{-3}}{min}$ and $150 \; \frac{cm^{-3}}{min}$).

The data was collected with the expectation that they would vary spectrally, and have distinct fit parameters associated with fitting to the single-temperature radiative transfer plume model. Relatively early on in this research, some effort was made in addressing this theory. However, at the time, only a gradient-based algorithm was used during spectral fitting of data to the model, and, as a result, residuals associated with fitting the data were relatively large. Consequently, significant differences between the four sets of data were not readily observed. Figure 51 shows the result of applying K-means clustering to each of the four sets of data. The plume shape, and clustered regions, are very similar in all four images. Image (a) and (b) show the plume clusters for diesel fuel exhaust with flow rates of 300 and $150 \; \frac{cm^{-3}}{min}$, while images (c) and (d) depict plume clusters from kerosene fuel plume data.

Figure 52 shows the results obtained from fitting each of the four temporally-averaged datacubes to a single-temperature plume model. Fit parameters were very similar, between the kerosene and diesel fuel jet engine data. No significant temperature differences were obtained, and column densities for the plume constituents did not vary significantly, either.

With the improved fitting algorithm, it may be worthwhile to investigate these datasets further. The improved method of spectral fitting incorporates both a gradient-based approach and a random search method for encountering the residual global
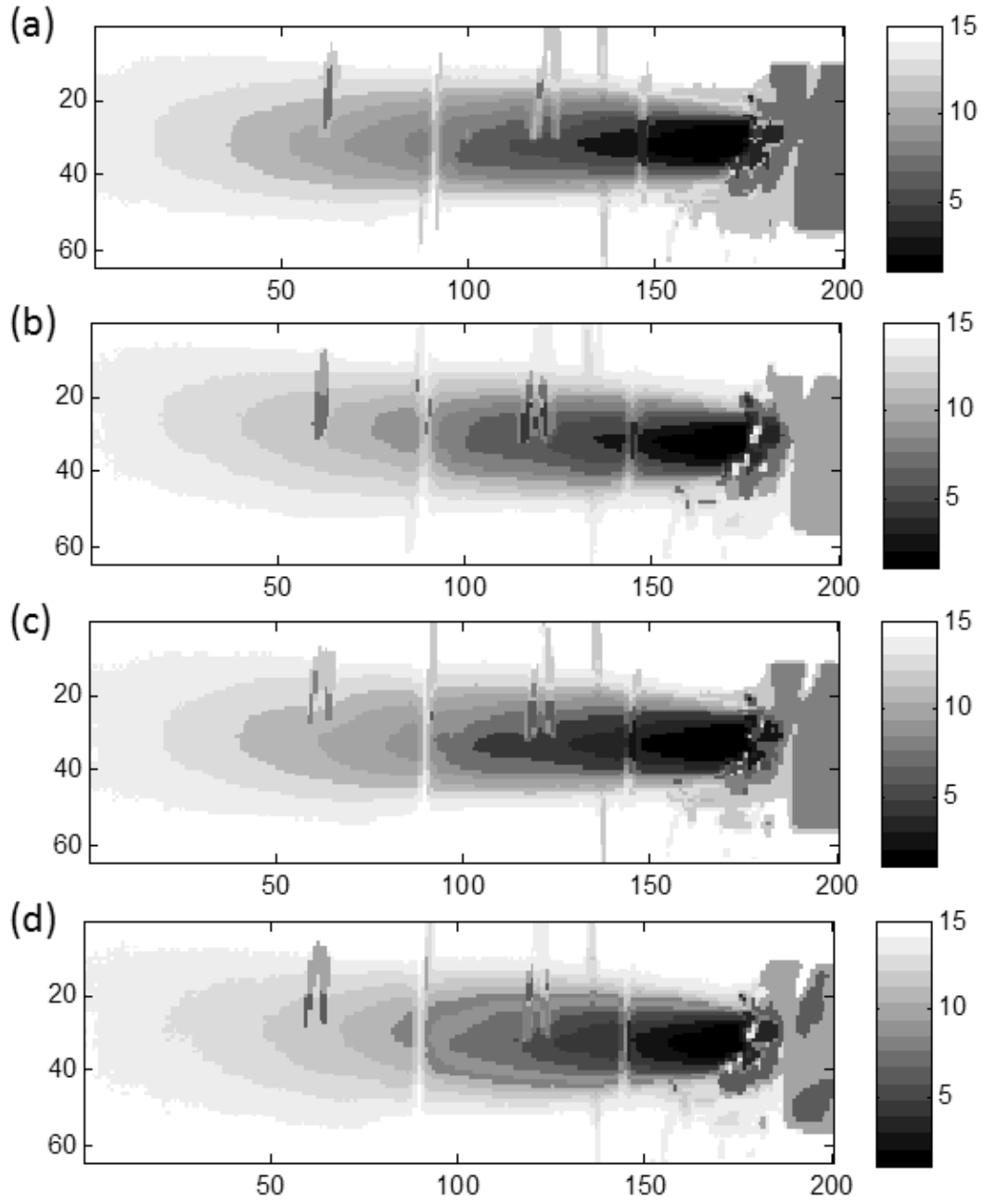
Figure 51. Clustering of jet engine exhaust data. (a) Diesel fuel with flow rate of 300 $\frac{cm^{-3}}{min}$. (b) Diesel fuel with flow rate of 150 $\frac{cm^{-3}}{min}$. (c) Kerosene fuel with flow rate of 300 $\frac{cm^{-3}}{min}$. (d) Kerosene fuel with flow rate of 150 $\frac{cm^{-3}}{min}$.
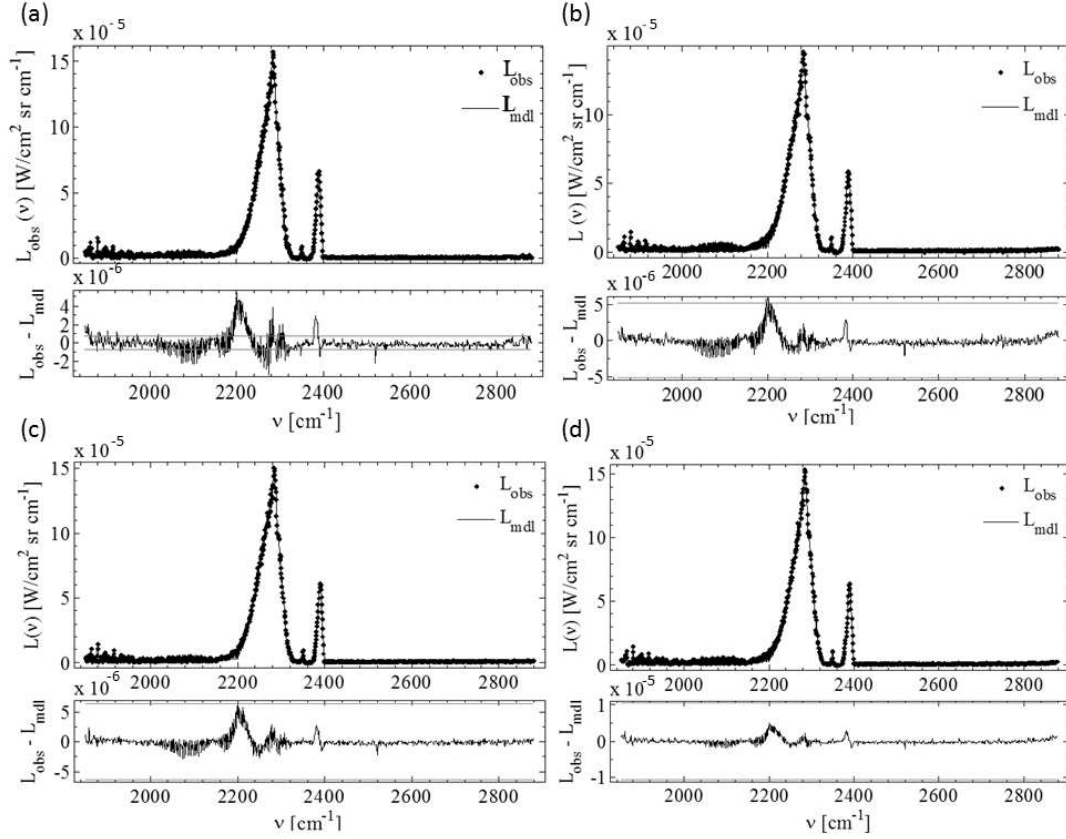
Figure 52. **Results from fitting jet engine exhaust data to single-temperature plume model for the hottest region of the plume. (a) Diesel fuel with flow rate of 300 $\frac{cm^{-3}}{min}$. (b) Diesel fuel with flow rate of 150 $\frac{cm^{-3}}{min}$. (c) Kerosene fuel with flow rate of 300 $\frac{cm^{-3}}{min}$. (d) Kerosene fuel with flow rate of 150 $\frac{cm^{-3}}{min}$.**

minimum. The initial method only used a gradient-based search, and would regularly encounter a local minimum, without stepping out far enough to encounter the true global minimum. This resulted in much larger residuals, and may have also led to similar fit statistics for the four jet engine datasets.

Bibliography

[1] U.S. Army Chemical and Biological Defense Command & National Research Council (U.S.), Technical assessment of the Man-in-Simulant Test (MIST) program. National Academy Press, Washington, D.C., 1997.

[2] Althouse, Mark L. and Chein-I Chang. "Chemical vapor detection with a multispectral thermal imager". *Optical Engineering*, 30:1725–1733, 1991.

[3] Anderson, Thomas N., Robert P. Lucht, Terrence R. Meyer, Sukesh Roy, and James R. Gord. "Diode-laser-based ultraviolet-absorption sensor for high-speed detection of the hydroxyl radical". *Opt.Lett.*, 30:1321–1323, 2005.

[4] Arrigone, Giovanni M. and Moira Hilton. "Optical spectroscopic measurement of unburnt hydrocarbons in emissions from aeroengine combustion systems". volume 4168, 221–231. SPIE, 2001.

[5] Arrigone, Giovanni M., Michael A. Welch, Moira Hilton, Michael N. Miller, and Christopher W. Wilson. "Detection of ethene and other hydrocarbons in gas turbine engine exhaust using non-intrusive FTIR spectroscopy". volume 4882, 384–393. SPIE, 2003.

[6] Arrigone, GiovanniM and Moira Hilton. "Theory and practice in using Fourier transform infrared spectroscopy to detect hydrocarbons in emissions from gas turbine engines". *Fuel*, 84:1052–1058, 2005.

[7] Bennett, Charles L., Michael R. Carter, David J. Fields, and F. D. Lee. "Infrared hyperspectral imaging results from vapor plume experiments". volume 2480, 435–444. SPIE, 1995.

[8] Bluth, G. J. S., J. M. Shannon, I. M. Watson, A. J. Prata, and V. J. Real-muto. "Development of an ultra-violet digital camera for volcanic SO_2 imaging". *Journal of Volcanology and Geothermal Research*, 161:47–56, 2007.

[9] Bowen, Spencer J. *Hyperspectral imaging of a turbine engine exhaust plume to determine radiance, temperature, and concentration spatial distributions.* 2009. AFIT/GAP/ENP/09-M02; Thesis (M.S.)–Air Force Institute of Technology.

[10] Bracewell, Ronald N. *The Fourier transform and its applications.* McGraw Hill, Boston, 2000.

[11] Carlson, R. C., A. F. Hayden, and W. B. Telfair. "Remote observations of effluents from small building smokestacks using FTIR spectroscopy". *Applied Optics*, 27:4952–4959, 1988.

[12] Carter, Michael R., Charles L. Bennett, David J. Fields, and John A. M. Hernandez. "Gaseous effluent monitoring and identification using an imaging Fourier transform spectrometer". volume 2092, 16–26. SPIE, 1994.

[13] Carter, Michael R., Charles L. Bennett, David J. Fields, and F. D. Lee. "Livermore Imaging Fourier Transform Infrared Spectrometer (LIFTIRS)". volume 2480, 380–386. SPIE, 1995.

[14] Chamberland, Martin, Vincent Farley, Jean Giroux, Andre Villemaire, Jean-Francois Legault, and Karl R. Schwantes. "Development and testing of a hyperspectral imaging instrument for standoff chemical detection". volume 5584, 135–143. SPIE, 2004.

[15] Chamberland, Martin, Vincent Farley, Pierre Tremblay, and JeanFrancois Legault. "Performance model of imaging FTS as a standoff chemical agent detection tool". volume 5268, 240–251. SPIE, 2004.

[16] Chan, Shih H., Chuen C. Lin, and M. J. D. Low. "Analysis of principles of remote sensing and characterization of stack gases by infrared spectroscopy". *Environmental Science & Technology*, 7:424–427, 1973.

[17] Dereniak, Eustace L. and G. D. Boreman. *Infrared detectors and systems*. Wiley, New York, 1996.

[18] Dillon, William R. and Matthew Goldstein. *Multivariate analysis : methods and applications*. Wiley, New York, 1984.

[19] Edner, Hans, Kent Fredriksson, Anders Sunesson, Sune Svanberg, Leif Uneus, and Wilhelm Wendt. "Mobile remote sensing system for atmospheric monitoring". *Appl.Opt.*, 26:4330, 1987.

[20] Edner, Hans, Pár Ragnarson, Stefan Spánnare, and Sune Svanberg. "Differential optical absorption spectroscopy (DOAS) system for urban atmospheric pollution monitoring". *Appl.Opt.*, 32:327–333, 1993.

[21] Farley, Vincent, Martin Chamberland, Alexandre Vallières, André Villemaire, and Jean-François Legault. "Radiometric calibration stability of the FIRST: a longwave infrared hyperspectral imaging sensor". volume 6206, 62062A. SPIE, 2006.

[22] Farley, Vincent, Alexandre Vallières, Martin Chamberland, André Villemaire, and Jean-François Legault. "Performance of the FIRST: a long-wave infrared hyperspectral imaging sensor". volume 6398, 63980T. SPIE, 2006.

[23] Flores-Jardines, Edgar, Klaus Schäfer, Roland Harig, Peter Rusch, and Michel Grutter. "Investigation of temperature and gas concentration distributions in hot exhausts (airplanes and burners) by scanning imaging FTIR spectrometry". volume 5979, 59791A. SPIE, 2005.

[24] Gittins, Christopher M., William J. Marinelli, and James O. Jensen. "Remote Characterization of Chemical Vapor Plumes by LWIR Imaging Fabry-Perot Spectrometry". *Fifth Joint Conference on Standoff Detection for Chemical and Biological Defense: "CB Standoff: An Integrated Future"*. Physical Sciences Inc., September 2001.

[25] Griffiths, Peter R. and James A. De Haseth. *Fourier transform infrared spectrometry*. Wiley, New York, 1986.

[26] Gross, Kevin C. "Phenomenological model for infrared emissions from high-explosive detonation fireballs", 2007.

[27] Gupta, Neelam and Dale Smith. "A simultaneous dual-band infrared hyperspectral imager for standoff detection". volume 5995, 59950. SPIE, 2005.

[28] Harig, R., M. Grutter, G. Matz, P. Rusch, and J. Gerhard. "Remote Measurement of Emissions by Scanning Imaging Infrared Spectrometry". *CEM2007, 8th International Conference on Emissions Monitoring*, 34–39, 2007.

[29] Harig, Roland, Peter Rusch, Klaus Schäfer, and Edgar FloresJardines. "Method for on-site determination of the instrument line shape of mobile remote sensing Fourier transform spectrometers". volume 5979, 59791H. SPIE, 2005.

[30] Haus, R., K. Schafer, W. Bautzer, J. Heland, H. Mosebach, H. Bittner, and T. Eisemann. "Mobile Fourier-transform infrared spectroscopy monitoring of air pollution". *Appl. Opt.*, 33:5682, 1994.

[31] Heasler, P. "Nonlinear Bayesian Algorithms for Gas Plume Detection and Estimation from Hyper-spectral Thermal Image Data". *Sensors*, 7:905–920, 2007.

[32] Hecht, Eugene. *Optics*. Addison-Wesley, Reading, Mass., 2002.

[33] Heland, Jörg and Klaus Schäfer. "Analysis of aircraft exhausts with Fourier-transform infrared emission spectroscopy". *Appl. Opt.*, 36:4922–4931, 1997.

[34] Hendricks, A. G., U. Vandsburger, W. R. Saunders, and W. T. Baumann. "The use of tunable diode laser absorption spectroscopy for the measurement of flame dynamics". *Measurement Science and Technology*, 17:139–144, 2006.

[35] Herget, William F. "Remote and cross-stack measurement of stack gas concentrations using a mobile FT-IR system". *Appl. Opt.*, 21:635, 1982.

[36] Herget, William F. and James D. Brasher. "Remote measurement of gaseous pollutant concentrations using a mobile Fourier transform interferometer system". *Appl. Opt.*, 18:3404, 1979.

[37] Herzberg, Gerhard. *Infrared and Raman spectra of polyatomic molecules*. Van Nostrand, New York, 1945.

[38] Herzberg, Gerhard. *Spectra of diatomic molecules*. Van Nostrand, New York, 1950.

[39] Hilton, Moira, Giovanni M. Arrigone, and Michael N. Miller. "Non-intrusive spectroscopic investigations of soot and unburnt hydrocarbons in combustion gases". volume 3821, 198–208. SPIE, 1999.

[40] Hilton, Moira, Alan H. Lettington, and Ian M. Mills. "Remote gas detection and quantitative analysis from infrared emission spectra obtained by Fourier transform infrared spectroscopy". volume 2222, 130–137. SPIE, 1994.

[41] Hinnrichs, M., J. O. Jensen, and G. McAnally. "Handheld hyperspectral imager for standoff detection of chemical and biological aerosols". *Proceedings of SPIE*, 5268:67–78, 2003.

[42] Hinnrichs, Michele. "Remote sensing for gas plume monitoring using state-of-the-art infrared hyperspectral imaging". volume 3534, 370–381. SPIE, 1999.

[43] Hirsch, Eitan and Eyal Agassi. "Detection of gaseous plumes in IR hyperspectral images using hierarchical clustering". *Appl. Opt.*, 46:6368–6374, 2007.

[44] Jeffries, J. B., C. Schulz, D. W. Mattison, M. A. Oehlschlaeger, W. G. Bessler, T. Lee, D. F. Davidson, and R. K. Hanson. "UV absorption of CO2 for temperature diagnostics of hydrocarbon combustion applications". *Proceedings of the Combustion Institute*, 30:1591–1599, 1 2005.

[45] Jellison, Gerard P. and David P. Miller. "Determination of gas plume temperature from molecular emission spectra". *Optical Engineering*, 45:016201, 2006.

[46] Kranendonk, Laura A., Andrew W. Caswell, Christopher L. Hagen, Craig T. Neuroth, Dale T. Shouse, James R. Gord, and Scott T. Sanders. "Temperature Measurements in a Gas-Turbine-Combustor Sector Rig Using Swept-Wavelength Absorption Spectroscopy". *Journal of Propulsion and Power*, 25:859–863, 2009.

[47] Kranendonk, Laura A., Robert Huber, James G. Fujimoto, and Scott T. Sanders. "Wavelength-agile H_2O absorption spectrometer for thermometry of general combustion gases". *Proceedings of the Combustion Institute*, 31:783–790, 2007.

[48] Kwan, C., B. Ayhan, G. Chen, Jing Wang, Baohong Ji, and Chein-I Chang. "A novel approach for spectral unmixing, classification, and concentration estimation of chemical and biological agents". *IEEE Transactions on Geoscience and Remote Sensing*, 44:409–419, 2006.

[49] Manolakis, Dimitris and Francis M. D'Amico. "Design and evaluation of hyperspectral algorithms for chemical warfare agent detection". volume 5995, 599503. SPIE, 2005.

[50] Manolakis, Dimitris G. and Francis M. D'Amico. "A taxonomy of algorithms for chemical vapor detection with hyperspectral imaging spectroscopy". volume 5795, 125–133. SPIE, 2005.

[51] Marinelli, William J., Christopher M. Gittins, Bogdan C. Cosofret, Teoman E. Ustun, and James O. Jensen. "AIRIS Wide Area Detection System Field Tests". *6th Joint Conference on Standoff Detection for Chemical and Biological Defense.* 2004.

[52] Marinelli, William J., Christopher M. Gittins, Bogdan C. Cosofret, Teoman E. Ustun, and James O. Jensen. "Development of the AIRIS-WAD Multispectral Sensor for Airborne Standoff Chemical Agent and Toxic Industrial Chemical Detection". *2005 Parallel Meetings of the MSS Specialty Groups on Passive Sensors; Camouflage, Concealment, and Decpetion; Detectors; and Materials.* Physical Sciences Inc., 2005.

[53] Marinelli, William J., Christopher M. Gittins, Alan H. Gelb, and B. D. Green. "Tunable Fabry–Perot Etalon-Based Long-Wavelength Infrared Imaging Spectroradiometer". *Appl.Opt.*, 38:2594–2604, 1999.

[54] Mehta, Naresh C., Ernst T. Scharlemann, and Charles G. Stevens. "Quantitative estimation of trace chemicals in industrial effluents with the Sticklet transform method". volume 4378, 10–20. SPIE, 2001.

[55] Messinger, D. W., C. Salvaggio, and N. M. Sinisgalli. "Detection of Gaseous Effluents from Airborne LWIR Hyperspectral Imagery using Physics-based Signatures". *2006 International Symposium of Spectral Sensing Research (ISSSR), Frontier Sensing and Monitoring, Novel Hyperspectral Sensors and Algorithms.* 2006.

[56] Meyer, Terrence R., Sukesh Roy, Thomas N. Anderson, Robert P. Lucht, Rodolfo Barron-Jimenez, and James R. Gord. "10 kHz detection of CO_2 at 4.5 μm by using tunable diode-laser-based difference-frequency generation". *Optics Letters*, 30:3087–3089, 2005.

[57] Milláan, Milláan M. and Raymond M. Hoff. "Remote sensing of air pollutants by correlation spectroscopyinstrumental response characteristics". *Atmospheric Environment*, 12:853–864, 1978.

[58] Moore, Elizabeth A., Kevin C. Gross, Spencer J. Bowen, Glen P. Perram, Martin Chamberland, Vincent Farley, Jean-Philippe Gagnon, Philippe Lagueux, and Andre Villemaire. "Characterizing and overcoming spectral artifacts in imaging Fourier-transform spectroscopy of turbulent exhaust plumes". volume 7304, 730416. SPIE, 2009.

[59] Nelsson, C., F. Lundberg, P. Nilsson, and M. Berglund. "ScanSpec: an imaging FTIR spectrometer". Wendell R. Watkins, Dieter Clement, and William R. Reynolds (editors), *Society of Photo-Optical Instrumentation Engineers (SPIE) Conference Series; Presented at the Society of Photo-Optical Instrumentation Engineers (SPIE) Conference*, volume 4029, 324–336. 2000.

[60] O'Donnell, E. M., D. W. Messinger, C. Salvaggio, and J. R. Schott. "The invariant algorithm for identification and detection of multiple gas plumes and weak releases". *Proceedings of the SPIE, Sensor Data Exploitation and Target Recognition, Algorithms and Technologies for Multispectral, Hyperspectral, and Ultraspectral Imagery X*, volume 5806, 206–217. SPIE, 2005.

[61] Pelleg, Dan and Andrew Moore. "X-means: Extended K-means with Efficient Estimation of the Number of Clusters". 2000.

[62] Platt, U. *Air monitoring by spectroscopic techniques*, 27–84. Wiley, New York, 1994.

[63] Polak, Mark L., Jeffrey L. Hall, and Kenneth C. Herr. "Passive Fourier-transform infrared spectroscopy of chemical plumes: an algorithm for quantitative interpretation and real-time background removal". *Appl. Opt.*, 34(24):5406, 1995.

[64] Prengle, H. W., Charles A. Morgan, Chen-Shen Fang, Ling-Kun Huang, Paolo Campani, and William W. Wu. "Infrared remote sensing and determination of pollutants in gas plumes". *Environmental Science & Technology*, 7:417–423, 1973.

[65] Rogalski, A. and K. Chrzanowski. "Infrared devices and techniques". *Opto-electronics Review*, 10:111–136, 2002.

[66] Rusch, Peter, Roland Harig, Gerhard Matz, Klaus Schäfer, Carsten Jahn, and Selina Utzig. "SIGIS HR: a system for measurement of aircraft exhaust gas under normal operating conditions of an airport". volume 5979, 597922. SPIE, 2005.

[67] Schäfer, Klaus, Joerg Heland, Roger Burrows, John V. Black, Marc Bernard, Gary Bishop, Volker Tank, Erwin Lindermeir, Dave H. Lister, Robert S. Falk, Peter Wiesen, and Moira Hilton. "AEROJET: nonintrusive measurements of aircraft engine exhaust emissions". volume 3108, 38–41. SPIE, 1997.

[68] Schäfer, Klaus, Joerg Heland, Erwin Lindermeir, Moira Hilton, Gary Bishop, Johanna Vally, Peter Wiesen, Dave H. Lister, and Marc Bernard. "Determination of exhaust composition in turbine test beds by FTIR emission spectrometry". volume 3821, 191–197. SPIE, 1999.

[69] Schäfer, Klaus, Joerg Heland, Dave H. Lister, Erwin Lindermeir, Moira Hilton, Gary Bishop, Peter Wiesen, and Marc Bernard. "Evaluation of FTIR emission

spectrometry for the determination of turbine exhaust composition in test beds".
volume 3821, 416–421. SPIE, 1999.

[70] Schäfer, Klaus, Jörg Heland, Dave H. Lister, Chris W. Wilson, Roger J. Howes, Robert S. Falk, Erwin Lindermeir, Manfred Birk, Georg Wagner, Peter Haschberger, Marc Bernard, Olivier Legras, Peter Wiesen, Ralf Kurtenbach, Klaus J. Brockmann, Volker Kriesche, Moira Hilton, Gary Bishop, Roy Clarke, John Workman, Michael Caola, Rachel Geatches, Roger Burrows, John D. Black, Philippe Hervé, and Johanna Vally. "Nonintrusive Optical Measurements of Aircraft Engine Exhaust Emissions and Comparison with Standard Intrusive Techniques". *Appl. Opt.*, 39:441–455, 2000.

[71] Schürmann, Gregor, Klaus Schäfer, Carsten Jahn, Herbert Hoffmann, and Selina Utzig. "Detection of emission indices of aircraft exhaust compounds by open-path optical methods at airports". volume 5979, 59791B. SPIE, 2005.

[72] Selby, J. E. A. and R. A. Reed. "Atmospheric Background and Smoke Stack Measurements and Modeling in the 3.8-5.5 μm Region". *Optical Properties of the Atmosphere, SPIE Proceedings*, 1978.

[73] Shepanski, J. and S. Sandor-Leahy. "LWIR hyperspectral imagery and its exploitation for gas plume characterization". *Geoscience and Remote Sensing Symposium, 2005*, 7:4958– 4961, 2005.

[74] Somesfalean, Gabriel, Janis Alnis, Ulf Gustafsson, Hans Edner, and Sune Svanberg. "Long-path monitoring of NO2 with a 635 nm diode laser using frequency-modulation spectroscopy". *Appl.Opt.*, 44:5148–5151, 2005.

[75] Spisz, Thomas S., Patricia K. Murphy, Christopher C. Carter, Alison K. Carr,

Alexandre Vallières, and Martin Chamberland. "Field test results of standoff chemical detection using the FIRST". volume 6554, 655408. SPIE, 2007.

[76] Suhre, Dennis R. and Eliel Villa. "Imaging spectroradiometer for the 8-12 μm region with a 3 cm^{-1} passband acousto-optic tunable filter". *Appl.Opt.*, 37(12):2340–2345, 1998.

[77] Thomas, Mark J., Paul E. Lewis, Robert T. Kroutil, Roger J. Combs, Gary W. Small, Randall W. Zywicki, Dale L. Stageberg, Charles T. C. Jr., and Timothy L. Marshall. "Infrared detection and analysis of vapor plumes using an airborne sensor". volume 4725, 47–64. SPIE, 2002.

[78] Tremblay, Pierre, Kevin C. Gross, Vincent Farley, Martin Chamberland, André Villemaire, and Glen P. Perram. "Understanding and Overcoming Scene-Change Artifacts in Imaging Fourier-Transform Spectroscopy of Turbulent Jet Engine Exhaust". volume 7457. SPIE, 2009.

[79] Vallières, Alexandre, André Villemaire, Martin Chamberland, Louis Belhumeur, Vincent Farley, Jean Giroux, and Jean-François Legault. "Algorithms for chemical detection, identification and quantification for thermal hyperspectral imagers". volume 5995, 59950G. SPIE, 2005.

[80] Walter, Jr., Howard and Dennis Flanigan. "Detection of atmospheric pollutants: a correlation technique". *Appl.Opt.*, 14:1423–1428, 1975.

[81] Weibring, P., M. Andersson, H. Edner, and S. Svanberg. "Remote monitoring of industrial emissions by combination of lidar and plume velocity measurements". *Applied Physics B: Lasers and Optics*, 66:383–388, 1998.

[82] Weibring, Petter, Hans Edner, and Sune Svanberg. "Versatile Mobile Lidar System for Environmental Monitoring". *Appl.Opt.*, 42:3583–3594, 2003.

[83] Wormhoudt, Joda. *Infrared methods for gaseous measurements : theory and practice.* M. Dekker, New York, 1985.

REPORT DOCUMENTATION PAGE

The public reporting burden for this collection of information is estimated to average 1 hour per response, including the time for reviewing instructions, searching existing data sources, gathering and maintaining the data needed, and completing and reviewing the collection of information. Send comments regarding this burden estimate or any other aspect of this collection of information, including suggestions for reducing the burden, to Department of Defense, Washington Headquarters Services, Directorate for Information Operations and Reports (0704-0188), 1215 Jefferson Davis Highway, Suite 1204, Arlington, VA 22202-4302. Respondents should be aware that notwithstanding any other provision of law, no person shall be subject to any penalty for failing to comply with a collection of information if it does not display a currently valid OMB control number.
PLEASE DO NOT RETURN YOUR FORM TO THE ABOVE ADDRESS.

1. REPORT DATE *(DD-MM-YYYY)*	2. REPORT TYPE	3. DATES COVERED *(From - To)*

4. TITLE AND SUBTITLE

5a. CONTRACT NUMBER

5b. GRANT NUMBER

5c. PROGRAM ELEMENT NUMBER

6. AUTHOR(S)

5d. PROJECT NUMBER

5e. TASK NUMBER

5f. WORK UNIT NUMBER

7. PERFORMING ORGANIZATION NAME(S) AND ADDRESS(ES)

8. PERFORMING ORGANIZATION REPORT NUMBER

9. SPONSORING/MONITORING AGENCY NAME(S) AND ADDRESS(ES)

10. SPONSOR/MONITOR'S ACRONYM(S)

11. SPONSOR/MONITOR'S REPORT NUMBER(S)

12. DISTRIBUTION/AVAILABILITY STATEMENT

13. SUPPLEMENTARY NOTES

14. ABSTRACT

15. SUBJECT TERMS

16. SECURITY CLASSIFICATION OF:			17. LIMITATION OF ABSTRACT	18. NUMBER OF PAGES	19a. NAME OF RESPONSIBLE PERSON
a. REPORT	b. ABSTRACT	c. THIS PAGE			
					19b. TELEPHONE NUMBER *(Include area code)*